Segmented Thermoelectric Oxide-based Module

Le, Thanh Hung

Publication date:
2014

Document Version
Publisher's PDF, also known as Version of record

SEGMENTED THERMOELECTRIC OXIDE-BASED MODULE

Ph.D. Thesis

By

Lê Thanh Hùng

Principle supervisor: Prof. Nini Pryds

Co-supervisors: Dr. Ngo Van Nong

Prof. Søren Linderoth

Department of Energy Conversion and Storage

Technical University of Denmark

Roskilde, Denmark

September 2014

Abstract

Since 1990s, oxide thermoelectrics have been considered as promising thermoelectric (TE) materials due to their non-toxicity, low-cost, and chemical stability at high temperatures. Studied results show great potential for applications in thermoelectric power generator (TEG) at high temperature and thus have drawn attentions over the years. However, oxides TEGs are still not used broadly due to their low performance. This thesis targets the research and development of exploring the use of these materials in high temperatures range using high conversion efficiency TEG based modules. This study demonstrates an effective way to improve the efficiency of oxide TEG by segmentation of oxide materials with other high-performance non-oxide materials, thereby, extending the temperature range.

This thesis was started by developing of *n*-type oxide material e.g. $CaMnO_3$ as possible alternative *n*-type candidate for a more stable high temperature material. In this study, thermoelectric properties from 300 to 1200 K of $Ca_{0.9}Y_{0.1}Mn_{1-x}Fe_xO_3$ for $0 \leq x \leq 0.25$ were systematically investigated in term of Y and Fe co-doping at the Ca- and Mn-sites, respectively. It was found that with increasing the content of Fe doping, the Seebeck coefficient of $Ca_{0.9}Y_{0.1}Mn_{1-x}Fe_xO_3$ tended to increase, while the tendency towards the electrical conductivity was more complicated. Thermal conductivity of the Fe-doped samples showed a lower value than that of the non-doped sample. The maximum dimensionless figure-of-merit, zT was found to be improved about 20% for the sample with $x = 0.05$ as compared to that of the $x = 0$ sample at 1150 K.

High-performance segmented legs/unicouples based on oxide materials are first designed by numerical modelling. The criteria of material selection for segmentation are based on their "efficiency ratio" described the total conversion efficiency per the materials cost and their compatibility factors. The numerical modeling results (chapter 3) showed that the maximum theoretical conversion efficiency of segmented legs/unicouples could be over 10%, which is more than twice as compared with the one comprised from non-segmented oxide elements. The calculation also takes into account the interfacial contact resistances to evaluate the influence on the total conversion efficiency. The obtained modeling results provide useful tools for designing future low-cost, high-performance segmented TEGs.

A high-performance segmented oxide-based module comprising of 4-unicouples using segmentation of the half-Heusler $Ti_{0.3}Zr_{0.35}Hf_{0.35}CoSb_{0.8}Sn_{0.2}$ and the misfit-layered cobaltite $Ca_3Co_4O_{9+\delta}$ as the *p*-leg and 2% Al-doped ZnO as the *n*-leg was successfully fabricated and characterized. The results (presented in Chapter 5) show that at a temperature difference of 700 K, the maximum output power density attains a value of ~6.5 kW/m^2, which is three times higher than that of a non-segmented oxide module under the same condition. Initial long-term stability test of the module at hot and cold side temperature of 1073/444 K showed a promising result, although a slight degradation tendency could be observed after 48 hours of operating in air. Nevertheless, the total

conversion efficiency of this segmented module is still low less than 2%, and needs to be further improved. A degradation mechanism was observed, which attributed to the increase in the interfacial contact resistance between the *n*-type material (doped ZnO) and the metal electrode.

The next study (Chapter 6) focuses on enhancing the efficiency of a single oxide-based segmented leg by further reducing the contact resistance and employing materials with better TE properties, i.e. a *p*-type leg that consists of misfit-layered cobaltite $Ca_{2.8}Lu_{0.15}Ag_{0.05}Co_4O_{9+\delta}$ nano-composite and the half-Heusler $Ti_{0.3}Zr_{0.35}Hf_{0.35}CoSb_{0.8}Sn_{0.2}$ alloy. For the first time, a maximum conversion efficiency as high as ~5% at a $\Delta T \approx 756$ K was measured. This high efficiency segmented leg is also tested for over two weeks at the hot and cold side temperatures of 1153/397 K, showing good durability as a result of stable, low electrical resistance contacts.

Abstract (Danish)

Siden 1990'erne, har oxid termoelektriske materialer været betragtet som lovende termoelektriske (TE) materialer på grund af fraværet af giftige stoffer, lave omkostninger og kemisk stabilitet ved høje temperaturer. Resultaterne viser store muligheder for anvendelser i termoelektriske generatorer (TEG) ved høj temperatur og har derfor tiltrukket sig opmærksomhed gennem årene. Men oxid TEG'er bruges stadig ikke bredt på grund af deres lave ydelse. Denne afhandling er fokuseret på forskning og udvikling for at udforske brugen af disse materialer ved høje temperaturer ved hjælp af TEG baseret moduler med høj konverteringseffektivitet. Denne undersøgelse viser en effektiv måde at forbedre effektiviteten af oxid TEG ved segmentering af nitrogenoxid materialer med andre højtydende ikke-oxid materialer for derved at udvide temperaturintervallet.

Denne afhandling starter med udviklingen af *n*-type oxid materialer fx $CaMnO_3$ som mulig alternativ *n*-type kandidat til et mere stabilt høj-temperatur materiale. I denne undersøgelse, blev termoelektriske egenskaber fra 300 K til 1200 K af $Ca_{0.9}Y_{0.1}Mn_{1-x}Fe_xO_3$ for $0 \leq x \leq 0{,}25$ systematisk undersøgt på med henblik på Y og Fe dotering på Ca- og Mn-pladserne, henholdsvis. Det blev konstateret, at med et stigende indhold af Fe dotering har Seebeck koefficient på $Ca_{0.9}Y_{0.1}Mn_{1-x}Fe_xO_3$ tendens til at stige, mens den elektriske ledningsevne var mere kompliceret. Varmeledningsevnen af de Fe-doterede prøver viste en lavere værdi end for den ikke-doterede prøve. Den maksimale dimensionsløse "figure of merit", zT, konstateredes at blive forbedret omkring 20 % i prøven med $x = 0{,}05$ i forhold til x = 0 prøven ved 1150 K.

Højtydende segmenterede ben/unicouples baseret på oxid materialer er først designet ved numerisk modellering. Kriterierne i materialevalget er baseret på deres "effektivitets forhold" som er den samlede konverteringseffektivitet pr. materiale omkostning, og deres kompatibilitets faktorer. Numerisk modellerings resultater (kapitel 3), viste, at den maksimale teoretiske konverteringseffektivitet på segmenterede ben/unicouples kunne være over 10 %, hvilket er mere end det dobbelte af den fra ikke-segmenterede oxid elementer. Beregningen tager også hensyn til grænseflade kontaktmodstand for at vurdere indflydelsen på den samlede konverteringseffektivitet. De opnåede modellerings resultater giver et nyttigt værktøj til at designe fremtidens billige, højtydende segmenteret TEGs.

Et højtydende segmenteret oxid-baseret modul bestående af 4-unicouples ved hjælp af segmentering af halv-Heusler materialet $Ti_{0.3}Zr_{0.35}Hf_{0.35}CoSb_{0.8}Sn_{0.2}$ og den utilpassede-lags koboltit $Ca_3Co_4O_9$ som p-ben og 2% Al-doteret ZnO som n-ben er blevet fremstillet og karakteriseret. Resultaterne (præsenteret i kapitel 5) viser, at ved en temperaturforskel på 700 K opnår den en maksimal effekttæthed på 6.5 kW/m^2, hvilket er tre gange højere end for et ikke-segmenteret oxid modul under samme betingelser. Indledende langtidsstabilitet af modulet med varm og kold side temperaturer på henholdsvis 1073 K og 444 K, viste et lovende resultat, selv om en lille tendens til nedbrydning kunne konstateres efter 48 timers operation i luft. Ikke desto mindre er den samlede konverteringseffektivitet på dette segmenterede modul stadig lav, mindre end 2%, og skal forbedres yderligere. Den observerede nedbrydnings mekanisme tilskrives stigningen i grænseflade kontaktmodstand mellem *n*-type materialet og metal elektroden.

Den næste undersøgelse (kapitel 6) fokuserer på at styrke effektiviteten af et enkelt oxid-baseret segmenteret ben ved yderligere at reducere kontakt modstanden og benytte materialer med bedre TE egenskaber, dvs *p*-type ben bestående af utilpassede-lags koboltit $Ca_{2.8}Lu_{0.15}Ag_{0.05}Co_4O_{9\ +\delta}$ nano-komposit og en halv-Heusler $Ti_{0.3}Zr_{0.35}Hf_{0.35}CoSb_{0.8}Sn_{0.2}$ legering. For første gang blev en maksimal konverteringseffektivitet på ~5 % ved $\Delta T \approx 756$ K målt. Dette højeffektive segmenterede ben er også testet i over to uger ved varm- og koldside temperaturer på henholdsvis 1153 K og 397 K, hvor det udviser god holdbarhed som følge af stabile, lav-modstands elektriske kontakter.

Table of Contents

Acknowledgements

None of this work would have been possible without the guidance of my supervisors Dr. Ngo Van Nong, Prof. Nini Pryds, and Prof. Søren Linderoth. I have learnt, through them, the spirit of research – from basic lab skills and data analysis, to how to construct and write a scientific paper. My supervisors always motivate and guide me on how to approach and obtain the best results. More importantly, they have taught me how a scientific study should be done and how to deal with a problem, ranging from the general to the specific. I would like to take this opportunity to express my deep thanks to them.

I would like to express my sincere thanks to people in thermoelectric groups Li Han, Tim Holtage, NingYu Wu, Pham Hoang Ngan, Dennis Valbjørn Christensen, Ali Sarhadi, Rasmus Bjørk, Dan Eriksen, and Kaspar Kirstein Nielsen, who have helped, supported and brought me memorable during my Ph.D. study. I would also like thanks to Christian Bahl for helping in the translation of the thesis abstract, Eugen Stamate and Feisal Kroushawi for their assisting in sputtering system. Thanks to our laboratory technicians and engineers Steen Bang, Ebtisam Abdellahi, Karl Thydén, Pernille Hedemark Nielsen, Annelise Mikkelsen, Agnes Kjøller, Henrik Paulsen, Xiufu Sun, Carsten Gynther Sørensen, and John Johnson for the practical laboratory works and safety issues. I would like to give special thanks to Jørgen Geyti and Søren Kock for helping in building up the Rig-test thermoelectrics. Thanks to our secretary Anita Voss, Lene Thorsted, and Heidi Pedersen for helping me with the administrative work.

I would also like to give many thanks to our international collaborators Jeff Snyder, Benjamin Balke, Michitaka Ohtaki, Bo Brummerstedt Iversen, Man Hoang Viet, Dang Le Minh, and Kasper Andersen Borup, who have helped me immensely with modeling thermoelectrics, half-Heusler materials and Hall measurement.

I would like to express my sincere thanks to the assessment committee members Dr. Luise Theil Kuhn, Prof. Lasse Aistrup Rosendahl, and Dr. Yaniv Gelbstein for evaluating and assessing my thesis.

I would like to acknowledge our department, DTU Energy Conversion, for preciously supporting my study. Thanks to the Programme Commission on Energy and Environment (EnMi) which is part of the Danish Council for Strategic Research (Contract No. 10-093971), for financially supporting my research work which is part of the OTE-POWER project.

I would also like to express my deep gratitude to Nong's family for unlimitedly helping, sharing and caring for us since we moved to Denmark.

Lastly, my deepest gratitude goes to my family, my parents, my wife and my son for their unending support and encouragement. They are always with me – through anything and everything.

List of Publications

(During PhD study only)

Peer-reviewed Papers:

[1] Le Thanh Hung, Ngo Van Nong, Li Han, Dang Le Minh, Kasper A Borup, Bo B. Iversen, Nini Pryds, Søren Linderoth, "*High-temperature Thermoelectric Properties of* $Ca_{0.9}Y_{0.1}Mn_{1-x}Fe_xO_3$ *(*$0 \leq x \leq 0.25$*)*," J. Mater. Sci. **48**, 2817 (2013).

[2] Le Thanh Hung, Ngo Van Nong, Søren Linderoth, and Nini Pryds. "*Segmentation of low-cost, high efficiency oxide-based thermoelectric materials*", Phys. Status Solidi A, 1–8 (2015) / DOI 10.1002/pssa.201431626..

[3] Le Thanh Hung, Ngo Van Nong, G. Jeffrey Snyder, Li Han, Eugen Stamate, Man Hoang Viet, Benjamin Balke, Søren Linderoth, and Nini Pryds, "*High Performance p-type Segmentation of Oxide and Half-Heusler Alloy*", Energy Conversion and Management, under review, (2014).

[4] Le Thanh Hung, Ngo Van Nong, G. Jeffrey Snyder, Benjamin Balke, Li Han, Rasmus Bjørk, Pham Hoang Ngan, Tim C. Holgate, Søren Linderoth, and Nini Pryds, "*Segmented thermoelectric oxide-based module*," Energy, under review, (2014).

[5] Li Han, Ngo Van Nong, Thanh Hung Le, Tim Holgate, Nini Pryds, Michitaka Ohtaki, and Søren Linderoth, "*The Influence of* α*- and* γ*-*Al_2O_3 *Phases on the Thermoelectric Properties of Al-doped ZnO*," J. Alloys Compd. **555**, 291 (2013).

[6] Li Han, Thanh Hung Le, Ngo Van Nong, Nini Pryds, and Søren Linderoth, "*The Influence of Spark Plasma Sintering Temperature on the Microstructure and Thermoelectric Properties of Al,Ga Dual-Doped ZnO*," J. Electron. Mater. **42**, 1573 (2013).

[7] Pham Hoang Ngan, Dennis Valbjørn Christensen, Gerald Jeffrey Snyder, Le Thanh Hung, Søren Linderoth, Ngo Van Nong, and Nini Pryds, "*Towards High Efficiency Segmented Thermoelectric Unicouples*", physica status solidi (a) 211: 9–17 (2014).

[8] Li Han, Ngo Van Nong, Wei Zhang, Thanh Hung Le, Tim Holgate, Kazunari Tashiro, Michitaka Ohtaki, Nini Pryds, and Søren Linderoth, "*Effects of morphology on the thermoelectric properties of Al-doped ZnO*", RSC Adv. **4**, 12353 (2014).

Conference Presentations

[1] Le Thanh Hung, Li Han, Eugen Stamate, Benjamin Balke, Pham Hoang Ngan, Søren Linderoth, Ngo Van Nong, and Nini Pryds, "*Preparation and characterization of segmented p-type* $Ti_{0.3}Zr_{0.35}Hf_{0.35}CoSb_{0.8}Sn_{0.2}/Ca_3Co_4O_9$" Part of: Proceedings of the MRS 2013 Fall Meeting, 2013, Presented at: Materials Research Society 2013 Fall, Boston (Oral).

[2] Le Thanh Hung, Ngo Van Nong, Pham Hoang Ngan, Li Han, Tim Holgate, Søren Linderoth, and Nini Pryds "*Fabrication and performance of high temperature segmented thermoelectric oxide-based module*" Part of: Proceedings of the 32nd International Conference on Thermoelectrics, 2013, Presented at: 32nd International Conference on Thermoelectrics, 2013, Kobe (Poster).

[3] Le Thanh Hung, Ngo Van Nong, Søren Linderoth, and Nini Pryds, "*High-temperature segmented thermoelectric oxide module using p-type $Ca_3Co_4O_9$ and n-type $ZnAlO/CaMn_{0.95}Nb_{0.05}O_3$ legs*", Presented at: 6th International Workshop on Advanced Materials Science and Nanotechnology, 2012, Ha Long City (Oral).

[4] Le Thanh Hung, Ngo Van Nong, Pham Hoang Ngan, Dan Eriksen, Li Han, Søren Linderoth, and Nini Pryds, "*High-temperature Oxide Thermoelectric Modules With p-type $Ca_3Co_4O_9$ and n-type Al-doped ZnO Legs,*" Presented at: 31st International & 10th European Conference on Thermoelectrics, 2012, Aalborg (Oral).

[5] Le Thanh Hung, Ngo Van Nong, Li Han, Dang Le Minh, Nini Pryds, and Søren Linderoth, "*High-temperature Thermoelectric Properties of $Ca_{0.9}Y_{0.1}Mn_{1-x}Fe_xO_3$ ($0 \leq x \leq 0.25$)*" Part of: Proceedings of the E-MRS 2012 Spring Meeting, 2012, Presented at: European Materials Research Society 2012, Strasbourg (Poster).

List of Figures

List of Tables

Chapter 1 Introduction

In this chapter, the basic principles of thermoelectric effects, materials, and modules are introduced. It also contains an overview of current high-temperature non-segmented and segmented thermoelectric modules, and their typical applications and developing progress. An outline of the thesis is presented at the end of this chapter.

1.1 Thermoelectric effects

The thermoelectric effect is the direct conversion of a temperature gradient to electricity (Seebeck effect) and vice versa (Petier effect). Since this study mainly focuses on power generation, the Seebeck effect will be described in more detail.

The Seebeck effect was discovered in 1821 by the physicist and chemist Dr. Med. Thomas Johann Seebeck (1770–1831) [1,2]. In general, the Seebeck effect can be described as shown in Figure 1.1a, b. When a temperature gradient is applied to a thermoelectric material (often a doped semiconductor), the majority charge carriers (electrons for *n*-type material and holes for *p*-type material) will thermally diffuse from the hot side (more energy) to the cold side (less energy) together with carrying the charge. As a result of this thermal diffusion of charge carriers, an electrostatic potential (voltage) is created. The polarization of charge carriers between the hot side and the cold side keeps the balance in this electric field, and the voltage drop across the material is called thermo power or Seebeck voltage, as presented in Fig. 1.1b. Thus, the Seebeck coefficient α is the ratio of potential difference (ΔV) and temperature gradient (ΔT), which can be expressed as:

$$\Delta V = \alpha \, \Delta T \tag{1.1}$$

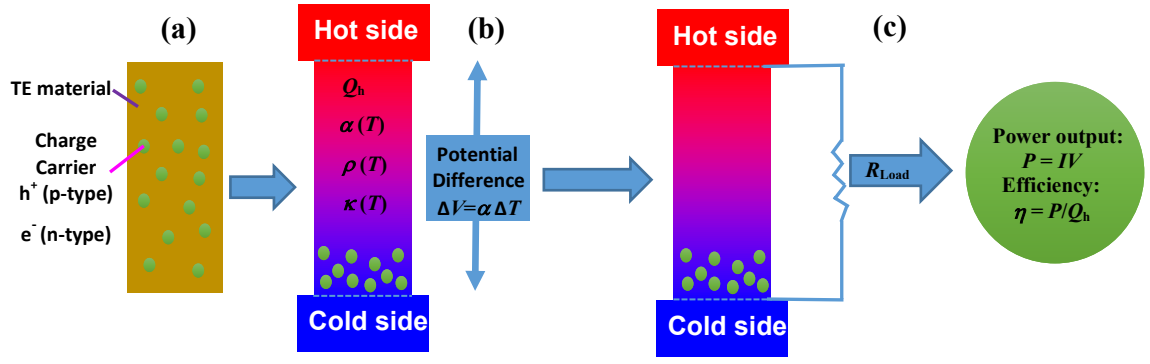

Figure 1.1 Schematic of Seebeck effect in a thermoelectric material. (a) The thermoelectric material contains majority charge carriers of *p*-type or *n*-type. (b) A potential difference is built up when applied a temperature gradient on the thermoelectric material. (c) The power output generates in the completing circuit apply an external load.

An output power generates when an electrical connection to an external load is established on the hot side and the cold side. Since the electric field due to a temperature gradient results in a positive

voltage for a *p*-type material and a negative voltage for an *n*-type material, *p*- and *n*-type materials are usually connected to form a thermocouple. The heat to electricity conversion efficiency is then defined as the total electric power output, *P*, divided by the total heat input on the hot side, Q_h, which can be written as:

$$\eta = \frac{P}{Q_h} \tag{1.2}$$

1.2 Thermoelectric figure-of-merit and materials

The efficiency of material is evaluated by the figure-of-merit *z* or the dimensionless figure-of-merit *zT*, which can be expressed as

$$zT = \frac{\alpha^2}{\rho\kappa}T \tag{1.3}$$

where α, ρ, κ, and *T* are the Seebeck coefficient, electrical resistivity, thermal conductivity, and absolute temperature, respectively. The concept of figure-of-merit was first proposed by a Russian physicist, Abram Fedorovich Ioffe, in 1949.

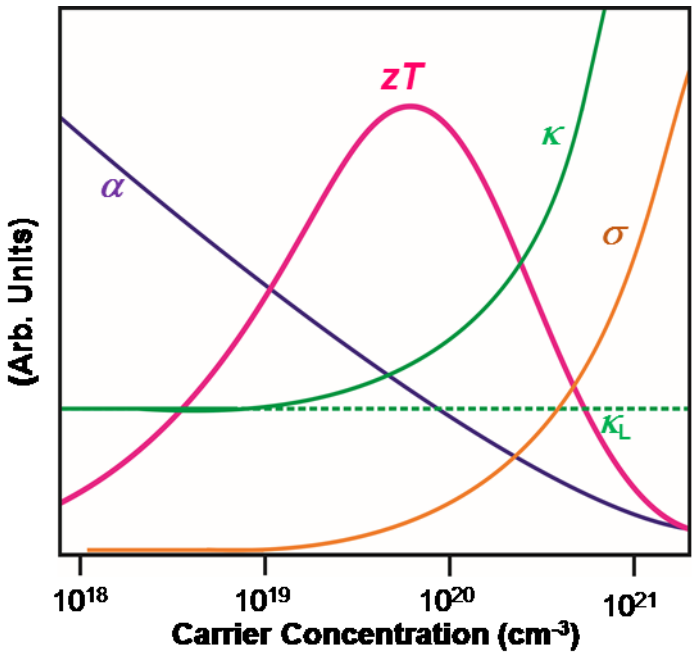

Figure 1.2 Schematic dependence of *zT*, Seebeck coefficient, electrical conductivity (1/ρ) and thermal conductivity on the carrier concentration of a thermoelectric material [3].

It can be seen from equation (1.3) that high *zT* requires a high value of Seebeck and a low value of electrical resistivity and thermal conductivity in a material, as presented in Figure 1.2. The good thermoelectric materials are of carrier concentrations of 10^{19} and 10^{21} carriers/cm^3 [3]. The optimization of the thermal conductivity is complicated by the heat transport including lattice and electronic thermal conductivity.

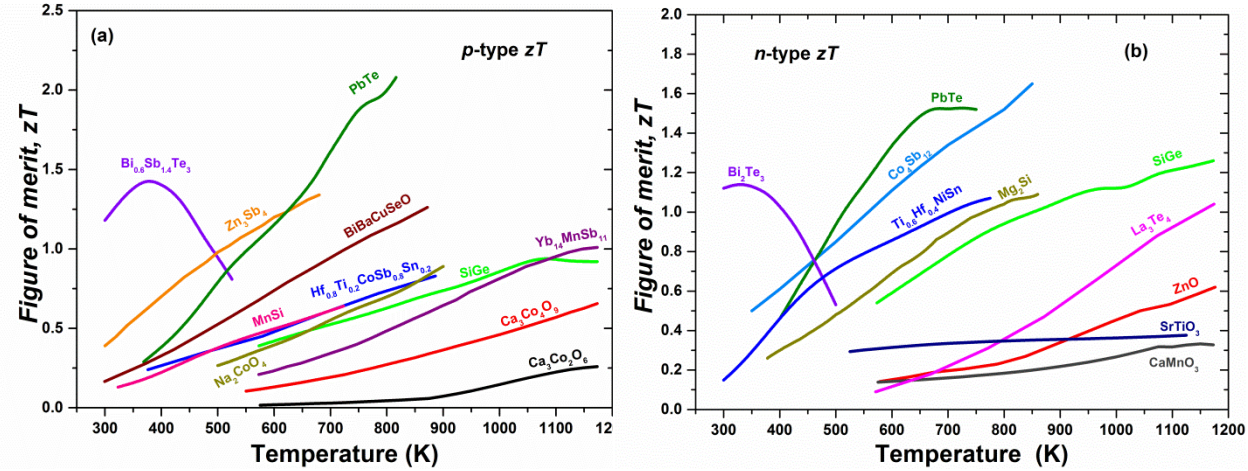

Figure 1.3 The material figure-of-merit, zT, of selected state-of-the-art p-type (a) and and n-type (b) for various temperature range.

Figure 1.3 shows the dimensionless figure-of-merit, zT, as a function of temperature for state-of-the-art TE materials. The new approach of nanostructured thermoelectric material has recently been used in reducing the lattice thermal conductivity. The results show very promising values with the peak zT reached at about 2.2 at 915 K [4] for polycrystalline PbTe compounds or zT = 2.6 at 923 K for SnSe single crystals [5].

1.3 Thermoelectric power generation

1.3.1 Thermoelectric module

The thermoelectric modules usually consist of several to hundreds thermoelectric couples of p-type and n-type materials, which are connected electrically in series and thermally in parallel, as shown in Figure 1.4. The top and bottom sides of the module are often covered by substrates that made by material with good thermal conductance and electrical insulation such as aluminum oxide (Al_2O_3) or aluminum nitride (AlN).

A thermoelectric generator uses heat flow across: heat absorbed and rejected at the hot side and the cold side of the module, respectively, to power output through an external circuit. The voltage output of the module is generated from the Seebeck effect. In case of the open-circuit, the output voltage (V_{OC}) can be expressed as [6,7]:

$$V_{OC} = S = n\int_{T_c}^{T_h}\{\alpha_p(T) - \alpha_n(T)\}dT \tag{1.4}$$

where T_h and T_c are the hot and cold side temperatures, n is the number of p-n couples, α_p and α_n are the Seebeck coefficients of p- and n-type legs, respectively.

The thermoelectric elements are connected electrically in series. Thus, the total resistance of the

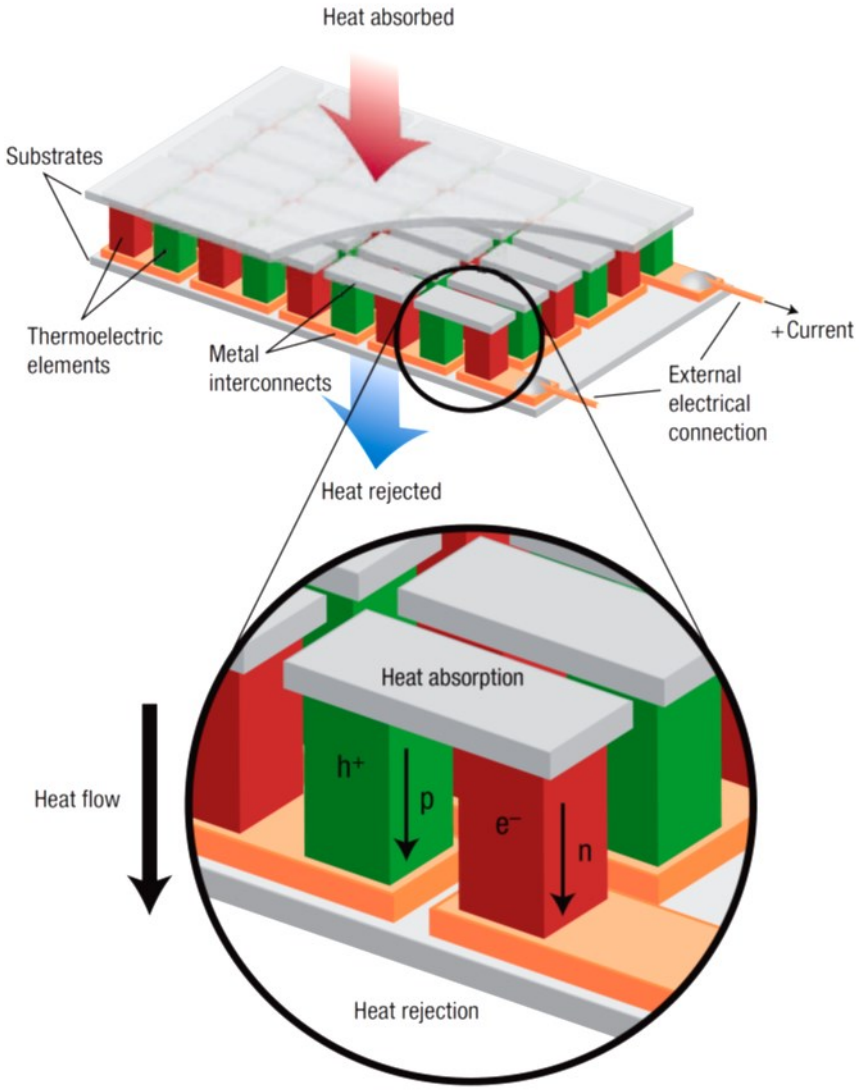

Figure 1.4 Schematic thermoelectric module consists of 27 couples of *p*-type and *n*-type with the direction of heat and charge flows. The figure is taken from Ref. [3].

module, R_{int}, can be approximately defined by

$$R_{int} = n\left(\frac{\rho_n l}{A_n} + \frac{\rho_p l}{A_p}\right) + R_c \tag{1.5}$$

here, l is the length of the legs, A_n and A_p are the cross-sectional area of *p*- and *n*-type legs, respectively, and R_c is the total contact resistance, which includes the electrical contact resistances at the joined part of the leg i.e. the hot and cold side junctions.

Similarly, the total thermal conductance of the module, K, can be determined by

$$K = n\left(\frac{\kappa_n A_n}{l} + \frac{\kappa_p A_p}{l}\right) + K_c \tag{1.6}$$

K_c is the total thermal losses including thermal contact, heat conductance and heat radiation losses. The magnitude of the output current, I, is proportional to the sum of the internal resistance of the

module R_{int} and the external resistive load R_{Load} and it is given by:

$$I = \frac{S}{R_{int}+R_{Load}} \tag{1.7}$$

The power output of the module as a function of V_{OC} and the resistance is given by

$$P = I^2 R_{Load} = S^2 \left[\frac{R_{Load}}{(R_{int}+R_{Load})^2}\right] \tag{1.8}$$

The maximum power output (P_{Max}) occurs when an external load resistance is equal to the internal resistance (R_{int}= R_{Load}). The load resistance needs to be continuously adjusted to match the internal module resistance to generate a thermoelectric module at its maximum output power.

$$P_{Max} = \frac{S^2}{4R_{int}} \tag{1.9}$$

The total heat absorbed at the hot side of modules is expressed as

$$\mathrm{Q} = IV_{OC}T - K\Delta T - \frac{1}{2}I^2R \tag{1.10}$$

The device figure-of-merit can, therefore, be calculated as

$$ZT = \frac{S^2 T}{KR} \tag{1.11}$$

The maximum conversion efficiency of thermoelectric module is often given as

$$\eta_{max} = \frac{T_h - T_c}{T_h} \frac{\sqrt{1+ZT}-1}{\sqrt{1+ZT}+\frac{T_c}{T_h}} \tag{1.12}$$

where ZT is approximated equally to the material figure-of-merit zT.

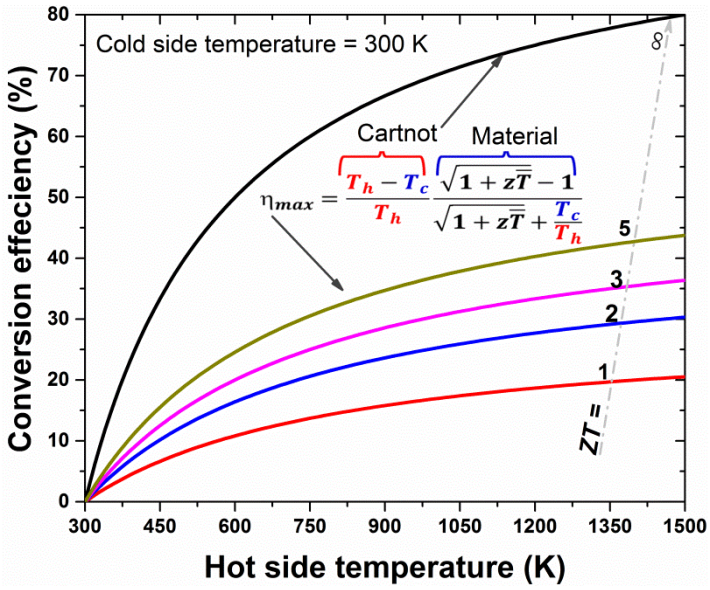

Figure 1.5 Calculated conversion heat-electricity efficiency as a function of temperature and thermocouple device figure-of-merit.

Figure 1.5 displays the conversion efficiency as a function of ZT and temperature differences. The first term of equation (1.12), $\frac{T_h - T_c}{T_h}$ is known as the Carnot efficiency which is the upper limited

conversion efficiency at infinity *ZT*. The maximum conversion efficiency of module increased with increasing the hot side temperature as a result of high Carnot efficiency contribution. Therefore, high temperature thermoelectric module is of great interest in high temperature heat-electricity conversion e.g. waste heat recovery from steel industrial and transportation sectors.

1.3.2 High temperature oxide thermoelectric modules

Oxide thermoelectric materials, consisting of abundant elements, have low-cost and environmentally-friendly processing, and hence, have attracted great interest in the area of advanced renewable energy. Many modules have been fabricated and characterized using a different combination of *p* and *n*-type of TE oxide materials such as *p*-type $Ca_3Co_4O_9$ and *n*-type $CaMnO_3$ or ZnO [8–11] or *p*-type $NaCo_2O_4$ and *n*-type ZnO [5, 7], etc. The power generation characteristics of different oxide modules are summarized in Table 1.1.

Table 1.1 Research progress on the power generation characteristics of oxide thermoelectric modules.

Ref.	Year	Materials	No. *p*-*n* couples	Jointing technique	T_{hot} (K)	ΔT (K)	V_0 (V)	P_{max} (mW)	Legs-size (mm)	Power Density (mW/cm^2)
[13]	2001	*p*-$Ca_{2.7}Bi_{0.3}Co_4O_9$ *n*-$Ca_{0.92}La_{0.08}MnO_3$	8	Pt paste	773	390	0.9	63.5	3×3	44.1
[14]	2006	*p*-$Ca_{2.7}Bi_{0.3}Co_4O_9$ *n*-$La_{0.9}Bi_{0.1}NiO_3$	140	Ag paste	1072	551	4.5	150	1.3×1.3×5	31.7
[5]	2006	*p*-$NaCo_2O_4$ *n*-$Zn_{0.98}Al_{0.02}O$	12	Diffusion welding	839	462	0.8	58	3×4×10	20.1
[16]	2006	*p*-$Ca_{2.7}Bi_{0.3}Co_4O_9$ *n*-$CaMn_{0.98}Mo_{0.02}O_3$	8	Ag paste	897	565	1	170	5×5×4.5	42.5
[7]	2007	*p*-$NaCo_2O_4$ *n*-$Zn_{0.98}Al_{0.02}O$	12	Diffusion welding	934	455	0.8	52.5	3×4×10	18.2
[17]	2007	*p*-$Ca_{2.7}Bi_{0.3}Co_4O_9$ *n*-$CaMn_{0.98}Mo_{0.02}O_3$	8	Ag	1273	975	0.7	340	5×5×4.5	85
[18]	2011	*p*-$Ca_3Co_4O_9$ *n*-$(ZnO)_7In_2O_3$	44	Ag paste	1100	673	1.8	423	p:15×15× 27 n:15×15×18	2.1
[9]	2014	*p*-$Ca_3Co_4O_9$ *n*-$Zn_{0.98}Al_{0.02}O$	6	Ag	773	248	0.12	2.26	4×4×10	1.2

* Only the modules with the number of *p*-*n* couples from 4 or higher are selected.

As seen in Table 1.1, although many combinations of *p*-*n* couples have been employed in the oxide modules, its performance i.e. voltage, and current output are still relative low compared with modules constructed from metallic alloys; even the experimental value of the conversion efficiency

has not been reported yet on those oxide modules. The highest estimated number is still lower than 2%. One of the main reasons for this low result is the low performance of oxide materials in the low-temperature range (< 750 K). To overcome the limitation mentioned above, new strategies on improved material of *zT* and a new concept in module design and fabrication are needed.

1.3.3 Segmented thermoelectric modules

From equation (1.12) and Fig. 1.5, one can see that in order to achieve high conversion efficiency of a thermoelectric power generator (TEG), both high figure-of-merit and large temperature differences are desired. The material *zT* is computed from α(T), ρ(T), and κ(T) using Eq. (1.3) strongly depend on temperature. The large temperatures that drop along the leg are dominated by large change in the *zT* curve. In general, each material exhibits a peak *zT* value, which is defined as their optimum working temperature interval. It means that for a given temperature interval, one material may have its highest *ZT* while in another temperature interval, a second material will have a higher *ZT*. Therefore, a TEG constructed from one material is limited to a particular operation temperature range which is determined by the type of materials used. To overcome the limitation of generator built-up from one material, TEGs based of two or more materials can solve this problem by either cascaded or segmented generators as schematically showed in Figure 1.6 [6].

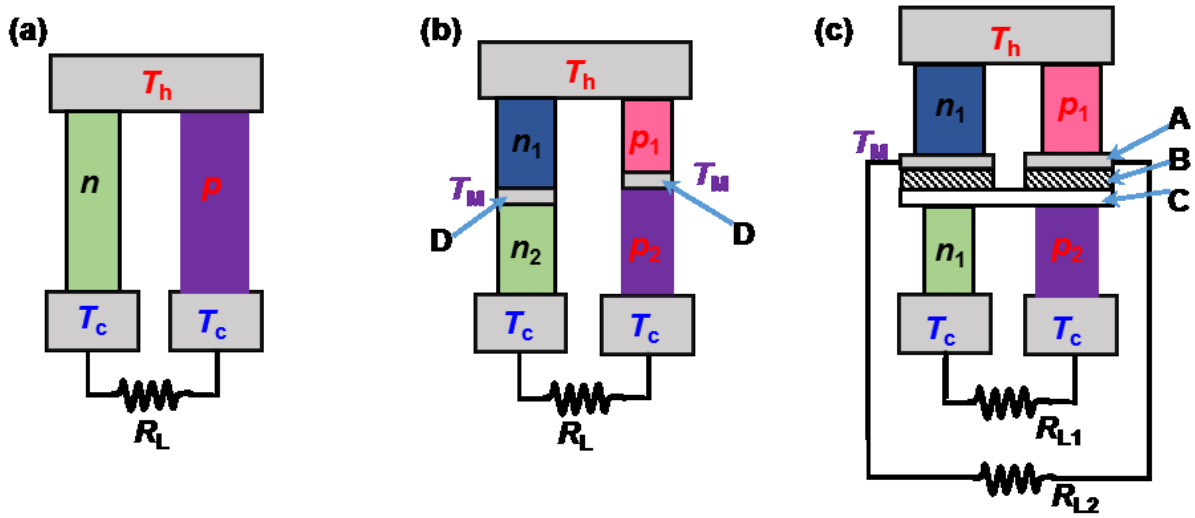

Figure 1.6 Schematic drawing of one-stage of (a) single material, (b) segmented two-material and (c) two-stage of cascaded thermoelectric generators. A, C and D are materials with high electrical and thermal conductivity. B is a material with high thermal conductivity and electrically insulating, in order to expect that there is no temperature gradient between A and C [6].

Fig. 1.6a presents a typical *p-n* unicouple made of a single material, for example, a low-temperature BiTe, a high-temperature oxide or SiGe. In BiTe-based module, the maximum highest temperature at the hot side is 450 K and 300 K at the cold side. When the temperature at the hot side is higher than 450 K, the material based on BiTe cannot be sustained because of oxidation, decomposition or volatility of the *p* and/or *n* legs. For modules made of oxide or SiGe-based materials, their peaks *zT* values are obtained at 1000 K as presented in Fig. 1.2 so that the highest device performance can only be reached at temperatures between 750 and 1200 K. Ideally, a

combination of two types of material in one device is expected to achieve higher efficiency by either segmenting or cascading, as shown in Fig. 1.6b, c [19–23]. A cascaded generator consists of two stages, where each stage is fabricated by a single *p*- and *n*-type TE material (Fig. 1.6c). A high-temperature material can be used for the hottest stage (>750 K) and then a metal alloy of high TE performance in the mid-low temperature range (<750 K). The stages have their electrical circuit and optimal load resistance, it often requires an external device to achieve maximum performance at each stage. Therefore, the major loss will appear on the electric connector as either heat conductance loss due to the low electrical resistivity or Joule heating loss due to the high electrical resistance [19,24]. In addition, a cascaded generator requires good electrically insulating, good thermal conductivity, and thermal contact at interfaces. Thus, it is a complicated technique in the practice of module construction. In contrast, a segmented generator uses only a single electric circuit, and each leg is designed by a combination of different materials with their highest value of *ZT*. However, in order to obtain an improved efficiency of a segmented TEG, the selected materials have to be compatible, namely, the difference in the compatibility factor ($s = \frac{\sqrt{1+zT}-1}{\alpha T}$) is within a factor of two [25,26].

With the above-mentioned advantages, the modules based-segmented legs have been broadly studied and the Jet Propulsion Laboratory (JPL-NASA) is the frontier research group in segmented generators aiming for space application. Many studies were conducted and focused on achieving as high of a thermal-electrical conversion efficiency as possible at various temperature differences, as shown in Table 1.2.

Table 1.2 Research progress on the power generation characteristics of segmented thermoelectric modules.

Ref.	Year	Materials	No. seg.	T_{hot} (K)	ΔT (K)	Test condition	Eff. (%)	
							Cal.	Exp.
[27]	2013	*p*- $Ce_{0.9}Fe_{3.5}Co_{0.5}Sb_{12}/Yb_{14}MnSb_{11}$ *n*- $CoSb_3/La_{3-x}Te_4$	2	1246	773	Vacuum	-	15
[28]	2011	*p*-$Bi_xSb_{2x}Te_3/Ag_{0.9}Pb_9Sn9Sb_{0.6}T_{20}$ *n*-$Bi_2Te_{3x}Se_x/Ag_{0.86}Pb_{19+x}SbTe_{20}$	2	670	358	Vacuum	9	6.56
[29]	2009	*p*-Bi_2Te_3/PbTe *n*- Bi_2Te_3/TAGS	2	803	510	Vacuum	-	10
[30]	2003	*p*-$Bi_2Te_3/CeFe_4Sb_{12}$ *n*- $Bi_2Te_3/CoSb_3$	2	885	569	Vacuum+Ar	12	5.5

It can be seen from Table 1.2 that remarkable results were obtained with the based-segmented generator. The highest efficiency was attained at about 15% in the segmented TEG using *p*-$Ce_{0.9}Fe_{3.5}Co_{0.5}Sb_{12}/Yb_{14}MnSb_{11}$ and *n*- $CoSb_3/La_{3-x}Te_4$ on the hot side 1246 K and a cold temperature of 473 K [27]. The BiTe materials are preferred to use in the segmented leg at low temperatures [20,28–36] since both *p*- and *n*-type BiTe-based materials are hitherto the best-performing materials in the low-temperature range (300 K to 500 K), as shown in Fig. 1.3. While the *p*-type material e.g. PbTe [28,29], Zn_4Sb_3 [35,37], MnSi [38] and $CeFe_4Sb_{12}$[33,39], and *n*-type $CoSb_3$ [34,35,37], TAGS [28] applied for segmented legs in the higher temperature region (500 K to 800 K). For the efficiency

of the segmented generator, the experimental results are always smaller than the calculated one due to a large contribution of thermal and electrical losses. The main factors that affected the conversion efficiency are summarized by the following [20]:

- The material figure-of-merit of segments is determined by a small temperature gradient, ΔT, less than 10 K, while the devices work under large temperature differences (200 to 700 K).
- The compatibility factor, s.
- Interfacial contact (electrical and thermal) resistance.
- Heat losses on the side of the leg.

According to results reported in Refs. [20,28,32,36,40], the functionally graded materials have been suggested as a good solution to reduce contact resistance. In this way, the material zT could be optimized by tuning the carrier concentration layer by layer in the TE leg; the contact resistance between layers can be therefore negligible. However, the grade materials required similar sintering conditions i.e. temperature, pressure and environment, which lead to limits in materials selection. Generally, the previously-studied materials were only based on metallic compounds and the segmented TEG measurements conducted in high vacuum or inner gas in order to protect the legs against oxidation or sublimation. In some cases the leg is coated by protected layers [33]. Therefore, application of these generators often requires an encapsulation process, which increases the capital cost of modules. For high temperatures > 1000 K, the segmented materials used in Ref. [27,35] contained large quantity ratios of rare earth elements, e.g., La, Yb, and Ce, which are very expensive and might only be used for space application. Other inexpensive materials such as high-temperature oxide and mid-temperature half-Heusler alloy, have not been investigated yet. Thus, a study of segmentation based on cheap, stable, scalable materials is necessary to bring up low-cost and high efficiency TEG for high temperatures in waste heat recovery.

1.4 Thesis outline

The thesis consists of seven chapters which cover the content of modeling segmented thermoelectrics, development of oxide materials, the joining between oxides and metal, oxides and alloys, and the construction of segmented thermoelectric oxide-based legs/modules. The main scientific results and findings are presented in Chapter 3 to Chapter 6.

Chapter 1 presents the basic principles of thermoelectric effects, materials and modules. An overview of the current study on high-temperature thermoelectric modules was also given.

In Chapter 2, all the typical experimental methods and characterization techniques used in the thesis will be presented. They include: spark plasma sintering, joining legs, and module fabrication, as well as contact resistance and module measurements. Other experiments for particular works will be described in detail in each sub-chapter.

Chapter 3 will describe the modeling on segmented thermoelectrics used to predict the performance of non-segmented and segmented leg/unicouples. Based on the study on the efficiency ratio i.e. the conversion efficiency vs. materials cost, it shows that some oxides such as layered-cobaltite $Ca_3Co_4O_9$ and doped ZnO are good candidates for hot side materials for segmentation. Various state-of-the-art metallic materials are selected based on the calculation results of the

compatibility factor and the maximum total conversion efficiency of the segmented legs. The evaluation was carried out using a one-dimensional (1D) numerical modeling. The influence of the interfacial contact resistance on the performance of the segmented legs/unicouples is also considered and discussed in this chapter.

Chapter 4 presents the study on *n*-type oxide materials of $CaMnO_3$. For the investigation of $CaMnO_3$, the $Ca_{0.9}Y_{0.1}Mn_{1-x}Fe_xO_3$ system with $0 \leq x \leq 0.25$ was prepared, in which Ca-site was substituted with Y at a fixed concentration and Mn-site was partly replaced by Fe. The structural and the thermoelectric properties of these materials are investigated in detail. The influence of Y and Fe doping at Ca- and Mn-sites, respectively, on the crystal structure, is carefully studied by the Rietveld refinement analysis. The correlation between the crystal structures and the thermoelectric properties is discussed.

In Chapter 5, segmentation of the half-Heusler $Ti_{0.3}Zr_{0.35}Hf_{0.35}CoSb_{0.8}Sn_{0.2}$ (HH) and the non-doped layered-cobaltite $Ca_3Co_4O_9$ is investigated both by modeling and experiments. A 4 *p*-*n* couples segmented thermoelectric generator comprised of the segmented HH/$Ca_3Co_4O_9$ as *p*-legs and *n*-legs 2% Al-doped ZnO was fabricated and characterized at various hot side temperatures up to 1173 K. The power generation characteristics obtained experimentally for the correlation with theoretical calculations are compared with a non-segmented oxide module built up from *p*-leg $Ca_3Co_4O_9$ and *n*-leg 2% Al-doped ZnO.

Chapter 6 focusses on the fabrication and characterization of a high efficiency segmented *p*-leg building up from half-Heusler $Ti_{0.3}Zr_{0.35}Hf_{0.35}CoSb_{0.8}Sn_{0.2}$ (HH) and doped $Ca_{2.8}Lu_{0.15}Ag_{0.05}Co_4O_{9+\delta}$. It is found that a maximum efficiency of 5% is attained at a temperature gradient of about 756 K. In this chapter, the influence of the contact resistance on the total conversion efficiency was also evaluated by modeling, and correlated with the experimental results.

Finally, Chapter 7 is summary of the main findings and results of the thesis. Some future works and outlooks are also mentioned at the end of this chapter.

Chapter 2 Experimental methods

The experimental methods used in the thesis include powder synthesis, bulk material sintering, joining two dissimilar materials, module construction process, and characterization of materials, single legs, segmented legs, contact resistance and device performance. In this chapter, only the typical methods are focused on and described in detail. Other common experiments will be mentioned in each sub-chapter.

2.1 Spark Plasma Sintering

In the fabrication of thermoelectric materials, the most-effective method used to enhance thermoelectric performance is to make bulk nanostructured materials (pellet) consisting of separate nanoparticles connected through "particle's neglect" and its grain size is retention. In those materials with nanostructures, their thermal conductivity could be reduced as a result of the increase in phonon scattering. Therefore, retention of nano-size particles in bulk form during the sintering process is of prime importance. In the sintering technique, spark plasma sintering (SPS) is known as a powerful tool that can not only be used for consolidation/synthesis [41], but can also be used for coating/joining materials [42,43]. The SPS's principle is based on an electric current assisted sintering technique, which simultaneously applies an electric current and mechanical pressure, as

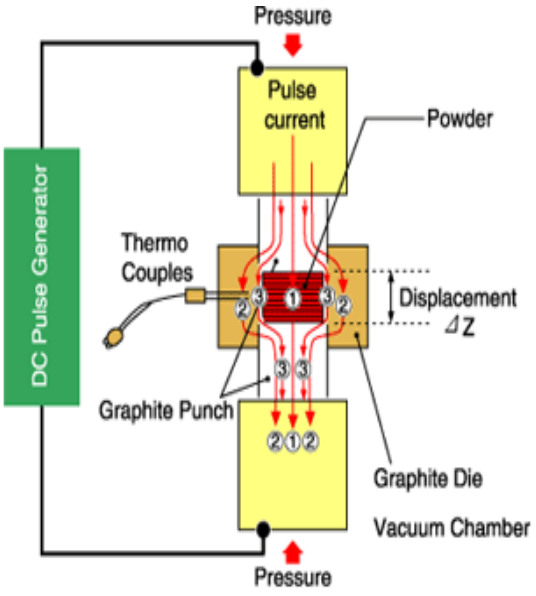

Figure 2.1 Schematic representation of the park plasma sintering (SPS) process [135].

schematically shown in Figure 2.1. With this technique, the sintered powders are consolidated and simultaneously densified with desired shape and density [41]. It can be seen from Fig. 2.1 that the pulse electric current can pass through both of the die and the sintered powder. The SPS processes can be used in efficient heat input, particularly when electrical-insulating die is used the electric current is applied to the electrical conductance punch and powder for an extremely short duration (a

few microseconds). The heat, therefore, will be concentrated on the sintered elements which avoid a large quantity of heat loss to the surrounding environments. In another way, the SPS can be used as a fast hot pressing technique without the current going through samples. In this thesis, the SPS will be used for sintering oxide materials and semimetal half-Heusler materials as well as the joining of metallic alloy, oxide compounds, and module fabrication.

For the sintering materials process, after calcination, milling, sieving, and checking the phase of samples, the obtained powders were covered with graphite paper and put into graphite die. The densified processing was carried out using a spark plasma sintering system (SPS). The SPS unit of Dr. Sinter 515S (Syntex Inc., Japan) was used, with a pulsed direct current regulated by the on/off settings, with each pulse lasting 3.3 ms and having a 12:2 on/off ratio. For the sintering parameters, a constant uniaxial pressure of 50 MPa, was used. The samples were heated to setting temperature e.g. 1123 K for *p*-type oxide $Ca_3Co_4O_9$ and $Ca_{2.8}Lu_{1.5}Ag_{0.05}Co_4O_{9+\delta}$ while a uniaxial pressure of 50 MPa was applied for holding 5 min. During the experiment, the temperature, applied pressure, and displacement or shrinkage of the sample were recorded. The as-prepared samples were then polished to remove the graphite foil. The details of these works can be seen elsewhere [8,44–46].

2.2 Joining segmented leg

Metal-ceramic joining has a long history. Egyptians first used it to cover their enamels several centuries B.C [47]. In general, joining provides a new structured ceramics in a way that manufacturing components cannot be made in one piece. This method is cheaper than others [47,48]. There are several joining techniques which can be roughly classified as: joining with intermediate material and direct joining. In direct joining, joint materials are directly connected to each other using co-sintering, explosion welding, and diffusion welding. A strong mechanical interface connection is usually provided, but its electrical and thermal properties are relatively poor. In contrast, when joining with intermediate material e.g. soldering and brazing uses a molten filler metal, the joint materials are connected by filler media so that its interface is normally not deformed after joining.

In order to obtain high performance of segmented thermoelectrics, the joint processes are required to achieve good interface connection with a low electrical and a high thermal contact. In this thesis, the silver brazing joint was

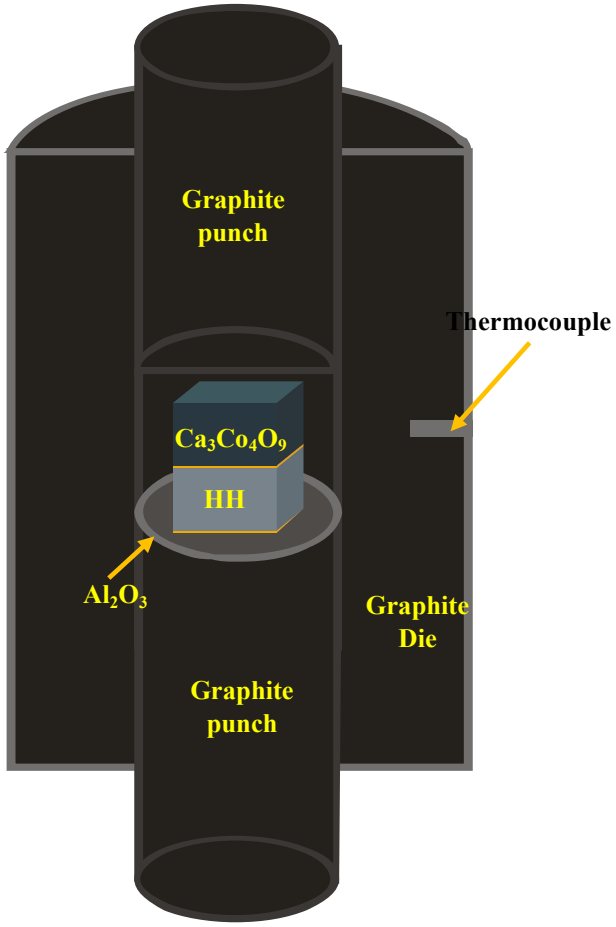

Figure 2.2 Schematic configuration of the brazing joining oxide-metallic alloys used spark plasma sintering as hot press without current passing through the sample.

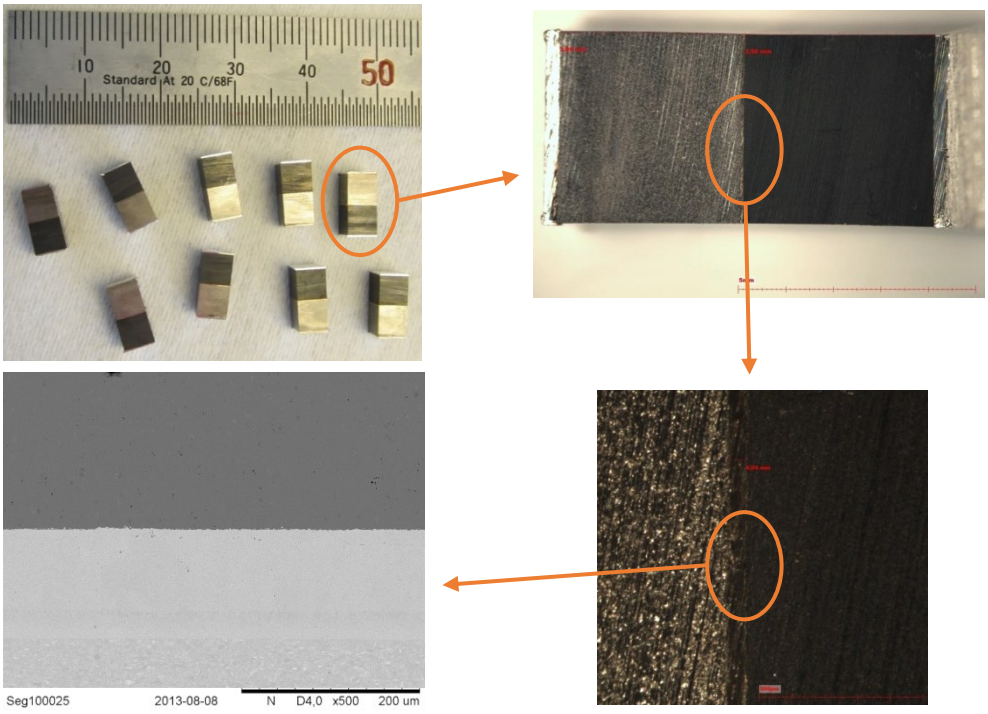

Figure 2.3 A proven picture of segmented half-Heusler/oxide legs were successfully joined by silver brazing method.

carefully investigated on metallic half-Heusler alloys and oxide $Ca_3Co_4O_9$ compounds. To fabricate the segmented legs, the obtained pellets of $Ca_3Co_4O_9$ and HH were cut, polished and then cleaned with acetone, isopropyl alcohol and deionized water and finally dried with nitrogen. The length of oxide and half-Heusler materials was designed as the demanding hot and cold side temperatures. 150 µm thick Ag foil with a purity of 99.99% was used as the standard joining material between the half-Heusler and the oxide, while 400 µm thick Ag foil was used to make electrodes. In order to avoid the influence of high density current of SPS on the thermoelectric properties of joint legs, the top and bottom of the sample were covered with a thin layer of alumina oxide that allows good heat conductance from graphite die as showed in Figure 2.2. The brazing process was conducted in a vacuum using an SPS under 20 MPa at 973 K for 10 min. Figure 2.3 shows some typical segmented legs of Ag/$Ca_3Co_4O_9$/Ag/HH/Ag obtained with a good adhesion at the interface.

2.3 Module fabrication

Figure 2.4 shows the whole process of module fabrication used in this thesis. The materials of *p*- and *n*-type were first optimized the fabrication condition and followed by characterization step. Using the measured data of materials properties, the modelling is used to calculate and design appropriate output performance. The legs were then cut into fixed dimensions according to the calculation results. For the fabrication of module substrate, the Ag electrodes were first fabricated on top of two alumina substrates by hot-pressing at 1073 K for 2 h in air. The substrate was chosen to fit the size of the graphite die used in an SPS process. *p*-legs and *n*-legs were attached to these designed

substrates. The whole module was then placed in a graphite die and hot-pressed at 973 K under a pressure of about 20 MPa in Ar atmosphere. It is seen from Fig 2.4 that all the step connection in series if any step is failed the process is required restart from fabricated material step.

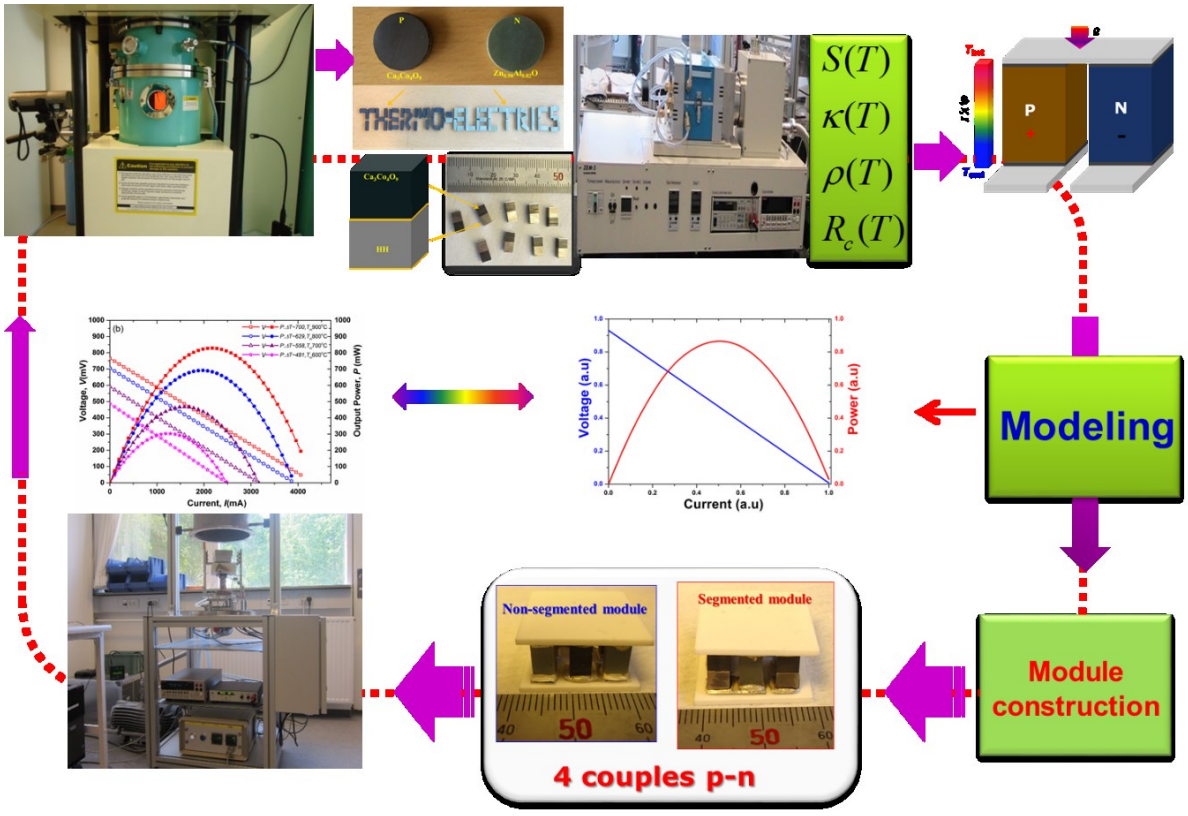

Figure 2.4 Schematic of the whole thermoelectric module construction process from sintering and characterized materials to modelling, built up and test modules.

2.4 Characterization

2.4.1 Contact resistances

Figure 2.5a presents a schematic configuration that used to determine the interfacial contact resistance (R_c) by linear extrapolation of the resistance (R) versus the distance of measuring probes (x_n to 0) and subsequent subtraction of the contribution from the alloy between the probe lead and the interface. The contact resistance is actually the interface resistance, which is multiplied by the cross-sectional area of the interface to give the area specific resistance of the interface (ASR). Fig. 2.5b illustrates a real picture of the fixture used to determine contact resistance of leg with electrode in this thesis. The fixture consists of long alumina tube which intergraded electrical connection wires and thermocouple. A spring system was installed to get a good thermal contract of two-end electrodes as showed in Fig. 2.5b. The terminal connected to the cooling water at the end of fixture

allowed measurement disregard thermal effect on the electrical conductivity of connected wires. As presented in Fig. 2.5a, the accuracy of the measurement also affected by the distance of probes placed on the surface of the sample. Shorter distance between two-probe higher uncertainties appears. It is normally required long sample (> 10 mm). However, the homogeneous temperature distributes on the long samples might difficult to archive. Therefore, the short segmented legs were employed other way that is demonstrated in Fig. 2.5c for determining the contact resistance between the different TE materials in a segmented leg using the ZEM-03. In the ZEM-03 system allows a small temperature gradient on sample (< 0.5 K) during measure electrical resistance. In addition, the one-dimensional heat transfer in the measured sample will minimize the influence of heat losses. The contact resistance can be determined by measuring the electrical resistivity of individual TE materials (V_1 and V_3) and the resistance across the interface of the segmented materials (V_2). By measuring the contact resistances of the sample with various cross-sectional areas (A_R), the ASR is then calculated from the slope of the fitted R^{-1}/A_R curve using the least-squares method.

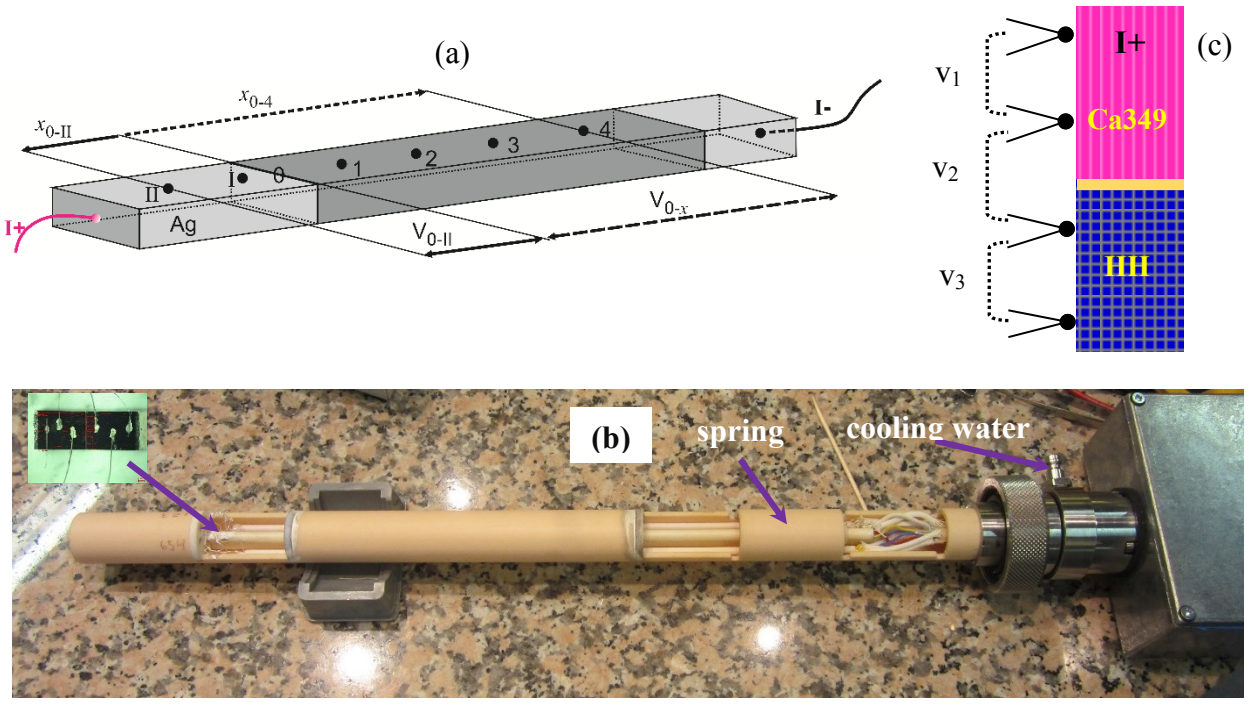

Figure 2.5 Schematic of the fixture used to measure the electrical contact resistances. (a) The darker shaded material is the $Ca_3Co_4O_9$ or 2% Al doped ZnO and the sign convention of the current is for forward current mode. (b) A real picture of a fixture used to measure ASR. (c) Schematic configuration of the voltage probes along the segmented leg

2.4.2 Module power generation characteristics

The power generation characteristics of the segmented legs and modules were performed in air using an in-house Rig-test system. The Rig-test consists of temperature and electrical measurement parts which controlled by a PC via feedback signal from multi-channel Keithley. The heat flux values at the hot and the cold sides of TEG can be determined through the measurement of temperatures

dropped on two heat transfer blocks at hot and cold sides. The voltage of the cell test is directly determined on the output wires of the device while current values are calculated in term of voltage dropped on shunt resistance and the value of electric load device. The heater made of SiN compounds that allow to use an extremely high ramping rate (6000 ^{o}C/hour) and also be able to apply high pressure on its surface as presented in Figure 2.6a.

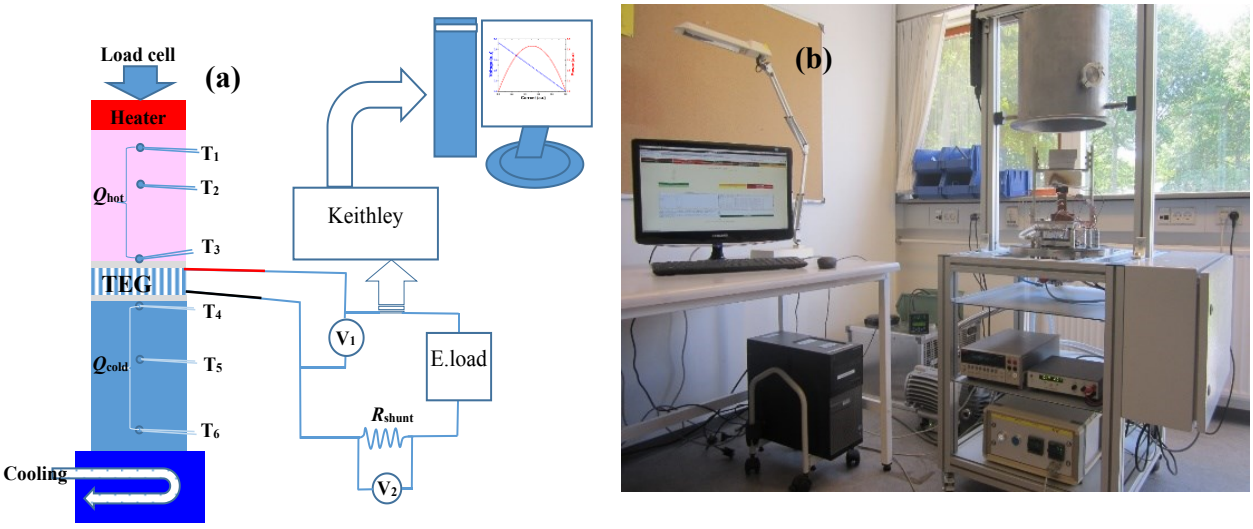

Figure 2.6 (a) Schematic illustration of module tester. (b) The complete view of the Rig-test used to measure the power generation characteristics of legs and modules in this thesis.

The *I-V* curves of legs and modules were automatically measured at different ΔT by sweeping electronic load that has the current value from 0 to 15 A with a minimum step of 1 mA. The controlled software system is based on Apache web server software (Open Source Software, OSS) and allow flexibility about the type gas control, cycling, long-term stability tests, etc. The measurements can be able to perform both power generation and heat pump effects in one setup. For the measurement of single leg, in order to define the accurate temperature difference across the leg, 0.5 mm n-type thermocouple was directly inserted inside the Ag electrodes at the vicinity of the top part of the leg. The thermocouple at the hot side is also used for setting up the PID of the heater controller. To minimize the heat losses during the test the heater was covered with a thick layer of silica felts. The efficiency of a TEG can be calculated in term of measured electric power out and the heat flux values at hot and sides. However, the heat transfer block at hot side is needed to be well-defined which mean all the heat losses including convection, radiation and conductance are negligible. The functionality of the test-rig is calibrated by measuring the commercial G2-40-0329 Tellurex Corperation module [49].

Chapter 3 Segmentation of low-cost, high efficiency oxide-based thermoelectric materials

Abstract

Thermoelectric (TE) oxide materials have attracted great interest in advanced renewable energy research owing to the fact that they consist of abundant elements, can be manufactured by low-cost processing, sustain high temperatures, be robust and provide long lifetime. However, the low conversion efficiency of TE oxides has been a major drawback limiting these materials to broaden applications. In this work, theoretical calculations are used to predict how segmentation of oxide and semimetal materials, utilizing the benefits of both types of materials, can provide high efficiency, high temperature oxide-based segmented legs. The materials for segmentation are selected by their compatibility factors and their conversion efficiency versus material cost, i.e. "efficiency ratio". Numerical modelling results showed that conversion efficiency could reach values of more than 10% for unicouples using segmented legs based *p*-type $Ca_3Co_4O_9$ and *n*-type ZnO oxides excluding electrical and thermal losses. It is found that the maximum efficiency of segmented unicouple could be linearly decreased with increasing the interfacial contact resistance. The obtained results provide useful tool for designing a low-cost and high efficiency thermoelectric modules based-oxide materials.

The work presented in this chapter is submitted to Physica Status Solidi A: Applications and Materials Science 2014: Le Thanh Hung, Ngo Van Nong, Søren Linderoth, and Nini Pryds, "*Segmentation of low-cost, high efficiency oxide-based thermoelectric materials*".

3.1 Introduction

Thermoelectric generators are solid-state devices which directly convert heat to electricity without any moving part, and maintenance free, and hence have attracted increasing interest in waste heat recovery which improves the overall energy efficiency used of many various applications [3,50–52]. A typical TEG usually constructs from *p*- and *n*-type TE materials and its maximum thermal-electricity conversion efficiency, η_{max}, can be expressed as

$$\eta_{max} = \frac{T_h - T_c}{T_h} \frac{\sqrt{1+z\overline{T}}-1}{\sqrt{1+z\overline{T}}+\frac{T_c}{T_h}} \tag{3.1}$$

where T_h is the hot side temperature, T_c is the cold side temperature, $\frac{T_h - T_c}{T_h}$ is known as the Carnot efficiency, $\overline{T} = \frac{T_h + T_c}{2}$, and the TE material figure of merit z (=$\alpha^2/\rho\kappa$, whereα, ρ, and κ are the Seebeck coefficient, the electrical resistivity, and the thermal conductivity, respectively), and T is absolute temperature. It is obvious from Eq. (3.1) that besides the zT, large temperature spans also are required to increase in the conversion efficiency. Under such high-temperature conditions, oxide TE materials are of the most promising candidates due to their natural durability, robustness to the surroundings in additional with their low-cost and abundant source compared with conventional TE intermetallic compounds [53–57]. They have therefore been widely studied with the aim to improve the value of zT using for example heavy element doping [44,58,59], nano-structuring [53,54,60], nanowire and optimized morphology [61–63], and nano-inclusion [58,64]. During recent years, remarkable results have been reported on Al and Ga dually doped-ZnO [59,61,62,65,66] and $Ca_3Co_4O_9$ nanocomposite [44,67,68] with the peak zT reached the values of 0.65 at 1200 K and 0.61 at 1140 K, respectively. However, the performance of oxide modules are still relative low, and so far their estimated conversion efficiency is smaller than 3% [69], which is due to the low thermoelectric performance of oxide materials in the low temperature range. To overcome the limitation mentioned above, two possible solutions are available: cascaded and segmented generators. In a cascade module the performance can be enhanced by stacking several TE modules on top of each other. This type of module is often requires an external device to accumulate the maximum performance in each single module. The main losses in such module are either heat conductance loss due to the low electrical resistivity or Joule heating loss due to the high electrical resistance [17]. In contrast, a segmented generator uses only single electric circuit, and each leg is designed by a combination of different materials with their highest value of zT. In order to obtain an improved efficiency of a segmented TEG the selected materials have to be compatible i.e. the difference in their compatibility factor ($s = \frac{\sqrt{1+zT}-1}{\alpha T}$) must be within a factor of two [25,26]. With the purpose of pursuing low-cost, and high-conversion efficiency of TEGs based-oxide, we have in this study, applied one-dimensional (1D) numerical modelling using various state-of-the-art intermetallic compounds TE materials to achieve high conversion efficiency of the segmented legs. The influence of the interfacial contact resistance on the total conversion efficiency of the segmented unicouple is also evaluated.

3.2 Calculation model

In order to evaluate the efficiency of non-segmented and segmented TE elements, a one-dimensional (1D) model of the thermoelectrics is used and detailed of the model can be found in [8,24,70]. In this calculation, the efficiency of segmented and non-segmented TE elements was calculated under the ideal conditions, i.e. neglecting all the heat losses, thermal and electrical contact resistances, but including all the thermoelectric effects. The calculations can, therefore, be considered as an upper limit for the obtainable actual efficiency in experiments. The 1D model solves for the reduced current density u (= $J/\kappa\nabla T$), which is defined as the ratio between the electrical current density (J) and the heat flux by conduction (κ). The values of u at any temperature along the leg can be determined by solving the following differential equation [16]:

$$\frac{du}{dT} = u^2 T \frac{d\alpha}{dT} + u^3 \rho\kappa, \tag{3.2}$$

The differential equation is valid for both non-segmented and segmented legs if – for the latter – the material properties are changed from one material to another at a particular known interface temperature (T_M) where the segments meet.

The reduced current densities at the various temperatures can be calculated by the following equation:

$$\frac{1}{u_n} = \frac{1}{u_{n-1}} \sqrt{1 - 2u_{n-1}^2 \overline{\rho\kappa} \Delta T} - \bar{T}\Delta\alpha \tag{3.3}$$

Here, $\Delta\alpha = \alpha(T_n) - \alpha(T_{n-1})$ and $\overline{\rho\kappa} = [\rho(T_n)\kappa(T_n) + \rho(T_{n-1})\kappa(T_{n-1})]/2$. From u values, the reduced (η_r) and total efficiency (η_{leg}) of a segmented or non-segmented leg can be found:

$$\eta_r = \frac{u(\alpha - u\rho\kappa)}{u\alpha + \frac{1}{T}} \tag{3.4}$$

$$\eta_{leg} = 1 - \frac{\alpha_c T_c + \frac{1}{u_c}}{\alpha_h T_h + \frac{1}{u_h}} \tag{3.5}$$

Where u_c and u_h are values of the reduced current density at the cold and hot side temperatures, respectively.

As for the segmented legs, η_{leg} is determined by an optimum interface temperature T_M. To simplify the choice of temperature, T_M often sets to be the temperature where the material at the cold side reaches its maximum zT.

The value of u_h is a free parameter varied in the equation (3.5) to get the highest efficiency, a Fortran program was used to numerically calculate the value of u(T) in this work. In practice, u_h is varied by changing the load resistance. When an n-type leg and a p-type leg are connected electrically in series and thermally in parallel to form a unicouple, the efficiency is calculated by

$$\eta_{unicouple} = 1 - \frac{\alpha_{c,p} T_{c,p} + \frac{1}{u_{c,p}} - \alpha_{c,n} T_{c,n} - \frac{1}{u_{c,n}}}{\alpha_{h,p} T_{h,p} + \frac{1}{u_{h,p}} - \alpha_{h,n} T_{h,n} - \frac{1}{u_{h,n}}} \tag{3.6}$$

Where the subscripts *n* and *p* denote the *n*- and *p*-type legs. Numerically, both $u_{p,h}$ and $u_{n,h}$ are optimized simultaneously.

With the purpose of evaluating the relationship between material cost and conversion efficiency, the term "efficiency ratio" which calculated using the peak *zT* value divided by material cost has been used in Ref. [56]. Although the "efficiency ratio" can somehow describe qualitative the feasibility and the sustainability features of *p*- and *n*-type TE materials, the peak *zT* excluded temperature dependent thermoelectric properties and boundaries condition i.e. hot and cold side temperatures of TE leg in which might be not fully reflected conversion efficiency. In this study, we have used the exact solution [24] to find the efficiency value of the leg (η_{leg}) in a particular temperature interval instead of using the peak *zT* value. The "efficiency ratio", η_{ratio}, therefore, can be expressed as:

$$\eta_{ratio} = \frac{\eta_{leg}}{M_{cost}} \tag{3.7}$$

Where, η_{leg} is calculated from Eq. (3.5) and M_{cost} is the TE material cost. M_{cost} is computed by the sum of the costs of raw materials and processing that need to produce 1 mol of e.g. $Ca_3Co_4O_9$.

3.3. Results and discussion

3.3.1 Material selection

In this section, the selection of materials for segmentation will be based on the figure-of-merit *zT*, the "efficiency ratio" and the compatibility factor. Other properties including thermal expansion coefficient, chemical stability, toxicity and mechanical properties are not taken into account for the theoretical model. However, it should be noted that these properties are very important in practical of TEG manufacturing and its long term stability.

On the material figure- of- merit zT

Figure 3.1 displays the material figure-of-merit *zT* and the compatibility factor *s* of collected state-of-the-art *p*- and *n*-type materials in the low temperature range from low (300 to 450 K), mid (450 to 800 K) and high (800 to 1200 K). In this collection, the *zT* and *s* factors were computed from the temperature dependence of thermoelectric properties i.e. Seebeck coefficient, electrical resistivity and thermal conductivity (not show here). In the low temperature range, BiTe [71,72] alloys monopolize with the peak *zT* value over 1, while in the mid-temperature range PbTe [4] compounds are leading TE materials which can reach the *zT* values of 2 at 750 K and 1.6 at 700 K for *p*- and *n*-type, respectively. Although presented the highest peak *zT* value, the compounds contain Pb element which might be concerned to environmentally unfriendly issues [73]. To avoid environmental impact, studies on less toxic compounds have been flourishing recently, among those materials, *p*-type of Zn_3Sb_4 [74], MnSi [38], HH [75],

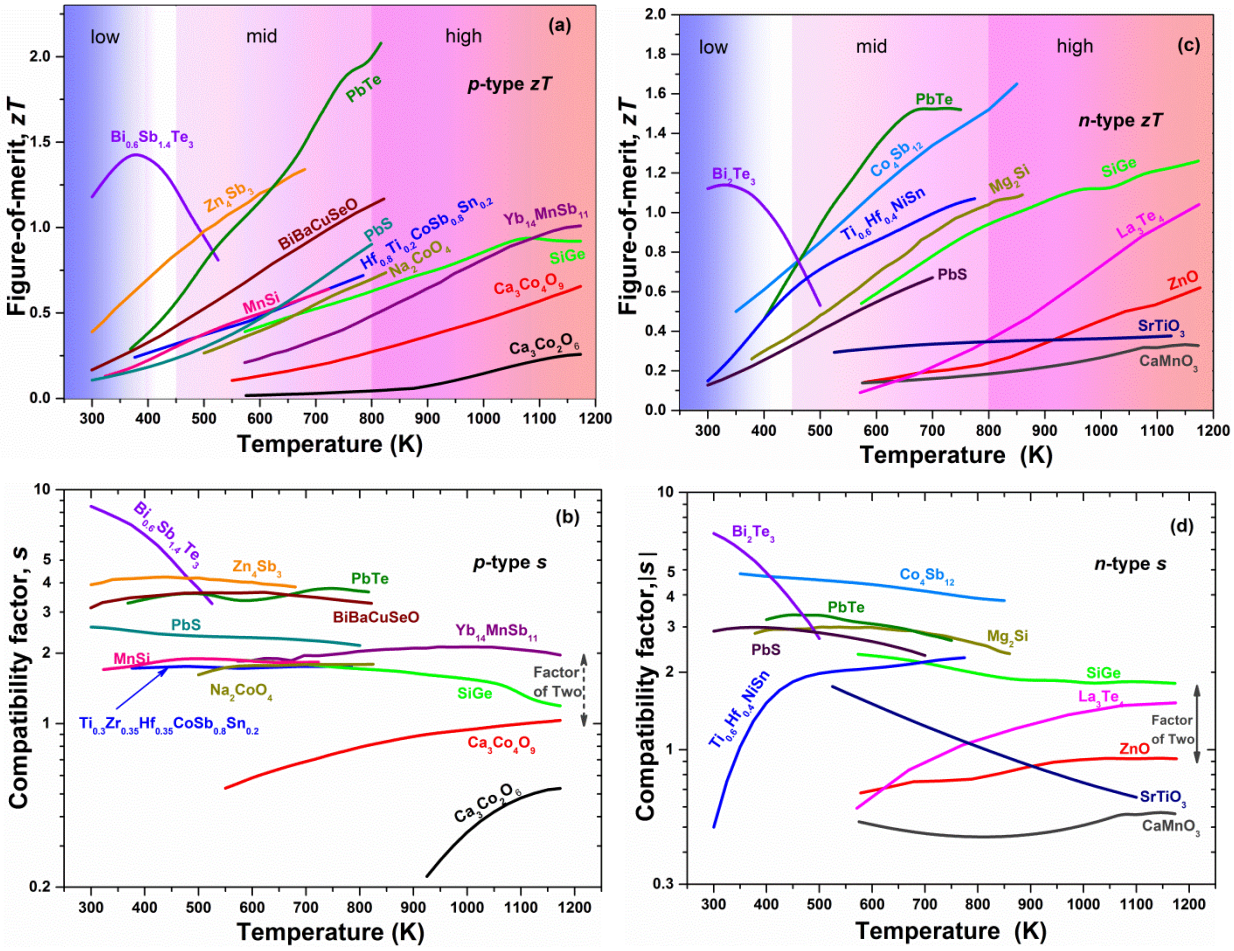

Figure 3.1 The material figure-of-merit *zT* and their compatibility factor s of selected state-of-the-art *p*-type (a and b) and *n*-type (c and d) for various temperature range.

BiBaCuSeO [76] , and *n*-type of CoSb [77], HH and Mg_2Si [78] these show for example very promising *zT* values of ~1.7 for *n*-type CoSb [77] at 850 K and ~ 1.4 for *p*-type Zn_3Sb_4 [74]. In the high temperature range, conventional alloys e.g. the *p* and *n*-type SiGe [79,80] and state-of-the-art intermetallic compounds such as *p*-type $Yb_{14}MnSb_{11}$ [81] and *n*-type La_3Te_4 [82] are the materials with the highest peak *zT* values of about 1. However, a high-temperature TEG constructed from these materials often need to have encapsulation to prevent against the oxidation, sublimation and volatility processes when devices operated at high temperature [83,84]. Besides, the metallic compounds containing Tellurium tend to decompose and release harmful vapor in the high-temperature application [56]. In contrast, oxide materials such as $Ca_3Co_4O_9$ [44], $Ca_3Co_2O_6$ [85], Na_2CoO_4 [86], ZnO [61,62,65], $SrTiO_3$ [87], $CaMnO_3$ [88] are environmental friendly operating for high-temperature usage. Although the peak *zT* values of oxide materials have relative low as compared with traditional intermetallic compounds, their chemical composition contains abundant elements and low-cost of raw and material processing [56]. Therefore, it will be useful to develop a criterion, which include the materials performance but also the overall cost of these materials.

On the "efficiency ratio"

In order to provide a better comparison of materials selection in term of efficiency and material cost, the efficiency ratio, η_{ratio}, is exploited to appraise candidates for high temperature TE materials. In this calculation, the costs of raw materials that need to produce 1 mol of e.g. $Ca_3Co_4O_9$ nanocomposite [44], doped-ZnO [65], SiGe [79,80], La_3Te_4 [82] etc. are taken from Alfa Aesar [89] with the purity of elements selected corresponding to its references. The bulk manufacturing cost of these materials are followed the data previously reported by LeBlanc et al. [90]. The manufacturing cost of $Si_{80}Ge_{20}$ and oxides are about 1.1 \$/kg, while that of $Yb_{14}MnSb_{11}$ or La_3Te_4 is 1.26 \$/kg [90]. As shown in Fig. 3.2a, the metallic compounds containing rare earth elements have the highest value of material cost, e.g. $Yb_{14}MnSb_{11}$ and La_3Te_4 are four orders more expensive than oxide materials. The values of η_{ratio} are calculated from Eq. (3.7), the efficiency of single materials was computed using Eq. (3.5) with fixed cold and hot side temperatures of 300/1173 K and without including electrical and thermal losses. As seen from Fig.3.1a, c, the peak zT values of oxide materials are only 60% that of compared e.g. SiGe or skutterudite, but their efficiency ratios are higher by a factor of five for *p*-type and twenty for *n*-type materials as clearly shown in Fig. 3.2b. This result points out that doped-ZnO and $Ca_3Co_4O_9$ nano-composite are the good candidates as hot-side materials for low-cost high performance segmented legs.

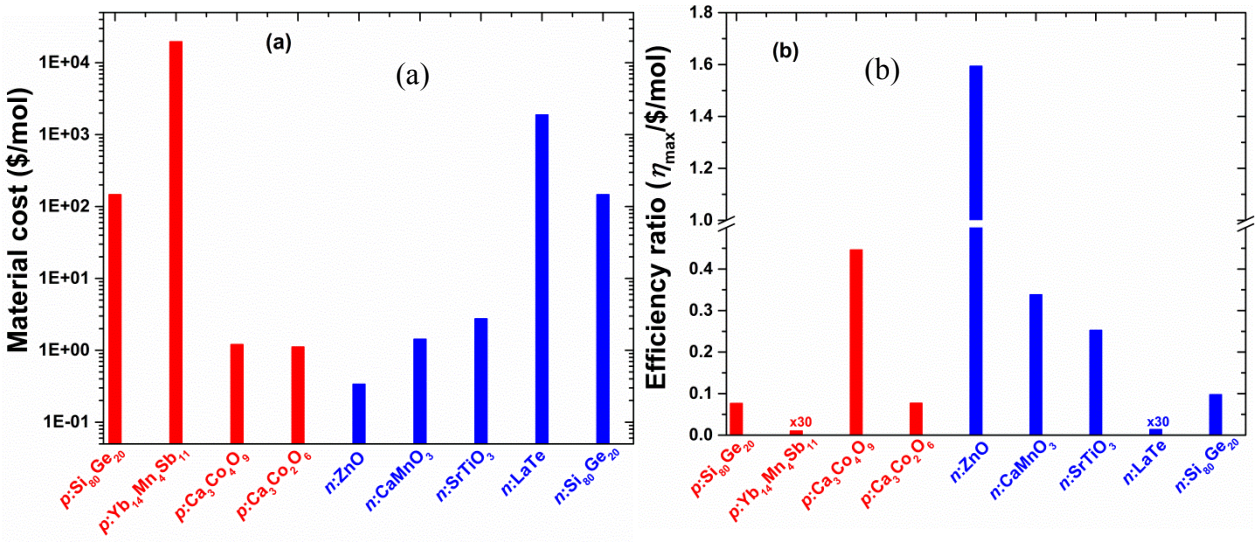

Figure 3.2 A plot of price in dollars per mole (a) and (b) efficiency ratio for various high-temperature TE materials.

On the compatibility factor

Aforementioned, in order to ensure high conversion efficiency of segmented module the compatibility factor of materials to be segmented must be first considered. Here, the rule of thumb is that the difference in compatibility factors between two materials should be within a factor of two [25,26]. To evaluate the effect of compatibility, *s*, segmented legs containing compatible and non-compatible materials segmentations of *n*-type leg contain doped ZnO and HH or CoSb alloys were chosen. Fig. 3.3 shows the temperature dependence of the compatibility factor, the relative current density, and the reduced efficiency as well as the absolute efficiency as a function of relative current

density for ZnO, HH, CoSb, segments of HH/ZnO and CoSb/ZnO. It can be seen that the *s* values of CoSb are three times as much larger than that of ZnO, while the difference in s between HH and ZnO is less than a factor of 2 (Fig. 3.3a). The relative current density *u* was computed from the temperature dependence of thermoelectric properties e.g. Seebeck, electrical and thermal conductivity. Here, the value of u_h (T=T_{hot}) was numerically calculated in order to obtain the highest efficiency Eq. (3.5). It can be seen from Fig. 3.3a that the values of $u_{CoSb\text{-}ZnO}$ and $u_{HH\text{-}ZnO}$ start separating in the high temperature range. This is due to the fact that their *u* values are different at hot side temperature. Shown in Fig. 3.3b is the actual reduced efficiency that was calculated based on the *u* values using Eq. (3.4), and the maximum reduced efficiency ($\max\eta_r = \frac{\sqrt{1+zT}-1}{\sqrt{1+zT}+1}$) at u = s. The maximum reduced efficiency of CoSb is higher than that of HH due to its higher *zT*. However, the actual reduced efficiency of segmented CoSb/ZnO is lower than HH-ZnO over the whole temperature range. Eventually, even under a larger temperature span the maximum total efficiency of the segmented CoSb/ZnO leg was decreased by 3.5% as compared with non-segmented CoSb one (Fig. 3.3c). Strikingly, with the segmentation of HH and ZnO, the maximum total efficiency was increased by 6.3% as compared with non-segmented ZnO.

With the aim of pursing low-cost, high efficiency high-temperature TEG, based on η_{ratio} values *n*-type ZnO and *p*-type $Ca_3Co_4O_9$ were selected as the best candidates for the hottest part (773 K to 1173 K) of segmented leg. For these calculations, the temperatures of the legs were chosen to be 1173 K for the hot side and 300 K for the cold side. The materials, which can be segmented at different temperature ranges, are summarized in Table 3.1. The interface temperatures (T_M) between two materials were evaluated based on their *zT* and the *s* values as shown in Fig. 3.1. Due to

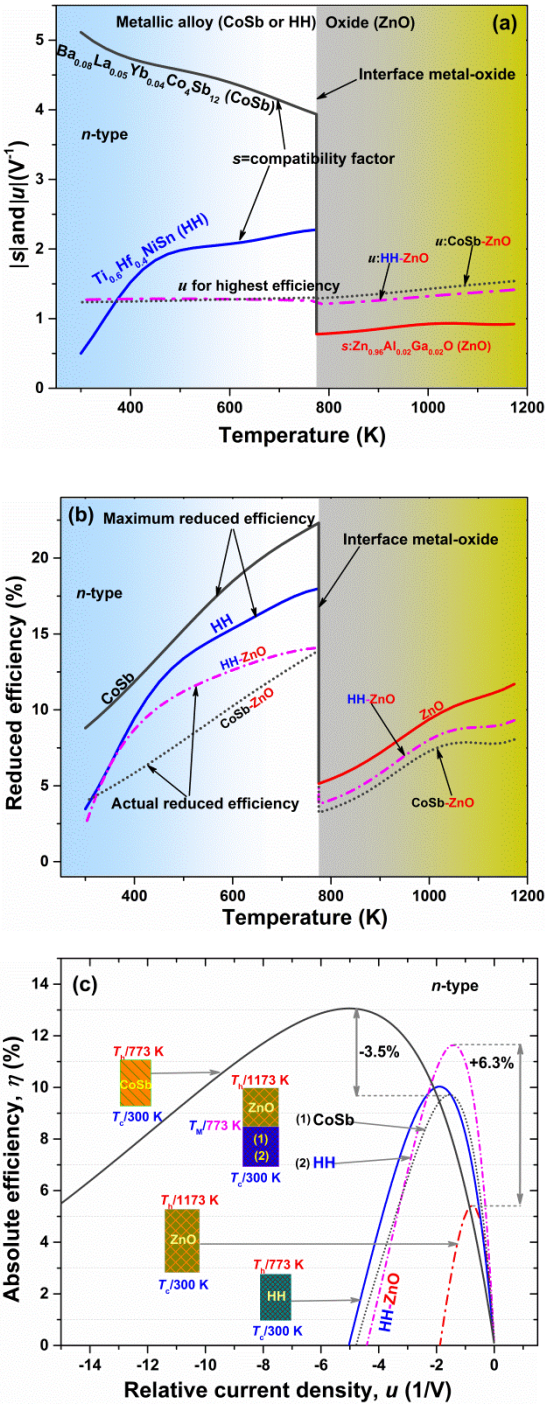

Figure 3.3 (a) Temperature dependence of the *s* and the *u*. (b) local and reduced efficiencies using value of *u* for highest efficiency compared to the maximum reduced efficiency for *n*-type segmented CoSb/ZnO and HH/ZnO legs. (c) Total efficiency of single components, incompatible segmented leg CoSb/ZnO and compatible segmented HH/ZnO.

the high performance of the BiTe compounds, in the low temperature range, they were selected for segmentation at the range of 300 K to 500 K for the *p*-type and 300 K to 450 K for *n*-type. However, since the compatibility factor of oxide does not match that of BiTe, they cannot directly segmented. Therefore, the HH (or PbTe) compounds were chosen as the best material to connect these two to form oxide/HH/PbT/BiTe.

Table 3.1 The possible materials for segmenting legs of *p*-$Ca_3Co_4O_9$ and *n*-ZnO

n-BiTe	*n*-PbTe	*n*-HH	*n*-ZnO	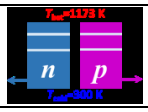	*p*-$Ca_3Co_4O_9$	*p*-HH	*p*-PbTe	*p*-BiTe
-	-	300←773	773←1173	two-segment	1173→773	773→300	-	-
300←450	-	450←773	773←1173	three-segment	1173→773	773→500	-	500→300
300←450	475←650	650←773	773←1173	four-segment	1173→773	773→650	650→500	500→300

3.3.2 Efficiency of individual segmented legs

Figure 3.4 shows the calculated maximum efficiency of non-segment, two-, three- and four-segments for *p*- and *n*-type legs. In these calculations, the hot and cold side temperatures of the legs were fixed at 300/1173 K without any thermal and electrical losses. It is clear from Fig.3.4 that segmentation increases the maximum efficiencies for both *p*- and *n*-type materials. Both conversion efficiencies and device ZTs are increased with increasing the number of segments. The increments in the efficiencies are 9.6% and 11.5% for *p*-type HH/$Ca_3Co_4O_9$, and *n*-type HH/ZnO two-segmented

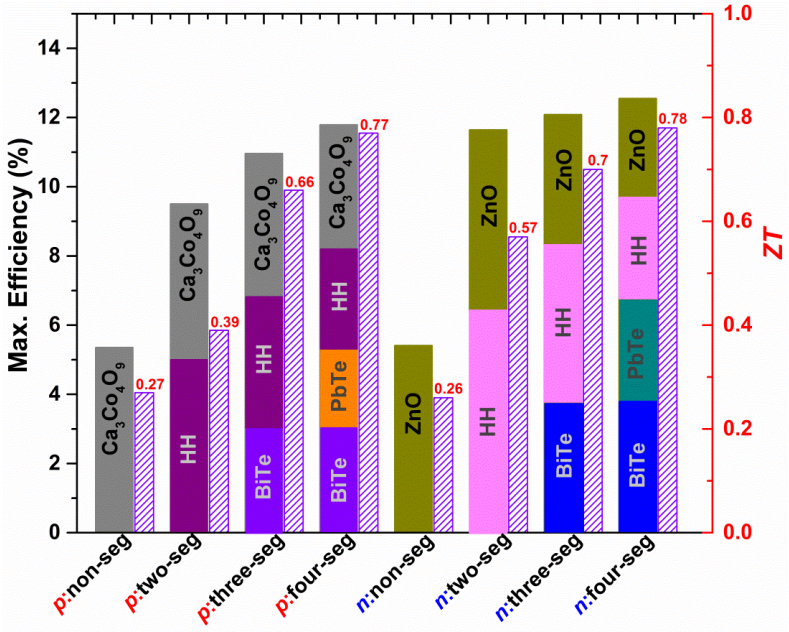

Figure 3.4 The diagram of the maximum total efficiencies of the state-of-the-art oxide-based segmented legs (solid column), and their device *ZT*s (pattern column).

legs, respectively as compared with 5.3% for single legs of oxide materials ZnO and $Ca_3Co_4O_9$. The highest efficiency of 11.7% for *p*- BiTe/PbTe/HH/$Ca_3Co_4O_9$ and 12.5% for *n*- BiTe/PbTe/HH/ZnO were calculated for four-segment legs.

When the reduced efficiency is equal to the maximum reduced efficiencies, i.e. $u = s$, the highest efficiency value of the legs can be achieved. As an example (Fig. 3.4), although three-segment *p*-type BiTe/HH/$Ca_3Co_4O_9$ has a higher value of ZT = 0.66 than that of two-segment *n*-type HH/ZnO (ZT = 0.57), the maximum total conversion efficiency attained for three-segment *p*-type (11%) is smaller than that for two-segment *n*-type (11.6%). This difference implies the importance of *s* and *u* values when designing segmented legs. These results also suggest that in additional to the improvement of materials *zT* values, optimized local compatibility factor is an efficient route that need to be considered [91,92].

3.3.3 Segmented unicouples

Combining the *p*- and *n*-type oxide-based segmented legs resulted in a unicouple whose efficiencies can be calculated by using Eq. (3.6). The highest calculated efficiency values for different unicouples are listed in Table 3.2. From Table 3.2, one can see that the efficiency of unicouples significantly increases with increasing the number of segments. The highest value of 12.2% was obtained for unicouple of *p*-BiTe/PbTe/HH/$Ca_3Co_4O_9$ and *n*-BiTe/PbTe/HH/ZnO four-segmented legs. For the chosen combinations of materials, an efficiency of more than 10% could be attained for unicouples of any of two segments e.g. *p*- HH/$Ca_3Co_4O_9$ and *n*-HH/ZnO (10.1%) or any of three segments of *p*-BiTe/HH/$Ca_3Co_4O_9$ and *n*-BiTe/HH/ZnO (10.9%). Although, the highest maximum efficiency of two-segment unicouple (10.1%) is 17% smaller than the one of four-segment (12.2%) the number of interfaces is also increased about 67% (from six to ten interfaces). Thus, the trade-off between the complicated legs production and the increment in conversion efficiency should be taken into account.

Table 3.2 Maximum efficiency of unicouples with various combination of *p*-*n* leg.

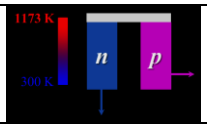	$Ca_3Co_4O_9$	HH/$Ca_3Co_4O_9$ (T_M/773 K)	BiTe/HH/$Ca_3Co_4O_9$ (T_M/500/773 K)	BiTe/PbTe/HH/$Ca_3Co_4O_9$ (T_M/500/650/773 K)
ZnO	5.3%	7.0%	7.5%	7.7%
HH/ZnO (T_M/773 K)	7.4%	10.1%	10.9%	11.3%
BiTe/HH/ZnO (T_M/450/773 K)	7.7%	10.7%	11.2%	11.9%
BiTe/PbTe/HH/ZnO (T_M/450/650/773 K)	7.8%	10.9%	11.7%	12.2%

As mentioned above, all efficiencies of segmented single legs and unicouples were calculated under the assuming a perfect thermal and electrical contact between two adjusted materials. The

contact resistance, is known as one of the main sources that detriment the performance of a TEG, especially for a segmented module which includes multiple number of interfaces, i.e. contact resistance [8,28,34]. In the current calculations, we have included a parameter called "resistance ratio", $\delta = R_c/R_{leg}$, which is defined as the total contact resistance (R_c) divided by the total electrical resistance (R_{leg}) for a TE leg. Fig. 3.5 presents calculations of efficiency of a segmented unicouple made of *p*-BiTe/HH/$Ca_3Co_4O_9$ and *n*-BiTe/HH/ZnO legs as a function of the resistance ratio at the hot side and cold side temperatures of 1173 K and 300 K, respectively.

It can be seen from Fig. 3.5 that the conversion efficiencies of segmented unicouple are linearly decreased with increasing the value of contact resistance. In practical, the contact resistance between metal-metal is in the range of 2 to 50 μΩcm^2 [93–95] and for oxide with metal electrode e.g. $Ca_3Co_4O_9$ and ZnO with Ag it is about 100 μΩcm^2 at about 1000 K [8,96]. As a result, the major contribution to the δ magnitude is usually attributed to the oxide-metal conjunctions. Therefore it is essential to be able to reduce the total contact resistance in the segmented legs based oxide. In addition, the value of δ not only depends on the total thermal contact resistance, but it also depends on the total electrical resistance of the legs, which is determined by the dimension of the leg, i.e. the

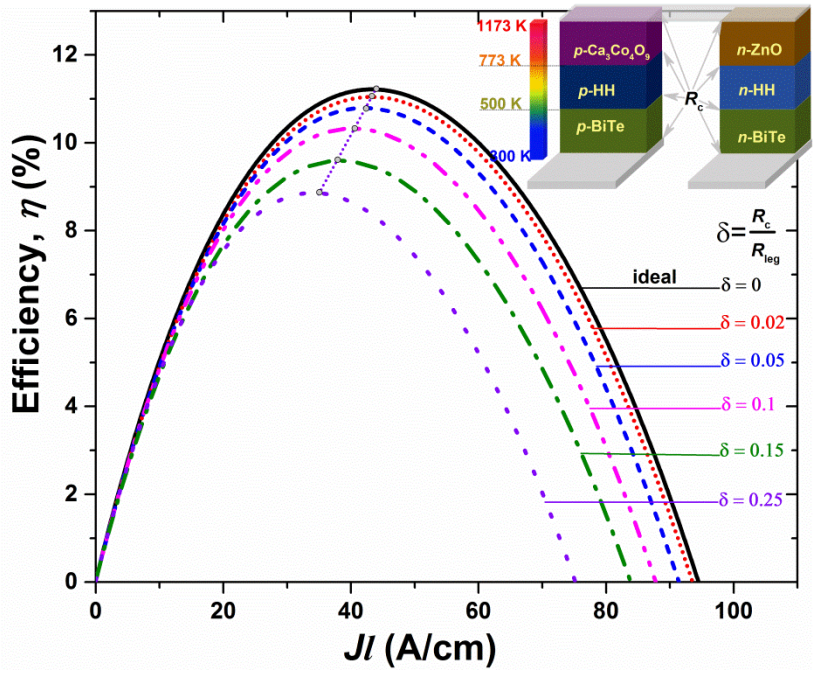

Figure 3.5 The influence of contact resistance on the total efficiency of unicouple comprised from *p*-BiTe/HH/$Ca_3Co_4O_9$ and *n*-BiTe/HH/ZnO.

length and cross-sectional area, that need also to be optimized. For example, for a given value of the electrical contact resistances, larger dimensions of a TE leg are often preferable to achieve a high efficiency. However in this case, the materials and manufacturing cost for fabrication such thermoelectric modules also need to be considered [90,97].

3.4 Conclusions

In summary, the low-cost, high efficiency oxide-based segmented legs/unicouples have been investigated using the numerical modelling. The materials to be segmented were selected based on their figure-of-merit, the "efficiency ratio" and their compatibility factors. The calculated results indicate that oxides materials are good candidates at the hot side for achieving low-cost, high performance segmented legs/unicouples. A maximum efficiency of more than 10% could be attained for the unicouples built up from segmented legs of *p*-$Ca_3Co_4O_9$ and *n*-ZnO with intermetallic compounds such as HH and BiTe. The modelling results have showed that in the building up TEG based segmented legs the trade-off between the increment in conversion efficiencies and the external factor i.e. complicated production and increasing interface contact resistances and should be taken into consideration. The obtained results suggest a tool to construct low-cost and high efficiency thermoelectric modules based on oxide materials for high-temperature power generation.

Chapter 4 High-temperature thermoelectric properties of $Ca_{0.9}Y_{0.1}Mn_{1-x}Fe_xO_3$ ($0 \leq x \leq 0.25$)

With the aim of the thesis is to develop low-cost, high-temperature TEG based oxide materials through the investigation in the Chapter 3 pointed out that the *p*- type nanocomposite $Ca_3Co_4O_9$ and the *n*-type doped ZnO materials are selected as the best candidates. The modules construction will be then used the oxide materials which are cooperated with two separate projects on development and processing of *n*-type, *p*-type oxide thermoelectric materials. The results have been published elsewhere [44,46,61,98]. As reported in the literature, so far, the studies indicated that *n*-type materials, such as ZnO, $SrTiO_3$, have much lower thermoelectric performance than their *p*-type counterparts. Therefore, in this chapter, the study of *n*-type of $Ca_{0.9}Y_{0.1}Mn_{1-x}Fe_xO_3$ is chosen as an alternative *n*-type oxide.

Abstract

Polycrystalline compounds of $Ca_{0.9}Y_{0.1}Mn_{1-x}Fe_xO_3$ for $0 \leq x \leq 0.25$ were prepared by solid-state reaction, followed by spark plasma sintering (SPS) process, and their thermoelectric properties from 300 to 1200 K were systematically investigated in term of Y and Fe co-doping at the Ca- and Mn-sites, respectively. Crystal structure refinement revealed that all the investigated samples have the O′-type orthorhombic structure, and the lattice parameters slightly increased with increasing Fe concentration, causing a crystal distortion. It was found that with increasing the content of Fe doping, the Seebeck coefficient of $Ca_{0.9}Y_{0.1}Mn_{1-x}Fe_xO_3$ tended to increase, while the tendency towards the electrical conductivity was more complicated. The highest power factor was found to be 2.1 $x10^{-4}$ W/mK^2 at 1150 K for the sample with $x = 0.05$ after annealing at 1523 K for 24 h in air. Thermal conductivity of the Fe-doped samples showed a lower value than that of the $x = 0$ sample, and the highest dimensionless figure-of-merit, zT was found to be improved about 20% for the sample with $x = 0.05$ as compared to that of the $x = 0$ sample at 1150 K.

The work discussed in this chapter is published in: Le Thanh Hung, Ngo Van Nong, Li Han, Dang Le Minh, Kasper A Borup, Bo B. Iversen, Nini Pryds, Søren Linderoth, "*High-temperature Thermoelectric Properties of $Ca_{0.9}Y_{0.1}Mn_{1-x}Fe_xO_3$ ($0 \leq x \leq 0.25$)*", J. Mater. Sci. 48, 2817 (2013). [45].

4.1 Introduction

With increasing the global energy demand, thermoelectric materials have recently gained much interest in both the theoretical and technological aspects due to the potential use of these materials in converting waste heat into electricity [3,99]. In general, for a single thermoelectric material the conversion efficiency can be evaluated by the dimensionless figure-of-merit ($zT = \sigma S^2 T/\kappa$, where σ, S, T, κ are the electrical conductivity, the Seebeck coefficient, the absolute temperature, and the thermal conductivity, respectively). The requirements for practical application of high thermal-to-electrical energy conversion place on finding suitable thermoelectric materials, and are not easily satisfied. They should not only possess good thermoelectric performance, they must also be stable at high temperatures and be composed of nontoxic and low-cost elements, but also must be able to be processed and shaped cheaply. For this purpose, metal oxide-based materials are considered as good candidates.

$CaMnO_3$, which is a perovskite oxide with orthorhombic structure at room temperature, has also been considered as a promising thermoelectric *n*-type material for high-temperature application [88,100–105]. Many attempts have been made in order to improve the thermoelectric performance of this type of material, mainly to enhance the electrical conductivity, reduce further the thermal conductivity, while avoiding degradation of the Seebeck coefficient. Most of these studies have been focused on doping for example Yb at Ca-site [88,100–103] or Nb at Mn-site [88,104], while only few reports performed the research on dually doping e.g. Sr and Yb at Ca-site [105]. Previous reports have showed that the substitution of Y for Ca resulted in a significant improvement in the thermoelectric performance of $Ca_{1-x}Y_xMnO_3$ system in a wide temperature region, and the optimum doping level was found to be around $x = 0.1$ [101,106]. Similar to other multi-valence systems such as cobaltites [44] or titanates [107], the interrelation between Mn^{3+} and Mn^{4+} should be responsible for the transport mechanism in the $CaMnO_3$ material. Therefore, doping of trivalent ions such as Fe^{3+} or Co^{3+} at the Mn-site would probably influence the transport properties of this material.

In this chapter, we have prepared the $Ca_{0.9}Y_{0.1}Mn_{1-x}Fe_xO_3$ system with $0 \leq x \leq 0.25$, in which Ca-site was substituted with Y at a fixed concentration and Mn-site was partly replaced by Fe. The structural and the thermoelectric properties of these set of materials were investigated in detail. The influence of Y and Fe doping at Ca- and Mn-sites, respectively, on the crystal structure was carefully studied by the Rietveld refinement analysis. The correlation between the crystal structures and the thermoelectric properties are discussed.

4.2 Experimental

Polycrystalline samples of $Ca_{0.9}Y_{0.1}Mn_{1-x}Fe_xO_3$ with $x = 0$, 0.05, 0.15, 0.2, and 0.25 were synthesized by a solid-state reaction. A mixture of commercially available $CaCO_3$ (98 %), MnO_2 (99.9 %), Fe_2O_3 (99.9 %), and Y_2O_3 (99.9%) precursors were thoroughly mixed by ball milling with ethanol for 24 h. The mixtures were dried, and then calcined at 1273 K for 24 h in air with an intermediate grinding procedure. The densify processing was carried out using a spark plasma sintering (SPS) system (SPS Syntex Inc., Japan). The samples were heated to 1123 K, while a

uniaxial pressure of 50 MPa was applied for 8 min in Ar atmosphere. During the experiment, the temperature, applied pressure, and displacement of the sample were recorded continuously. The as-prepared samples were then polished in order to remove the graphite foil used during the SPS processing. The pellets were then cut into bar ($3.5 \times 3.5 \times 12$ mm^3) and plate ($10 \times 10 \times 1.4$ mm^3) shapes for the thermoelectric properties and thermal conductivity measurements, respectively. XRD analysis was carried out on the powders after calcining and after the SPS processing using a Bruker robot diffractometer with Cu Kα radiation. Structural refinement was carried out using the Rietveld method with TOPAS 4.1. Microstructures of the samples were observed using scanning electron microscopy (SEM) with a Hitachi TM-1000 system. The electrical resistivity and the Seebeck coefficient were measured simultaneously from room temperature to 1200 K using an ULVAC-RIKO ZEM3 measurement system in a low-pressure helium atmosphere. The thermal conductivity, κ, was determined from the measured thermal diffusivity, α, the heat capacity, C_p, and the density, d, using the formula: $\kappa = d \times \alpha \times C_p$. The densities of the samples were measured by an AccuPyc-1340 pycnometer. The thermal diffusivity was measured by a LFA-457 laser flash system.

4.3 Results and discussion

Figure 4.1 shows powder X-ray diffraction (XRD) spectra measured at room temperature for pure $CaMnO_3$ and for $Ca_{0.9}Y_{0.1}Mn_{1-x}Fe_xO_3$ samples with x = 0, 0.05, 0.1, 0.15, 0.2, and 0.25 after they were calcined at 1273 K for 24 h in air. All the visible XRD peaks can be indexed as the pure phase of $CaMnO_3$, indicating that all the investigated samples are single phase.

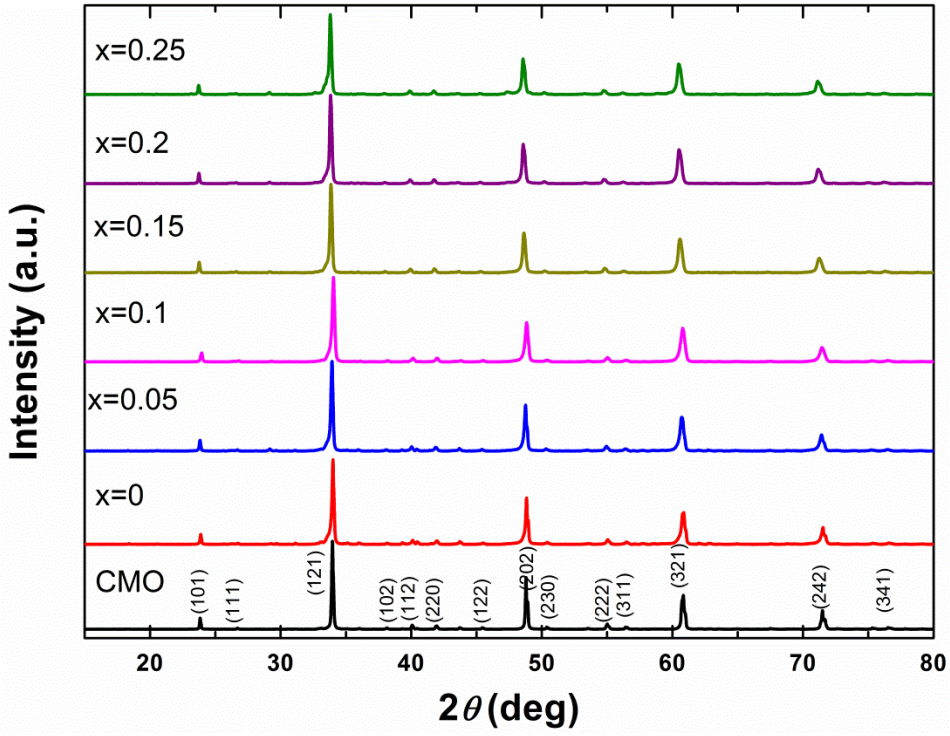

Figure 4.1 X-ray diffraction patterns of $CaMnO_3$ and $Ca_{0.9}Y_{0.1}Mn_{1-x}Fe_xO_3$ with x = 0, 0.05, 0.1, 0.15, 0.2, 0.25 samples after calcining at 1273 K for 24 h in air.

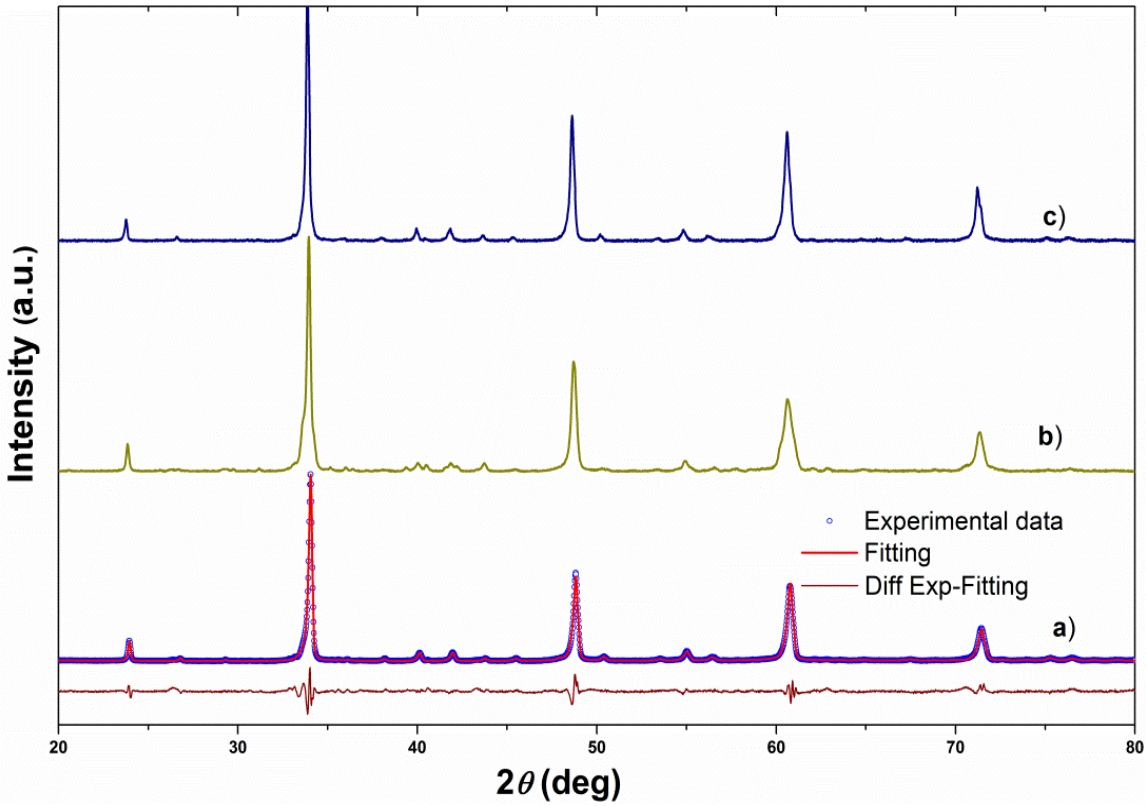

Figure 4.2 X-ray diffraction patterns of a typical sample $Ca_{0.9}Y_{0.1}Mn_{0.95}Fe_{0.05}O_3$: (a) Rietveld refinement profile of the calcined powder, (b) pellet sample sintered by SPS at 1173 K under pressure 50 MPa for 8 minutes under Ar atmosphere, (c) SPS sample after annealing at 1523 K in air for 24 h.

Figure 4.2 displays XRD patterns of a typical sample with $x = 0.05$ for the calcined powder (a), SPS sintered pellet (b), and the SPS sample after further heat treatment at 1523 K for 24 h in air (c). As indicated by this figure regardless of heat treatment, the structure remained the same. The structure refinement for the calcined powders $Ca_{0.9}Y_{0.1}Mn_{1-x}Fe_xO_3$ system was conducted using Topas 4.1 Rietveld refinement software with input parameters which were taken from Poeppelmeier et al. [108] using space group *Pnma* (No.62), and the refined results are summarized in Table 4.1. The profile *R* value (R_p), weighted profile *R*-factor (R_{wp}), and Goodness of fit (GOF) values obtained in this analysis are of high quality, and is clearly illustrated in Fig. 4.2 for a typical $Ca_{0.9}Y_{0.1}Mn_{1-x}Fe_xO_3$ sample with $x = 0.05$ as an example. This result implies that Y and Fe most likely substituted on the Ca- and Mn-sites of $CaMnO_3$, respectively. It can be judged from the data in Table 4.1, that the lattice parameters follow a relation of $c/\sqrt{2} \leq a \leq b$, confirming that the polycrystalline compounds $Ca_{0.9}Y_{0.1}Mn_{1-x}Fe_xO_3$ of our samples have O′-type orthorhombic structure [105,109].

The dependence of the lattice parameters and the cell volumes of $Ca_{0.9}Y_{0.1}Mn_{1-x}Fe_xO_3$ on the amount of Fe substituent are presented in Fig. 4.3. The result shows that the lattice parameters slightly increased with the increasing Fe concentration, resulting in an expansion in the unit cell volume. The increase in lattice parameters may be associated with the substitution of Fe^{3+} with a larger ionic radius (0.55 Å) for smaller Mn^{4+} (0.53 Å) ion [110].

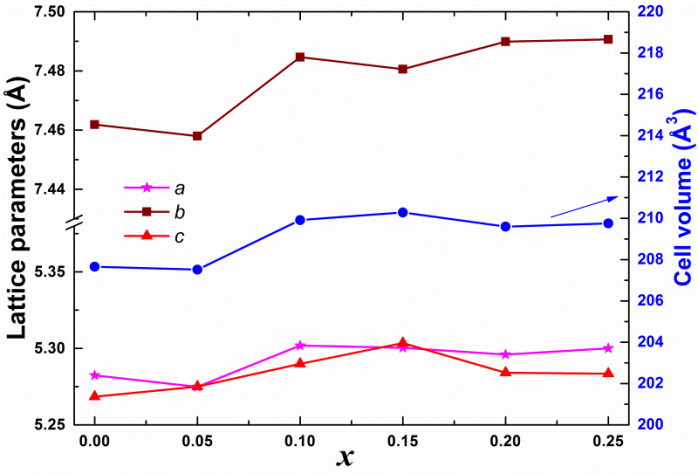

Figure 4.3 Lattice parameters and cell volume of $Ca_{0.9}Y_{0.1}Mn_{1-x}Fe_xO_3$ as function of Fe content (x).

In the case if Fe^{3+} substitutes for Mn^{3+} (0.58 Å), which has larger ionic radius, one would expect a slight contraction of the unit cell volume. The geometric distortion of ABO_3-type perovskites can be explained by Goldsmith tolerance factor, which is defined as

$$t = (r_A + r_O)/\sqrt{2}(r_B + r_O) \quad (4.1)$$

where r_A, r_B and r_O are the ionic radii of A, B, and O atoms, respectively [110]. For $Ca_{0.9}Y_{0.1}Mn_{1-x}Fe_xO_3$ compounds, calculation of Goldsmith tolerance factors (t) showed that the highest t value was 0.988 in the case of Fe^{3+} substitutes for Mn^{4+} and the smallest t value was 0.963 with Fe^{3+} substitutes for Mn^{3+}. It implies that the orthorhombic structure is stable for all $Ca_{0.9}Y_{0.1}Mn_{1-x}Fe_xO_3$ compounds.

Figure 4.4 depicts the temperature dependence of the electrical conductivity for $Ca_{0.9}Y_{0.1}Mn_{1-x}Fe_xO_3$ with x = 0, 0.05, 0.1, 0.15, 0.2, and 0.25 SPS sintered samples. The result points out that the electrical conductivity of the entire samples exhibit a semiconducting-like behavior over the whole measured temperature range. However, the electrical conductivity of the SPS sintered samples does

Table 4.1 Structural refinement factors, lattice parameters and cell volumes of $Ca_{0.9}Y_{0.1}Mn_{1-x}Fe_xO_3$.

Compositions (x)	0	0.05	0.1	0.15	0.2	0.25
R_{wp}(%)	8.42	9.33	9.39	11.27	10.62	10.62
R_p(%)	6.68	6.70	6.42	7.67	7.45	6.63
GOF	1.73	1.90	1.71	1.83	1.92	1.85
a (Å)	5.28233(2)	5.27480(3)	5.3018(3)	5.3004(1)	5.29596(2)	5.29999(3)
b (Å)	7.46185(3)	7.45797(4)	7.4846(6)	7.4806(2)	7.48990(3)	7.49067(5)
c (Å)	5.26841(2)	5.27498(5)	5.2899(2)	5.3035(3)	5.28405(2)	5.28344(3)
V (Å^3)	207.659(2)	207.514(2)	209.914(2)	210.284(3)	209.598(3)	209.755(2)

not show a clear tendency with the increase of Fe doping concentration. The value of σ tends to decrease with increasing Fe concentration for $x > 0.1$, while σ increases for the samples with $x \leq 0.1$. It should be noted here that those samples were sintered under a high pressure at high temperature, and in inert gas atmosphere. The oxygen content or even the microstructure may be varied from the samples, causing the different behaviors of the electrical conductivity as a result.

Temperature dependence of the Seebeck coefficient (S) for the SPS sintered samples of $Ca_{0.9}Y_{0.1}Mn_{1-x}Fe_xO_3$ with x = 0, 0.05, 0.1, 0.15, 0.2, and 0.25 are shown in Fig.4.5. S of all investigated samples show a negative values over the whole measured temperature range, indicating n-type conduction. Contrastingly to the electrical conductivity, the absolute S values increase with increasing Fe concentration, and the effect was more substantial in low temperature region.

In order to understand further the influence of the Fe doping on the thermoelectric properties, four SPS samples with x = 0, 0.05, 0.1, and 0.15 were selected and further annealed at 1523 K for 24 h in air. Figure 4.6a shows the electrical conductivity and the Seebeck coefficient as a function of temperature after annealing at 1523 K for 24 h in air. As seen from Fig. 4.6a a clear tendency showing the decrease of σ, while S increases with increasing Fe concentration from x = 0, 0.05, 0.1 to 0.15. The value of electrical conductivity was found to increase with more than two times as compared with post samples, while the Seebeck coefficient remained almost the same.

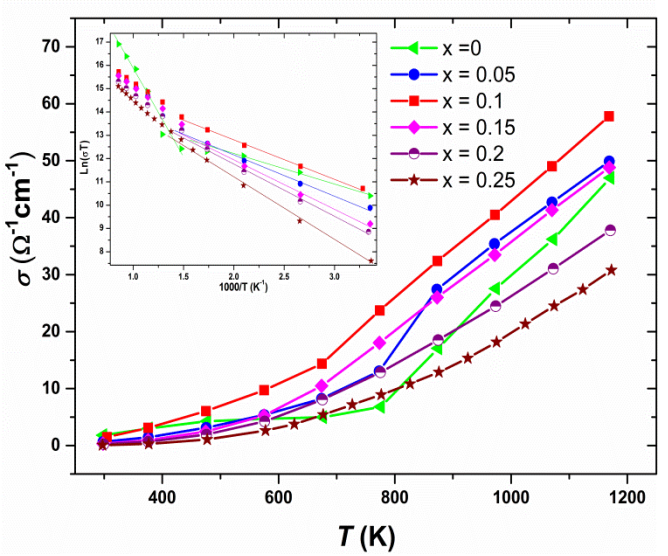

Figure 4.4 Temperature dependence of the electrical conductivity for $Ca_{0.9}Y_{0.1}Mn_{1-x}Fe_xO_3$ with x = 0, 0.05, 0.1, 0.15, 0.2, 0.25 SPS sintered samples; Inset, the activation energies were fitted from experimental data.

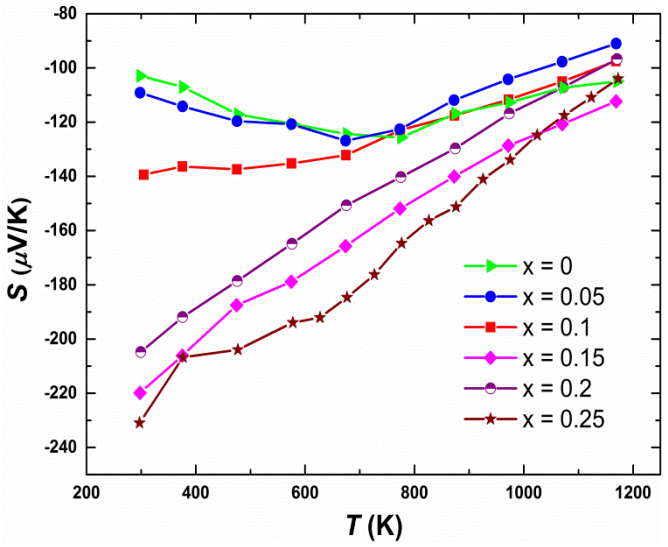

Figure 4.5 Temperature dependence of the Seebeck coefficient for $Ca_{0.9}Y_{0.1}Mn_{1-x}Fe_xO_3$ with x = 0, 0.05, 0.1, 0.15, 0.2, and 0.25 SPS sintered samples.

In general, the conduction mechanism of $CaMnO_3$ can be interpreted by hopping conduction [111] where hopping of the charge carriers is thermally activated with the activation energy E_a, the temperature dependence of the electrical conductivity σ is given as

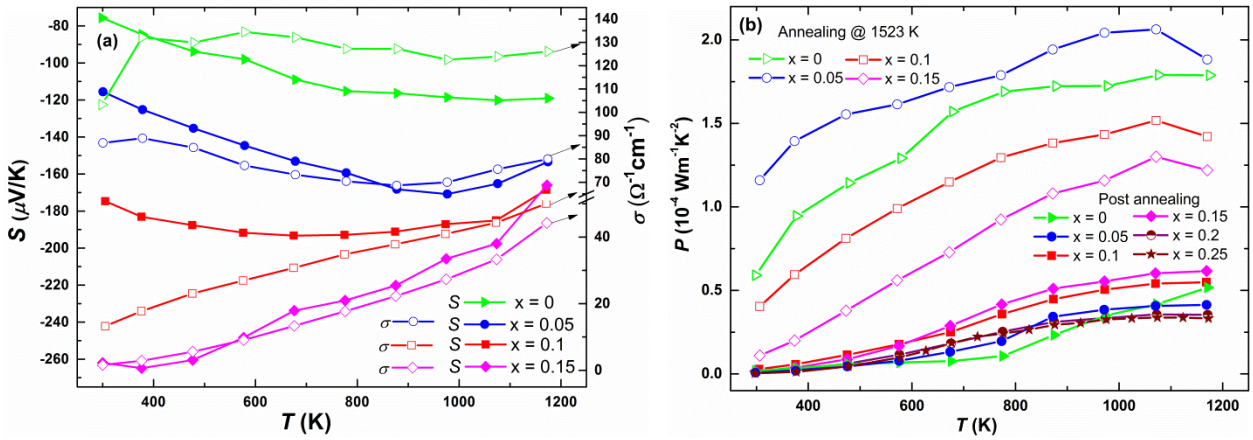

Figure 4.6 Temperature dependence of (a) the Seebeck coefficient (solid symbols) and the electrical conductivity (open symbols), and (b) the power factors for all the SPS sintered samples $Ca_{0.9}Y_{0.1}Mn_{1-x}Fe_xO_3$ with x = 0, 0.05, 0.1, 0.15, 0.2, 0.25 and selective samples with x = 0, 0.05, 0.1, 0.15 after annealing annealed at 1523 K for 24 h in air.

$$\sigma = C/T \exp(-E_a/k_B T) \quad (4.2)$$

where T is absolute temperature, k_B is the Boltzmann constant, and C is a constant depending on the charge carrier concentration. The activation energy could be estimated from the Arrhenius plot of $\mathrm{Ln}\sigma T$ versus $1/T$ as shown in the inset in Fig. 4.4.

The calculated activation energy, E_a is listed in Table 4.2 for all investigated samples, showing that E_a is linearly increasing with the increase of Fe substituent. However, the relationship between σ and E_a is only obeyed the hopping conduction's equation at temperatures below 700 K, as shown in Fig. 4.4 inset as well as in Table 4.2. As for the x = 0 and 0.05 samples, the $\mathrm{Ln}\sigma T$ versus $1/T$ curve showed two different slopes in the temperature regions of $T < 700$ and $T > 700$ yielding two activate energies (see Table 4.2), which is similar to the observation by Vecherskii et al. [112] on the oxygen non-stoichiometry $CaMnO_{3-\delta}$ system.

Table 4.2 Relative densities and electrical characteristics of $Ca_{0.9}Y_{0.1}Mn_{1-x}Fe_xO_3$.

Compositions (x)	0	0.05	0.1	0.15	0.2	0.25
Relative density (%)	94.36	94.86	97.40	96.65	95.60	93.39
E_a (meV)	117.46	146.15	155.28	181.33	189.69	227.47

For an extrinsic n-type semiconductor with negligible hole conduction, the thermoelectric power can be given by [18, 19]:

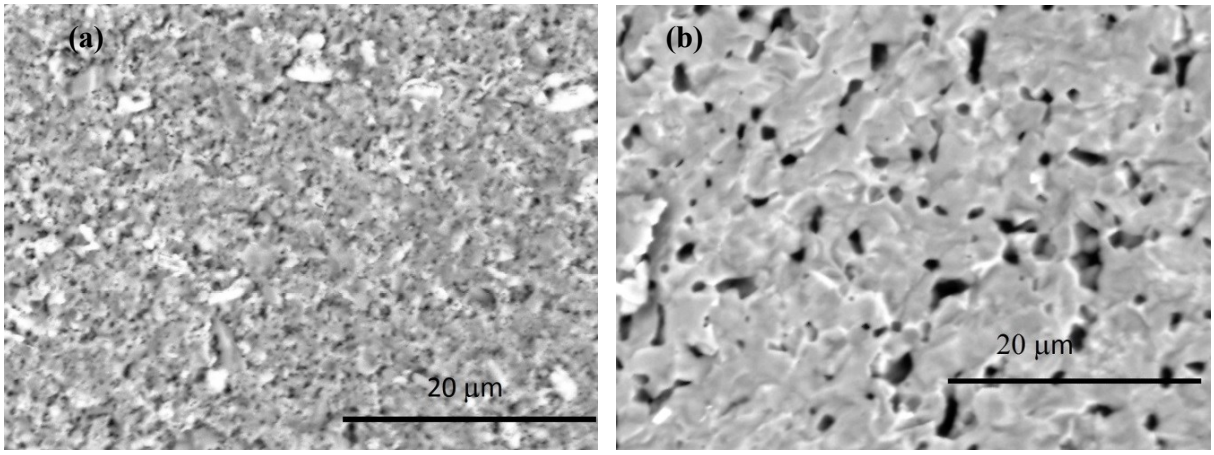

Figure 4.7 SEM images from fractured surfaces of a typical $Ca_{0.9}Y_{0.1}Mn_{1-x}Fe_xO_3$ with $x = 0.05$ sample: a) sample was sintered by SPS, b) sample was annealed at 1523 K for 24 h in air flow.

$$S(T) \approx -\frac{k_B}{e}\left[\ln\left(\frac{N_V}{n}\right) + A\right] \tag{4.3}$$

where e is the electric charge of the carrier, k_B the Boltzmann constant, N_V the density of states (DOS), n the carrier concentration, and A is a transport constant. Equations 4.2 and 4.3 clearly show that the decrease in carrier concentration (n) will result in an increase in the thermoelectric power (S) and vice versa. This can well explain the tendency of the Seebeck coefficient and the electrical conductivity as a function of temperature observed for the investigated samples after annealing with the increasing Fe concentration (see Fig. 4.6). Increasing the Fe content decreases the conductivity and increases the Seebeck coefficient which is also related to the carrier concentration via Eq. 4.3. However, further investigation on the carrier density and the mobility by means of the Hall measurements is currently ongoing to evidently support this interpretation.

Figure 4.6b shows the power factor (PF) as a function of temperature for all the SPS sintered samples and the selected ones after annealing. It is obvious that the PF values were remarkably improved by further heat treatment in air. The $x = 0.05$ sample showed the highest PF values over the whole measured temperature region, and the maximum PF attained was 2.1 x 10^{-4} W/mK^2 at about 1150 K.

To understand the reason which led to the finding interesting effect on the thermoelectric properties of the samples after heat treatment, the microstructure of the samples after SPS and after further annealing was studied using SEM, and the results are

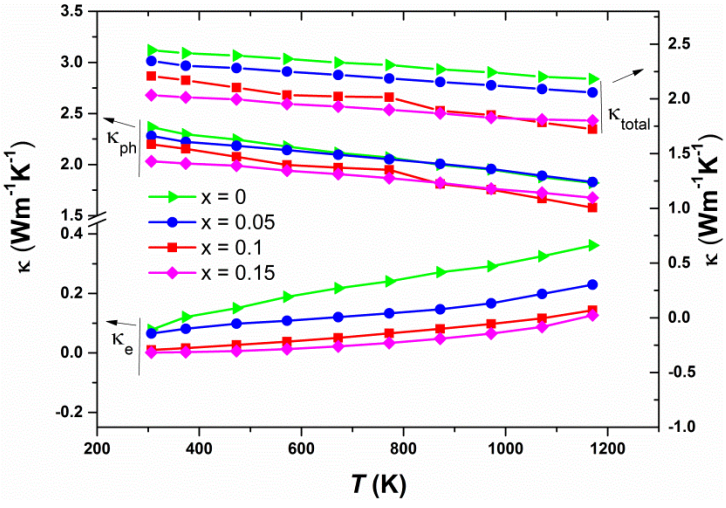

Figure 4.8 The total thermal conductivity (κ_{total}), the electronic and phonon components (κ_e and κ_{ph}) of $Ca_{0.9}Y_{0.1}Mn_{1-x}Fe_xO_3$ samples with $x = 0$, 0.05, 0.1, 0.15 as a function of temperature.

shown in Fig. 4.7a-b. Figure 4.7 shows an obvious difference in the grain size before and after the annealing. The small grains size structure observed for the SPS sintered sample means to be more grain boundaries, leading to the increase in electron scattering at the grain boundaries, and thus decreasing the electrical conductivity. This result well explained the behavior of the electrical conductivity for the samples before and after heat treatment.

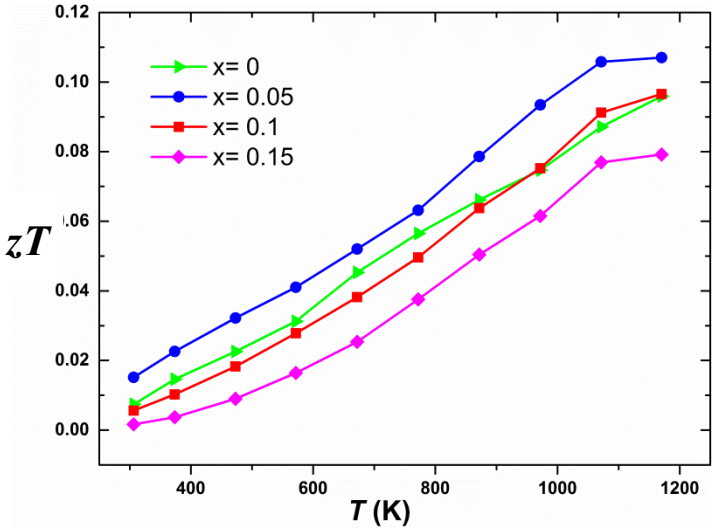

Figure 4.9 The dimensionless figure-of-merit (zT) as a function of temperature for $Ca_{0.9}Y_{0.1}Mn_{1-x}Fe_xO_3$ with x = 0, 0.05, 0.1, 0.15 selective SPS samples after heated treatment at 1523 K for 24 h in air.

Figure 4.8 shows the total thermal conductivity (κ_{total}) for all investigated samples. It can be seen that κ decreases with increasing temperature. The substitution of Fe at Mn-sites generally decreases the thermal conductivity. The total thermal conductivity can be expressed by the sum of a lattice component (κ_{ph}) and an electronic component (κ_e), i.e., as $\kappa_{total} = \kappa_{ph} + \kappa_e$. In this case, the contribution of κ_e to κ_{total}, estimated from the Wiedemann–Franz relation, is small, indicating the major contribution of the phonon term κ_{ph}, as clearly illustrated in Fig. 4.8. Finally, using the measured thermoelectric data, the dimensionless figure-of-merit of these compositions was calculated. Figure 4.9 presents the dimensionless figure-of-merit, zT, versus temperature for the x = 0, 0.05, 0.1 and 0.15 samples, showing that zT increased for the x = 0.05 and then decreased again with increasing x over the whole temperature range. The maximum zT value reached a value of 0.11 at about 1150 K for the x = 0.05 samples.

4.4 Conclusion

The effect of Fe substitution on the structure and the high-temperature thermoelectric properties of $Ca_{0.9}Y_{0.1}Mn_{1-x}Fe_xO_3$ (x = 0, 0.05, 0.1, 0.15, 0.2, 0.25) was investigated in details. Structural analysis shows that lattice parameters slightly increase with increasing amount of Fe substituent, which originates from the difference in the ionic radii between Fe and Mn ions. The thermoelectric properties were found to be improved for the Fe-doped samples with $x < 0.1$, particularly for the SPS samples with further annealing mainly due to the increase in the Seebeck coefficient that could overcome the simultaneous decrease of the electrical conductivity. The thermal conductivity was suppressed by the substitution of Fe for Mn. The maximum PF attained was 2.1 x 10^{-4} W/mK^2 for the x = 0.05 sample at 1150 K giving a maximum zT = 0.11, which is about 20 % higher than the x = 0 sample. Further study should be performed with finer Fe substituent tuning with $x < 0.1$ in order to optimize these compounds high-temperature thermoelectric properties.

Chapter 5 Segmented thermoelectric oxide-based module

Abstract

To improve the thermoelectric (TE) power generation performance of an oxide-based module, a segmentation of the legs is implemented. A high-performance segmented oxide-based TE module using segmentation of the half-Heusler $Ti_{0.3}Zr_{0.35}Hf_{0.35}CoSb_{0.8}Sn_{0.2}$ and the misfit-layered cobaltate $Ca_3Co_4O_{9+\delta}$ as the *p*-leg and 2% Al-doped ZnO as the *n*-leg was for the first time fabricated and characterized. The TE properties of individual legs as well as the interfacial contact resistances as a function of temperature were investigated. Numerical modeling was used to predict the efficiency and to evaluate the influence of the electrical and thermal losses on the performance of TE modules. The maximum output power of a 4-couples segmented module at a temperature difference of about 700 K attained 829 mW corresponding to a power density of ~650 mW/cm^2, which is three times higher than that of the best reported non-segmented oxide module under the same condition. Initial long-term stability test of the module at hot and cold side temperatures of 1073/444 K showed a promising result although a slightly degradation tendency could be observed after 48 h operating in air.

The work presented in this chapter is submitted to Energy 2014: Le Thanh Hung, Ngo Van Nong, Gerald Jeffrey Snyder, Benjamin Balke, Li Han, Rasmus Bjørk, Pham Hoang Ngan, Tim C. Holgate, Søren Linderoth, and Nini Pryds, "*Segmented thermoelectric oxide-based module*". Under review

5.1 Introduction

Thermoelectric (TE) energy conversion, which directly generates electricity from waste heat, has been considered to play an important role in a global sustainable energy solution [3,52]. In a such energy conversion device, the maximum energy conversion efficiency η_{max}, can be expressed as

$$\eta_{max} = \frac{T_h - T_c}{T_h} \frac{\sqrt{1+z\overline{T}}-1}{\sqrt{1+z\overline{T}}+\frac{T_c}{T_h}} \quad (5.1)$$

where T_h is the hot side temperature and T_c is the cold side temperature, $\frac{T_h - T_c}{T_h}$ is known as the Carnot efficiency, $\overline{T} = \frac{T_h + T_c}{2}$, z (= $\alpha^2/(\rho.\kappa)$, where α, ρ, and κ are the Seebeck coefficient, the electrical resistivity, and the thermal conductivity, respectively) is the dimensionless TE figure-of-merit and T is absolute temperature. It is obvious from equation (5.1) that as the temperature span increases both the TE conversion and Carnot's thermodynamic efficiencies of a thermoelectric generator (TEG) can be significantly improved [99]. Under a large temperature gradient in air, oxide-based thermoelectric materials are one of the strongest candidates due to their good thermal and chemical stabilities compared to TEGs made of conventional alloys, such as PbTe, complex Zintl compounds, etc. In addition, TEGs made of oxides are cost-effective due to the fact that the materials are cheap and easily processed. Among TE oxides, the layered-cobaltite $Ca_3Co_4O_{9+\delta}$ (Ca349) and doped ZnO materials are of the best candidates for high temperature applications [44,65,115]. Although a considerable number of oxide-based TE modules have been fabricated and tested [54] the output power generation of oxide modules are still limited due to the drawback of low performance of oxide materials in particular in mid-to-low temperature range [11,54]. In medium temperature range, half-Heusler compounds have recently emerged as good materials. The peak zT of a *p*-type half-Heusler material e.g. $Hf_{0.8}Ti_{0.2}CoSb_{0.8}Sn_{0.2}$ [75] can reach a value of 1 at 1073 K, which makes these materials promising candidates for waste heat recovery for the transportation sector [75,116]. Nevertheless, TE modules constructed from these materials are unstable at high temperatures (usually ≥ 773 K) [93] due to sublimation and oxidation. Therefore, segmentation of a half-Heusler alloy with an oxide TE material (at the hot side) may either improve the overall conversion efficiency of an oxides-based TEG or prevent the half-Heusler from sublimation/oxidation at high temperatures.

In this work, with the aim to improve the conversion efficiency of high temperature oxides-based TEG, a p-type half-Heusler $Ti_{0.3}Zr_{0.35}Hf_{0.35}CoSb_{0.8}Sn_{0.2}$ (HH) alloy was selected to be segmented with the Ca349 oxide. A one-dimensional (1D) model [117] was first used to design and predict the conversion efficiencies of TEGs with various segmented leg designs. Based on these results, a 4 *p*-*n* couples segmented thermoelectric generator (STEG) using the segmentation of HH/Ca349 as the p-leg and 2% Al-doped ZnO as the n-leg was constructed. A non-segmented thermoelectric generator (NTEG) using *n*-type 2% Al-doped ZnO and *p*-type Ca349 was also used for comparison. The power generation characteristics of the NTEG and the STEG were then characterized under various temperature gradients in air with the hot side temperatures varying up to 1173 K. The interfacial contact resistances and TE properties of the legs were investigated as a function of temperature and the results of these analyses were fed into a 3D model. Using the 3D model [118], a comparison between the experimental results and the model were carried out taking into account the contact

resistances as well as other parasitic losses. In addition, a preliminary long-term test was also performed on the STEG at high temperature to investigate the stability of the module.

5.2 Modeling

5.2.1 Formulation of the model

With the purpose of evaluating the efficiency of non-segmented and segmented TE elements, both the 1D [26,117] and the three-dimensional 3D [118] numerical models are used. These models take into account all thermoelectric effects i.e. the Peltier, Seebeck and Thomson effects, as well as heat conduction, Joule heating and the temperature dependence of the resistivity ρ(T), thermal conductivity κ(T), Seebeck coefficient α(T), and compatibility factor $s = \frac{\sqrt{1+zT}-1}{\alpha T}$. To have a guideline on the materials selection and TEG design, the efficiencies of segmented and non-segmented TE elements were first calculated under the ideal conditions, i.e. neglecting all the heat losses, thermal and electrical contact resistances. The calculations can therefore be considered as an upper limit for the obtainable actual efficiency in experiments. As for a practical TEG, the performance strongly depends on the thermal and electrical losses. Therefore, the 3D numerical model is used to evaluate the module's characteristics under realistic conditions including losses. Besides using the 3D numerical model, 1D modeling was used to confirm the design of the module geometries.

The 1D model solves for the reduced current density u (= $J/\kappa\nabla$T), which is defined as the ratio between the electrical current density (J) and the heat flux by conduction. When u is defined at a single point – e.g. at the hot side, u ($T = T_h$) – the value of u at any temperature along the leg can be determined using the following the differential equation

$$\frac{du}{dT} = u^2 T \frac{d\alpha}{dT} + u^3 \rho\kappa, \tag{5.2}$$

with an approximate recursive solution given elsewhere [99,119]. The differential equation is valid for both non-segmented and segmented legs if – for the latter – the material properties are changed from one material to another at a certain interface temperature (T_m) where the segments meet. From the reduced current densities evaluated at the cold and hot side temperatures, $u_c = u$ ($T = T_c$) and $u_h = u$ ($T=T_h$), the efficiency of a segmented or non-segmented leg can be found:

$$\eta_{leg} = 1 - \frac{\alpha_c T_c + \frac{1}{u_c}}{\alpha_h T_h + \frac{1}{u_h}} \tag{5.3}$$

As for the segmented legs, η_{leg} is determined by an optimum interface temperature T_m. To simplify the issue, T_m is often sets to be the temperature where the material at the cold side reaches its maximum zT.

For a typical *n*-*p* unicouple, the electric current through both elements is the same, but the relative contribution to the total heat flux is regulated by having different cross-sectional areas A_p and A_n (with A_p and A_n being the cross-sectional areas of *p*- and *n*-type legs, respectively). The maximum efficiency condition therefore requires a specific ratio of A_p/A_n to optimize the electric current of the unicouple. Assuming the *n*-element and the *p*-element have the same total length ($l = l_p = l_n$), the

ratio of the cross-sectional areas can be calculated by equating the total electric current ($I = J_pA_p = -J_nA_n$):

$$\frac{A_p}{A_n} = \frac{-J_n}{J_p} = \frac{-\int_{T_c}^{T_h} u_n \kappa_n dT}{\int_{T_c}^{T_h} u_p \kappa_p dT} \quad (5.4)$$

The electric current can be solved in term of the total area ($A_{total} = A_p + A_n$):

$$I = \frac{A_{total}}{l} \times \frac{-\int_{T_c}^{T_h} u_n \kappa_n dT \times \int_{T_c}^{T_h} u_p \kappa_p dT}{\int_{T_c}^{T_h} u_p \kappa_p dT - \int_{T_c}^{T_h} u_n \kappa_n dT} \quad (5.5)$$

The total voltage produced by a *p*-*n* unicouple can be computed by

$$V = \frac{1}{u_{h,p}} + \alpha_{h,p} T_h - \frac{1}{u_{c,p}} - \alpha_{c,p} T_c + \frac{1}{u_{h,n}} + \alpha_{h,n} T_h - \frac{1}{u_{c,n}} - \alpha_{c,n} T_c \quad (5.6)$$

The total electric power generation can then be determined by the relationship, $W = IV$. The total heat flowing through the *p* and *n* legs can be expressed as

$$U_{total} = I(\alpha_p T + \frac{1}{u_p} - \alpha_n T - \frac{1}{u_n}) \quad (5.7)$$

Finally, the thermal-to-electric energy conversion efficiency can be obtained:

$$\eta = \frac{W}{U_{total}} \quad (5.8)$$

As for the 3D modeling, the software COMSOL Multiphysics was used to solve the full thermoelectric equations on the specified geometry which includes *p*- and *n*-type legs, electrodes and substrates. The coupled differential equations describe the electrical current density, $\boldsymbol{J}$, and the heat flux, $\boldsymbol{J}_Q$, as

$$-\boldsymbol{J} = \sigma \nabla V + \sigma \alpha \nabla T \quad (5.9)$$

$$\boldsymbol{J}_Q = -\kappa \nabla T + T \alpha \boldsymbol{J} \quad (5.10)$$

In the equation (5.9) for $\boldsymbol{J}$, the first term is Ohms law, while the second describes the Seebeck effect. In the equation (5.10) for $\boldsymbol{J}_Q$, the first term describes Fourier heat conduction, while the latter describes the Peltier effect. Both Joule heating and the Thomson effect are included in the model. The heat losses by conduction, convection and surface to surface radiation can also be included in the model as well as contact resistances [118].

5.2.2 Calculation results

From the measured data of $\rho(T)$, $\kappa(T)$, and $\alpha(T)$, the efficiencies of non and segmented legs/TEGs can be calculated using the theoretical models described above. The materials for segmentation are selected based on figure of merit (zT) and compatibility factors (s). Fig. 5.1 shows the calculated results of zT, s, and absolute efficiency of non-segmented *p*-type HH, Ca349 and segmented HH/Ca349 materials. The zT value was determined to be ~0.2 for the *p*-type Ca349 at 1100 K and ~0.65 for the $Ti_{0.3}Zr_{0.35}Hf_{0.35}CoSb_{0.8}Sn_{0.2}$ (HH) at a temperature of 750 K as showed in Fig. 5.1a. The results of *p*-type materials prepared in this study are comparable with previous works reported for misfit-layered cobaltate $Ca_3Co_4O_{9+\delta}$ [44,115] and half-Heusler [75]. It can be seen from Fig. 5.1a that the zT of Ca349 has low value in the low-medium temperature regions, where HH alloy exhibits good zT. Therefore, the segmentation of Ca349 and HH is expected to exhibit high performance in wide temperature range. In addition, an advantage of using oxide Ca349 at the hot side is that it can help to protect the HH from oxidation and sublimation at high temperatures and possibly no

encapsulation is necessary for modules based on segmented HH/Ca349. However, in order to achieve higher thermal to electrical energy conversion efficiency the compatibility factor, *s*, of these materials has to be first considered [26,35,70]. From Fig. 5.1a, one can see that the compatibility factors of both HH and Ca349 slightly increased with increasing temperature, and they are within a factor of two. This implies that the segmented HH/Ca349 leg should provide a higher performance at a larger working temperature span [25]. Accordingly, the maximum conversion efficiency of the segmented HH/Ca349 leg could attain a value of about 7.1%, which is about 2.5 times higher than the single material Ca349 (2.9%) - under the same hot side and cold side temperatures of 1173/300 K (as showed in Fig. 5.1b). The maximum efficiency of single HH can attain a value of 6.4% at the hot and cold side temperatures of 773/300 K. The results point out that the main contribution to the increasing performance of segmented HH/Ca349 leg is attributed to the high performace of HH in the low-mid temperature range. Consequently, a TEG comprising of segmented HH/Ca349 legs is expected to achieve higher power generation in comparision with the one using non-segmented legs.

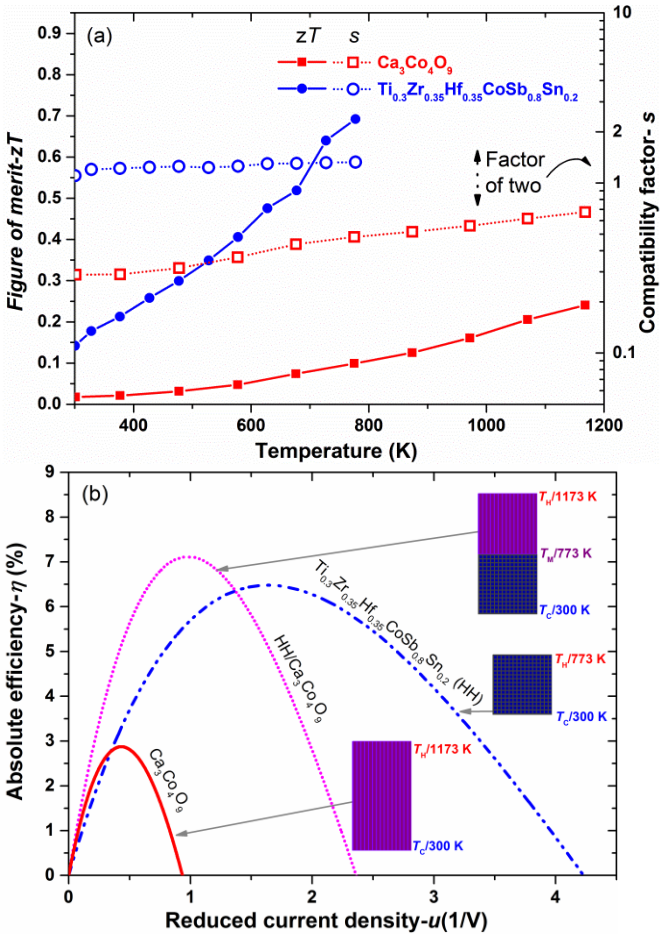

Figure 5.1 (a)Temperature dependences of *zT* and *s* of *p*-type Ca349 and HH alloys. (b) Absolute efficiencies of *p*-type Ca349, HH and segmented HH/Ca349.

For many applications e.g. power generation from waste heat, finding the optimized thermoelectric generation efficiency from given TE materials is a crucial step which affects extrinsic properties such as geometry of *p*-*n* legs [120]. Fig. 5.2 displays the maximum efficiency of 4 *p*-*n* couples of STEG and NTEG modules as a function of A_p/A_n ratio with fixed $T_c = 300$ K, $T_h = 1173$ K and 8 mm in length. In this calculation, we have assumed that the *n*-element and *p*-element have the same length and A_p is varied while A_n is fixed at 0.16 cm^2, and contact resistances are neglected. As seen in Fig. 5.1c, the maximum efficiency of STEG increases sharply with increasing the A_p/A_n ratio reaching a maximum 2.7% at $A_p/A_n = 2.4$ and then decreases slowly above this value. As for the NTEG, the maximum efficiency attains 1.6% at $A_p/A_n = 3.5$. These results suggest that the STEG would be able to perform a maximum efficiency, which is ~170% higher than the NTEG at their respective optimized A_p/A_n ratio. As seen from Fig. 5.2, a good agreement was obtained between the 1D and the 3D modeling. When combining with *n*-legs of $Zn_{0.98}Al_{0.02}O$, both the STEG and NTEG have an efficiency of less than 3%. This is due to the fact that an *n*-$Zn_{0.98}Al_{0.02}O$ leg could produce a

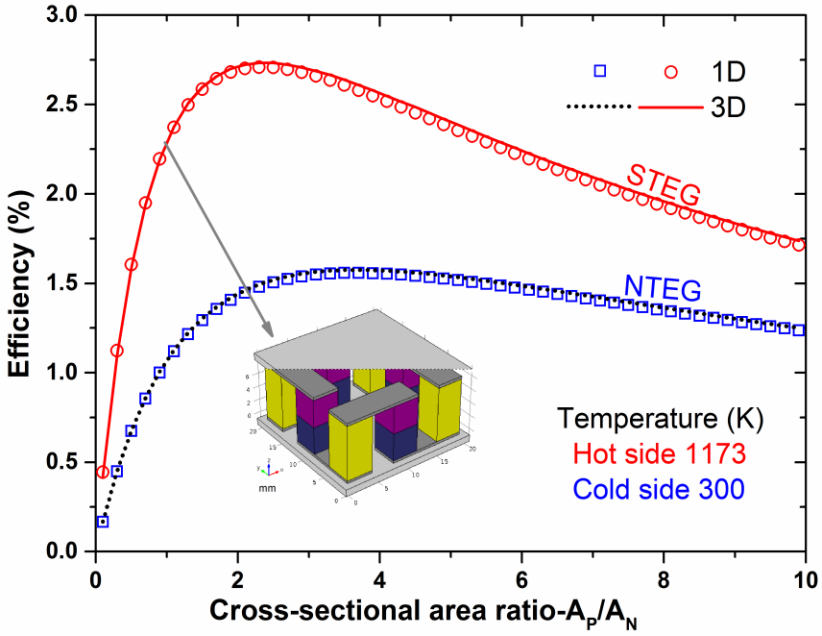

Figure 5.2 1D and 3D calculated efficiency as a function of the cross-sectional area ratio A_p/A_n at T_h/T_c = 1173/300 K for 4 couples of NTEG and STEG with $Zn_{0.98}Al_{0.02}O$ as n-legs.

maximum efficiency of only 0.7% under the hot and cold side temperatures of 1173/300 K. At the ratio of A_p/A_n = 1, the efficiency of STEG attains 2.3%, which is about 85% of the maximum value (~2.7%) at the optimum A_p/A_n = 2.4. However, the total volume of TE legs with A_p/A_n = 1 (1.024 cm^3) is only 59% of the total volume of TE legs with A_p/A_n = 2.4 (1.74 cm^3), suggesting that the capital cost might reduce due to the less amount of materials required. Therefore, we have chosen the ratio of A_p/A_n = 1 to build up and characterize the 4 *p*-HH/Ca349, *n*-$Zn_{0.98}Al_{0.02}O$ couples modules.

5.3 Experimental procedures

5.3.1 Thermoelectric materials

2%Al-doped ZnO platelets were synthesized using the nanoparticles as a seed by hydrothermal method at 368 K for 24 h in a solution of 0.49 M $Zn(CH_3COO)_2 \cdot H_2O$, 0.01 M $Al(NO_3)_3$, (Zn/Al = 98:2), 0.1 M NaOH, and 0.17 mM sodium citrate [18]. After hydrothermal process, the formed precipitates were centrifugally washed several times with de-ionized water and ethanol, and then dried in vacuum. Spark plasma sintering (SPS) system of Dr Sinter 515S (Syntex Inc., Japan) was used to consolidate the samples under the following conditions: constant uniaxial pressure of 50 MPa; holding temperature of 1223 K; holding time of 8 min, Ar atmosphere, and a ramping rate of 130 K/min. The details of this work could be seen elsewhere [61].

The *p*-type $Ca_3Co_4O_9$ were prepared by the solid state reaction followed by a spark plasma sintering process. Powders of $CaCO_3$ (99.99%) and Co_3O_4 (99.7%) were mixed, ball milled for 48 h in ethanol. The mixture was then dried and calcined in air at 1173 K for 24 hours. The obtained

calcined powders were then pressed into pellets using SPS with optimized sintering conditions under a uniaxial pressure of 50 MPa at 1123 K for 5 min in vacuum.

HH compound samples with the stoichiometric composition of $Ti_{0.3}Zr_{0.35}Hf_{0.35}CoSb_{0.8}Sn_{0.2}$ were prepared by arc melting from the pure (99.999%) metals Ti, Zr, Hf, Co, Sb, and Sn under argon atmosphere. In the course of the arc melting, the samples were re-melted and turned over three times to ensure the homogeneity. The obtained ingots were milled in a high-energy ball milling station (PM-100; Retsch, Germany) for 5 h under a protective argon atmosphere. The powder was filtered through a 60-mesh sieve and then sintered using SPS at 1373 K for 20 min (heating/cooling rates of 50 K/min) under a pressure of 50 MPa.

Pellets of *p*- and *n*-type materials $Ca_3Co_4O_9$, HH and 2% Al-doped ZnO were cut into bars of $4\times4\times8$ mm^3, which were then characterized for their thermoelectric properties and used as legs for building modules.

5.3.2 Segmentation

To make segmentation, the obtained pellets of Ca349 and HH were cut, polished and then cleaned with acetone, isopropyl alcohol and deionized water and finally dried with nitrogen. As designed module can work at hot side temperature up to 1223 K with optimum interface temperature T_m = 773 K and cold side temperature 300 K, the length of Ca349 and HH was calculated to be 4 mm for each with the negligible interface thermal resistance assumption. 150 μm thick Ag foil with a purity of 99.99% was used as the standard joining material between the HH and the Ca349 while 400 μm thick Ag foil was used to make electrodes which coupled the *n* and the *p*-type materials. The brazing process was conducted in vacuum using a SPS under 20 MPa at 973 K for 10 min. The TE properties of both the p- and n-legs were also characterized after making the contacts, and the result (not shown here) confirmed that there is no significant change during the joining process.

5.3.3 Module fabrication

For TE modules fabrication, the Ag electrodes was first fabricated on top of two alumina substrates with the dimension of $21\times21\times1$ mm^3 by hot-pressing at 1073 K for 2 h in air. The $21\times21\times1$ mm^3 substrate was chosen to fit the size of the graphite die used in a SPS process. A set of 4segmented *p*-legs and 4 non-segmented *n*-legs was attached onto these designed substrates according to the configuration shown in Fig. 5.1c. The whole module was then placed in a graphite die and hot-pressed at 973 K under a pressure of about 20 MPa in Ar atmosphere.

5.3.4 Characterization

Before and after sintering, the samples were examined by X-ray diffraction (XRD) on a Bruker D8 diffractometer (Bruker, Germany) using Cu-Kα radiation. The measurements of the electrical resistivity and the Seebeck coefficient were carried out on an ULVAC-RIKO ZEM-3 from room temperature up to 1200 K under a low-pressure helium atmosphere. The thermal conductivity (κ) was determined from the thermal diffusivity (γ), the mass density (ρ) and the specific heat capacity (C_p)

according to the equation $\kappa = \gamma\rho C_p$. The thermal diffusivity was obtained by the laser flash method (Netzsch LFA-457, Germany), the mass densities of the samples were measured by Archimedes' method using water with surfactant, and the specific heat capacity was measured using a differential scanning calorimeter (Netzsch DSC 404C, Germany).

Figure 5.3a presents a schematic configuration used to determine the interfacial contact resistance R_c by linear extrapolation of the resistance (R) vs. the distance of measuring probes ($V_{0\text{-}1}$ to $V_{0\text{-}4}$) and subsequent subtraction of the contribution from the alloy ($V_{II\text{-}0}$, $V_{I\text{-}0}$) between the probe lead and the interface. The contact resistance is actually the interface resistance, which is multiplied by the cross-sectional area of the interface to give the area specific resistance of the interface (ASR). The experiments were conducted in steady gas flow from 300 K to 850 K for the n-type leg of doped ZnO/Ag and from 300 K to 1070 K for p-type leg of Ca349/Ag. Fig. 5.3b demonstrates the method for measuring the contact resistance between the different TE materials in a segmented leg using the

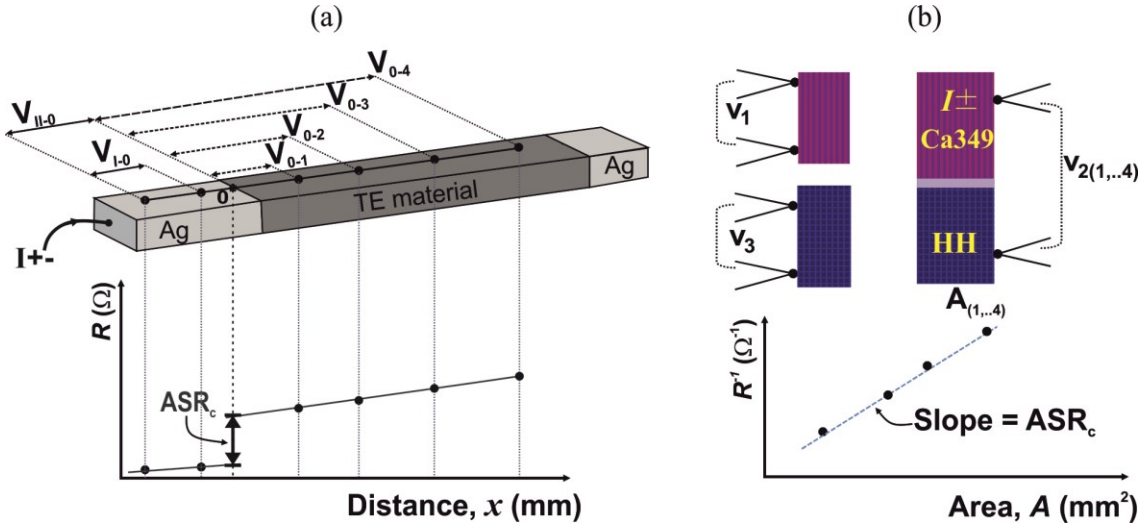

Figure 5.3 Configurations of the electrical contact resistance measurement for the non-segmented leg (a) and the segmented leg (b).

ZEM-03. The contact resistance can be determined by measuring the electrical resistivity of individual Ca349 (V_1) and HH (V_3) materials and the resistance across the interface of the segmented HH/Ca349 materials (V_2). By measuring the resistances of the segmented sample [$V_{2(1,..4)}$] with various cross-sectional areas $A_{(1,..4)}$, the ASR is then calculated from the slope of the fitted R^{-1}/A curve using the least-squares method.

Microstructure of the contacts and joining part were observed by a scanning electron microscopy (SEM) TM3000.

The power generation characteristics of STEG and NTEG were performed in air using an in-house Rig-test system. The I-V curves at different temperature gradients were automatically measured by sweeping the load resistance using an electronic load system. The designed measurement system is allowed to setup the measuring current range from 0 to 15 A with the minimum 1 mA step size, while the electronic load and shunt resistance are then applied and scanned until reaching a value closest the defined current together with measured voltage of TEG. The controlled software system

was designed based on the Apache web server software (Open Source Software, OSS) which is able to have maximum flexible setting up of required measurements such as gas control, cycling and long-term stability tests etc. In order to define the accurate temperature gradient, three 0.5 mm N-type thermocouples were attached on the Ag electrodes at the hot side and the cold side of module. The thermocouple at the hot side is also used as the process variable for the PID of the heater controller.

The conditions of the measurement and their uncertainties are summarized in Table 1. The values of uncertainty are calculated in term of the mean value divided by standard deviation. For the maximum output power uncertainty is estimated from the uncertainties of the electric current and voltage [121].

Table 5.1 The experimental measurement conditions and uncertainty.

Experiments			Measurement conditions	Uncertainty (%)
TE properties	Seebeck (α)		Helium atmosphere	3-5
	Res. (ρ)		Helium atmosphere	2-5
	Thermal cond. (κ)		Vacuum	< 5
Contact resistance (R_C)*	Leg-electrode		Air	1-3
	Seg. leg HH/Ca349		Helium atmosphere	2-5
Module NTEG & STEG	Temp.	T_c (< 450 K)	Air	4.7
		T_h	Air	2.3
	Current (I) @ P_{max}		Air	0.2
	Voltage V_{OC}		Air	0.1
	V @ P_{max}		Air	1.2
	P_{max}		Air	1.21

*The values excluded the geometric uncertainty.

5.4 Results and discussion

5.4.1 TE properties of the materials

Figure 5.4 shows the thermoelectric properties of a single *p*-type leg of HH and Ca349 as a function of temperature. For both *p*-type materials, the Seebeck coefficient (α) increased with increasing temperature (Fig. 5.4a). The α values of Ca349 were measured to be about 150 μV/K at room temperature and 180 μV/K at 1100 K. As for the HH alloys, α values increased from 160 to 230 μV/K as temperature increasing from room temperature to 700 K. The power factor ($=\alpha^2/\rho$) of HH is about an order higher than that of Ca349. The thermoelectric properties of *n*-type 2% Al-doped ZnO, the absolute Seebeck coefficient of *n*-type increased from about 40 μV/K at room temperature to about 170 μV/K at 1150 K. The power factor of the *n*-type materials increased with increasing temperature and reached a maximum value of about 11×10^{-4} W/mK^2 at 1150 K (Fig. 5.4b). The total thermal conductivity (not shown here) decreased with increasing temperature, and

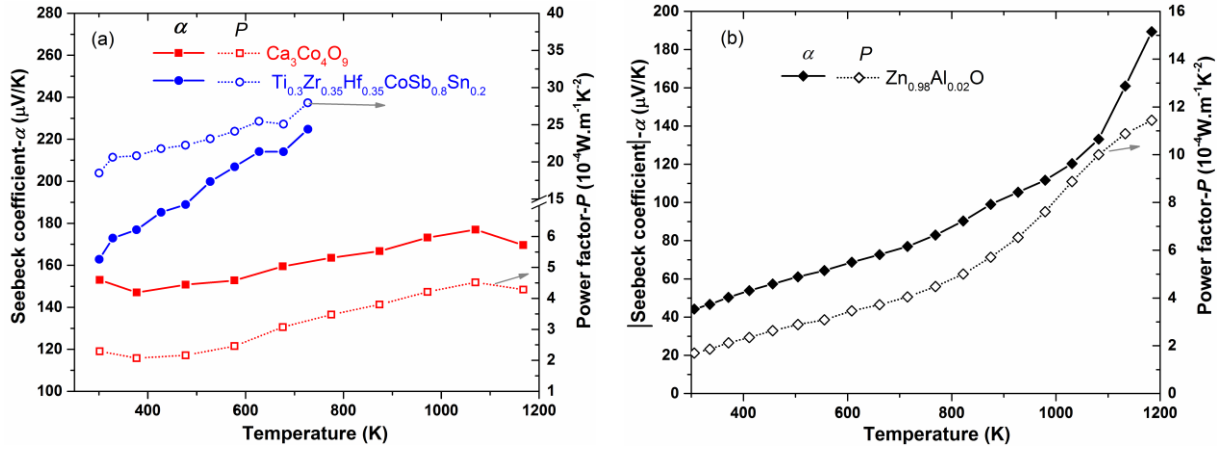

Figure 5.4 Temperature dependence of the Seebeck coefficient and power factor of (a) *p*-type Ca349 and $Ti_{0.3}Zr_{0.35}Hf_{0.35}CoSb_{0.8}Sn_{0.2}$ and (b) *n*-type 2% Al-doped ZnO.

the κ values was 23 and 5 W/mK at room temperature and 1150 K, respectively. The calculated z*T* were determined to be ~0.25 at about 1150 K. Thermoelectric properties of TE *p* and *n*-type in this work are reproducible and in good agreement with the other reported values of the same compositions [11,122].

5.4.2 Interfacial Contacts

In thermoelectric power generation devices, interfacial contact resistances are directly added to the TE module's internal resistance, thus it strongly decreases the electric current, *I,* and the output power, *P* [30,123,124]. Therefore, the effect of contact resistance on output power cannot be neglected and must be taken into account. In this study, the interfacial contact resistance between Ag/Ca349, $Ag/Zn_{0.98}Al_{0.02}O$ and HH/Ag/Ca349 have been characterized as a function of temperature, the obtained results are presented in Figure .5a-c. Fig. 5.5a-b plots the temperature dependence of

contact resistance between Ag electrodes with *p*-Ca349 and *n*-$Zn_{0.98}Al_{0.02}O$. The interfacial microstructure is shown through SEM images in the inset-figures. It can be seen that the Ag electrodes and the oxide materials have good adhesion at the interface. SEM and EDS analyses revealed that there are no obvious diffusion and secondary phase observed in the vicinity of those connections. Consequently, the obtained contact resistance values were found to be around 400 $\mu\Omega cm^2$, which are lower than the electrode using Fe22Cr [125]. Fig. 5.5c illustrates the contact resistance of segmented HH/Ag/Ca349. The contact resistance tends to decrease from 170 $\mu\Omega cm^2$ at room temperature to 100 $\mu\Omega cm^2$ at 1000 K. Measurement of contact resistance of the interface between HH and Ag electrode at room temperature showed that the contact resistance was as small as 5 $\mu\Omega cm^2$. Therefore, the main contribution to the total contact resistance of the HH/Ca349 segment could be attributed to the contacts of the Ca349 with Ag. It can also be observed in Fig. 5.5c that the interfacial resistance exhibited an abrupt change in their temperature dependences at about 600 K. It might be associated with a first-order transition of $Ca_3Co_4O_{9+\delta}$ [125].

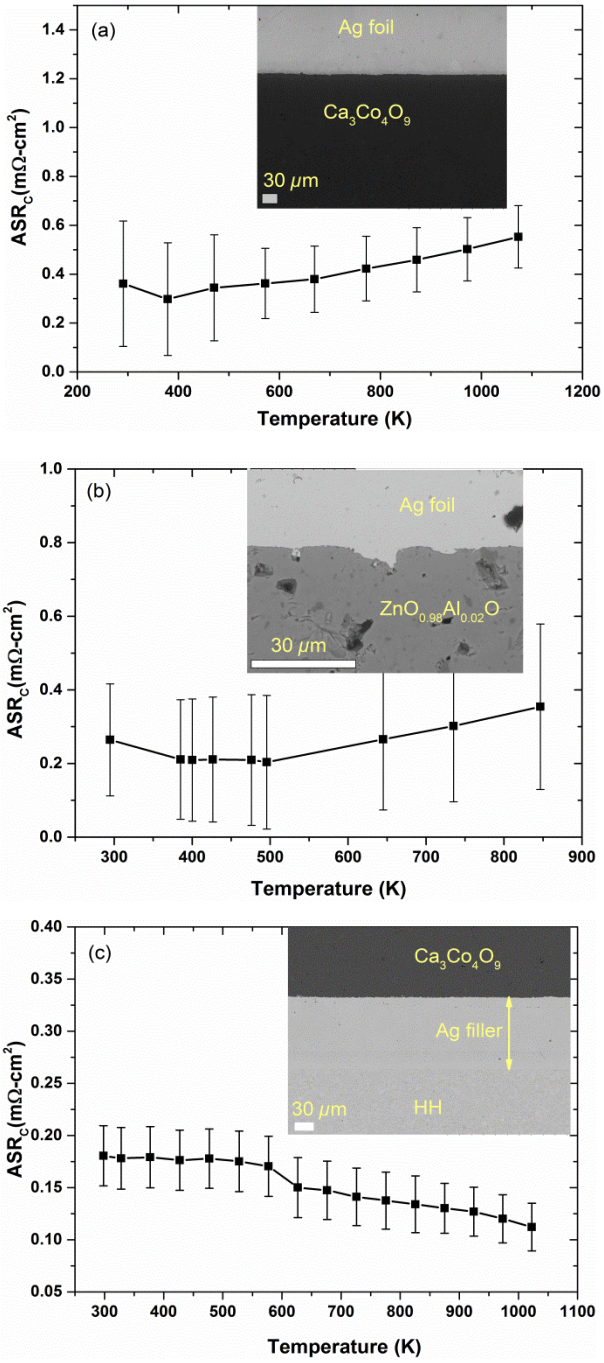

Figure 5.5 (a) Contact resistance of, Ag electrode with Ca349, (b) Ag electrode with 2% Al doped ZnO, (c) the contact resistance of HH/Ag/Ca349 was extracted from sandwich structure and single component Ca349 and HH.

5.4.3 Power generation characteristics of the modules

The power generation of module is expected to improve by using segmented legs as predicted in the modeling part. However, in a realistic working condition there are many factors which effect the output power of modules such as heat losses, contact resistances, heat transfer, etc. In order to demonstrate the influence of segmentation in TEG, two type of 4 *p*-*n* couples modules STEG (*p*-segmented HH/Ca349, *n*-2% Al-doped ZnO) and NTEG (*p*- pure Ca349 and 2% Al-doped ZnO as *n*-legs) were prepared, tested and compared. Figure 5.6a-b shows the power generation characteristics of NTEG and STEG at various applied temperature gradients. As expected, both voltage-current *V* (*I*) and output power-current *P* (*I*) show the same tendency of increasing value as

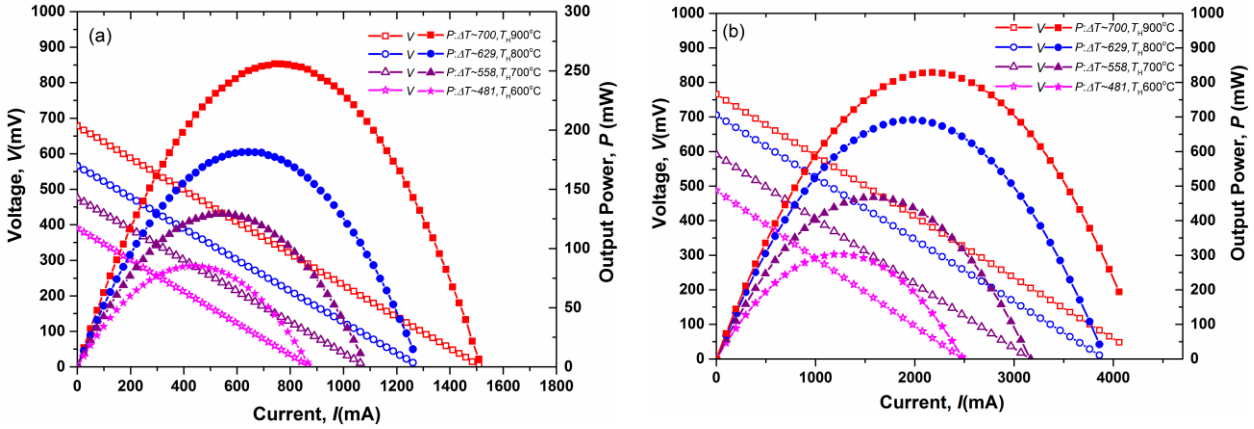

Figure 5.6 Voltages and output power for the 4 p-n couples NTEG (a) and STEG (b) as a function of current under different temperature gradient.

the temperature increases. At the highest applied temperature difference (T_h/T_c = 1173 K/~473 K), $\Delta T \approx 700$ K, the measured open circuit voltage (V_{OC}) of the NTEG was found to be 677 mV, and the voltage decreased linearly with increasing current. The measured maximum output power reached a value of 256 mW at a current of 742 mA and a voltage of 345 mV (Fig. 5.6a). As for the STEG, the measured maximum output power attained 829 mW at $\Delta T \approx 700$ K which is three times higher than that of NTEG.

In order to understand the sources that influence on the obtained experimental results, we have conducted theoretical calculations of the power generation characteristics of the TEGs under ideal conditions i.e. no heat losses or contact resistances (electrical or thermal). The relationship between the open-circuit voltage V_{OC} and the Seebeck coefficients of the TE materials forming the module can be then expressed as [7]:

$$V_{OC} = n \int_{T_c}^{T_h} \{\alpha_p(T) - \alpha_n(T)\} dT \tag{5.11}$$

where T_h and T_c are the hot and the cold side temperatures, n is the number of p-n couples, α_p and α_n are the Seebeck coefficients of p- and n-type legs, respectively. One should note that, the thermocouples used to measure the temperature were placed on surface of Ag electrodes and their thermal contact resistance was assumed to be small. Therefore, the V_{OC} values measured are well reflecting the actual temperature span across the TE legs. At a temperature gradient of about 700 K, the calculated V_{OC} for non-segmented TEG was 685 mV, which is very close to the experimental value of 677 mV.

As for the STEG, formula (11) can be rewritten as:

$$V_{OC} = n \int_{T_m}^{T_h} \alpha_{Ca349}(T) dT + n \int_{T_c}^{T_m} \alpha_{HH}(T) dT - n \int_{T_c}^{T_h} \alpha_n(T) dT \tag{5.12}$$

Where T_m is the temperature at the connection junction. The T_m can be determined by the continuity of the heat flux at the junction, which yields [126]:

$$\kappa_{Ca349}(T_h - T_m) + \alpha_{Ca349} T I = \kappa_{HH}(T_m - T_c) + \alpha_{HH} T I \tag{5.13}$$

In case of the open circuit voltage the T_m can be obtained by:

$$T_m = \frac{\kappa_{Ca349} T_h + \kappa_{HH} T_c}{\kappa_{Ca349} + \kappa_{HH}} \tag{5.14}$$

The T_m was found to be 735 K, and the calculated V_{OC} of segmented was 768 mV which is slightly

higher than the measured value 765.7 mV. At the same temperature difference, $\Delta T \approx 700$ K, the measured V_{OC} of STEG is 100 mV larger than the V_{OC} of NTEG indicating that the voltage of TEG is improved by using HH segmentation.

The magnitude of the output current, I, is proportional to the sum of the internal resistances of the module R_{int} and the external resistive load R_{Load} and it is given by [7]:

$$I = \frac{V_{OC}}{R_{int}+R_{Load}} \tag{5.15}$$

where $R_{int} = R_{legs} + R_C$ is the sum of the resistances of the *p*-*n* legs without metal electrodes R_{legs} and the total contact resistance R_C, which includes the contact resistances at the joining part of segmented leg, the hot-side junction and the cold-side junction.

The power output of the module as a function of V_{OC} and the total resistance is given by

$$P = I^2 R_{Load} = V_{OC}^2 \left[\frac{R_{Load}}{(R_{int}+R_{Load})^2}\right] \tag{5.16}$$

It is clear from Eq. (5.11), (5.12), (5.15) and (5.16) that the power output of the module is dependent on the Seebeck coefficient, the internal resistance and the external load resistance. The maximum power output (P_{Max}) occurs when the external load resistance is equal to the internal resistance. To generate a thermoelectric module at its maximum power output, the load resistance needs to be continuously adjusted to match the internal module resistance.

$$P_{Max} = \frac{V_{OC}^2}{4R_{int}} \tag{5.17}$$

This resistance can vary greatly with temperature due to the temperature dependences of the resistivity of the TE materials itself as well as the temperature dependence of the total contact resistances. It is obvious that the smaller the internal resistance, the higher the maximum output power can be obtained.

In order to give a quantitative evaluation to the results, the internal resistances of the modules (R_{int}) were also calculated from the slope of the fitted *I*-*V* curve using the least-squares method. The obtained result shows that at a $\Delta T \approx 700$ K, the R_{int} of the NTEG and STEG were found to be approximately 447 and 177 mΩ, respectively. Since the electrical resistivity of the HH is much lower than the Ca349 in the temperature range of 473 K to 735 K, the total R_{legs} of the STEG (135 mΩ) was subsequently reduced by 65% as compared to the NTEG (199 mΩ). When combining the higher Seebeck coefficient and lower internal electrical resistance, the maximum output power of the STEG attained a value of 829 mW, which is about three times higher than that of the NTEG counterpart, as clearly shown in Fig. 5.7a.

At $\Delta T \approx 700$ K, the power density (maximum power output divided by the total area of the TE legs) attained about 650 mW/cm^2, which is higher than any reported values of the high temperature oxide modules (see Table 5.2). In order to have a fair comparison in Table 5.2, only the modules comprising of at least 4 p-n couples were selected. The power density can also be expressed as output power divided by the total area of the module; in this case, the value is ~ 200 mW/cm^2 for our STEG. However, in the literature ones often do not report the actual dimension of their modules, making it difficult to compare the results. The obtained results indicate the advantages of using STEG for effective power generation from waste heat recovery where the required device has to work at a high temperature and in oxidizing conditions.

Table 5.2 The power generation characteristics of oxide-based thermoelectric modules reported in literatures.

Ref.	Year	Materials	No. *p*-*n* couples	Jointing technique	T_{hot} (K)	ΔT (K)	V_0 (V)	P_{max} (mW)	Legs-size (mm)	Power Density (mW/cm^2)
[13]	2001	*p*-$Ca_{2.7}Bi_{0.3}Co_4O_9$ *n*-$Ca_{0.92}La_{0.08}MnO_3$	8	Pt paste	773	390	0.9	63.5	3×3	44.1
[14]	2006	*p*-$Ca_{2.7}Bi_{0.3}Co_4O_9$ *n*-$La_{0.9}Bi_{0.1}NiO_3$	140	Ag paste	1072	551	4.5	150	1.3×1.3 ×5	31.7
[5]	2006	*p*-$NaCo_2O_4$ *n*-$Zn_{0.98}Al_{0.02}O$	12	Diffusion welding	839	462	0.8	58	3×4×10	20.1
[16]	2006	*p*-$Ca_{2.7}Bi_{0.3}Co_4O_9$ *n*-$CaMn_{0.98}Mo_{0.02}O_3$	8	Ag paste	897	565	1	170	5×5×4.5	42.5
[7]	2007	*p*-$NaCo_2O_4$ *n*-$Zn_{0.98}Al_{0.02}O$	12	Diffusion welding	934	455	0.8	52.5	3×4×10	18.2
[17]	2007	*p*-$Ca_{2.7}Bi_{0.3}Co_4O_9$ *n*-$CaMn_{0.98}Mo_{0.02}O_3$	8	Ag	1273	975	0.7	340	5×5×4.5	85
[18]	2011	*p*-$Ca_3Co_4O_9$ *n*-$(ZnO)_7In_2O_3$	44	Ag paste	1100	673	1.8	423	15×15× 27	2.1
[127]	2013	*p*-$Ca_{2.76}Cu_{0.24}Co_4O_9$ *n*-$Ca_{0.8}Dy_{0.2}MnO_3$	4	Ag paste	937	321	0.28	31	7×9× 25	6.2
[9]	2014	*p*-$Ca_3Co_4O_9$ *n*-$Zn_{0.98}Al_{0.02}O$	6	Ag	773	248	0.12	2.26	4×4×10	1.2
This work		*p*-$Ca_3Co_4O_9$ *n*-$Zn_{0.98}Al_{0.02}O$	4	Ag	1173	700	0.67	256	4×4×8	200
		p-HH/$Ca_3Co_4O_9$ *n*-$Zn_{0.98}Al_{0.02}O$	4	Ag	1173	700	0.76	829	4×4×8	650

In practical applications, the contact resistances (electrical and thermal contact resistances) and the heat losses (radiation, convection and conduction) are strongly influence on the modules performance, particularly under operation in air and at high temperature [14,30,124,128–130]. Therefore, 3D numerical modeling was used to evaluate the effects of these losses on the performance of STEG and NTEG [118]. The efficiency as a function of current has been calculated for different cases and the results are also given in Fig. 5.7b. The maximum calculated efficiencies including heat losses and contact resistances were found to be 1.16% for the STEG and 0.37% for the NTEG. The model provides the opportunity to study the influence of the contact resistance as well as the heat loss on the efficiency. For the STEG without contact resistance the model predicated an efficiency of 1.51%, while excluding contact resistance and heat loss the efficiency can be as high as

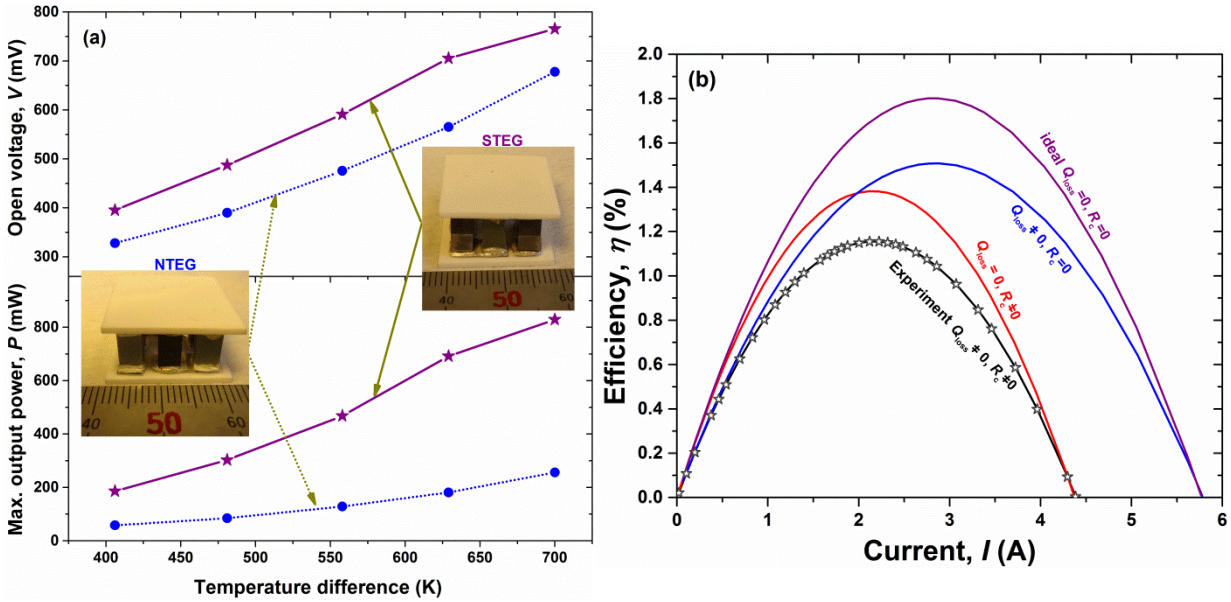

Figure 5.7 The open voltage and maximum output power of NTEG and STEG as a function of temperature differences, ΔT. Inserted photos showing the actual segmented and non-segmented modules. (b) 3D modeling results used experimental measurement data of STEG with and without heat losses (Q_{loss}) and total contact resistances (R_c) at hot and cold side temperatures of 1173/473 K.

1.80%. From, these results it is clear that the overall efficiency of the STEG is reduced due to the combined effect caused by the contact resistances and the heat loss. This illustrates the need for reducing the contact resistance and the heat losses in TEG in general and in these modules in particular.

Besides the high output performance, the long-term stability also plays a very important role in the practical application. Figure 5.8 exhibits the initial long-term stability test of our STEG, which was conducted in air while maintaining the hot side at 1073 K and the cold side at 444 K. These results revealed that the output power of the module was relatively stable in air up to 48 hours with a slight degradation rate of approximately 0.5 mW/h. After 48 h, the maximum output power of STEG was degraded about 4%. The decreasing may be associated with the changing of interfacial contact resistance at the hot side of the oxides with electrodes. However, the further investigations are needed to elucidate the source of this effect.

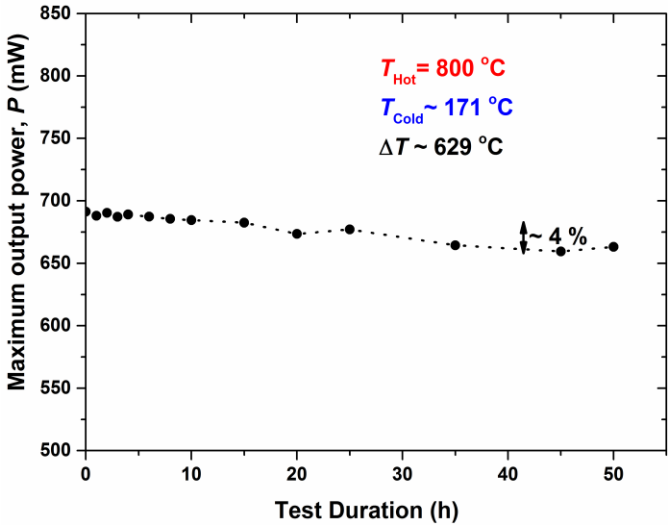

Figure 5.8 The long term stability test of STEG in air at hot and cold sides of 1073/444 K.

5.5 Conclusions

In conclusion, a high temperature segmented thermoelectric oxide-based module comprising of *p*-legs segmentation of $Ti_{0.3}Zr_{0.35}Hf_{0.35}CoSb_{0.8}Sn_{0.2}$ and the misfit-layered cobaltate $Ca_3Co_4O_{9+\delta}$, and *n*-legs 2% Al-doped ZnO has been successfully fabricated and tested for the first time. The enhancement of output power generation was originated from the half-Heusler alloy with higher thermoelectric performance in the low-to-mid temperature range comparing with oxides. The high performance of the STEG also benefitted from the reduction in the total internal resistance of module due to the low contact resistance between the half-Heusler alloy and the Ag electrodes. At a hot side temperature of 1173 K corresponding to a temperature gradient of about 700 K, the maximum power density of the module reached 650 mW/cm^2, which is among the highest values reported so far for oxide-based modules. Using the 3D numerical modeling in combination with the experimental data we found that the efficiency of the STEG (1.16%) was significantly improved as compared with the NTEG (0.37%). Initial long-term testing showed that a segmented oxide module is a promising route for power generation e.g. from waste heat at high temperatures.

Chapter 6 High performance p-type segmented leg of misfit-layered cobaltite and half-Heusler alloy

Abstract

In this study, a segmented *p*-type leg of the doped misfit-layered cobaltite $Ca_{2.8}Lu_{0.15}Ag_{0.05}Co_4O_{9+\delta}$ and the half-Heusler $Ti_{0.3}Zr_{0.35}Hf_{0.35}CoSb_{0.8}Sn_{0.2}$ alloy was fabricated and characterized. The thermoelectric properties of single components, segmented leg, and electrical contact resistance of the joint part were measured as a function of temperature. The output power generation characteristics of segmented legs were characterized in air under various temperature gradients, ΔT, with the hot side temperature up to 1153 K. At $\Delta T \approx 756$ K, the maximum conversion efficiency reached a value of ~5%, which is about 65% of that expected from the materials without parasitic losses. The long-term stability investigation over two weeks at the hot and cold side temperatures of 1153/397 K shows that the segmented leg has good durability as a result of stable, low electrical resistance contacts.

The work presented in this chapter is submitted to Energy Conversion and Management 2014: Le Thanh Hung, Ngo Van Nong, Gerald Jeffrey Snyder, Li Han, Eugen Stamate, Man Hoang Viet, Benjamin Balke, Søren Linderoth, and Nini Pryds, "*High Performance p-type segmented leg of misfit-layered cobaltite and half-Heusler alloy*". Under review

6.1 Introduction

Thermoelectric (TE) power generation devices are offering environmentally friendly power generation from waste heat, and hence have attracted increasing interest in the last two decades as an advanced technology for renewable energy [3,50,99]. Improvements of the efficiency and the durability of the thermoelectric materials have long been the major focused topics. To enhance heat to electricity conversion efficiency, studies on thermoelectrics have been aiming at raising the value of the TE material figure-of-merit, $zT = \alpha^2 T/(\rho.\kappa)$, where α, ρ and κ are the Seebeck coefficient, the electrical resistivity and the thermal conductivity, respectively, and T is the absolute temperature. With increasing value of zT, a higher maximum device energy conversion efficiency η_{max}, which can be expressed as

$$\eta_{max} = \frac{T_h - T_c}{T_h} \frac{\sqrt{1+z\bar{T}}-1}{\sqrt{1+z\bar{T}}+\frac{T_c}{T_h}} \quad (6.1)$$

is expected. T_h is the hot side temperature and T_c is the cold side temperature, $\frac{T_h - T_c}{T_h}$ is known as the Carnot efficiency, and $\bar{T} = \frac{T_h + T_c}{2}$. However, each TE material exhibits their best performance in different temperature range. For *p*-type TE materials, Bi_2Te_3 [3] works the best in the low temperature range from 300 to 450 K, while half-Heusler alloys [8,75], PbTe [131], Zn_4Sb_3 [74] and MnSi [38] operate in the mid-temperature range from 450 to 800 K and oxide materials [11], Zintl compounds [132], SiGe [79] are in the high temperature range from 800 to 1200 K. Therefore, a thermoelectric power generator (TEG) constructed from single materials is limited to a particular operation temperature range, which is determined by the type of materials used [3,133]. In this context, a segmentation of different thermoelectric materials shows their best performance in different temperature ranges has been demonstrated as one of the most effective methodologies to achieve high thermoelectric efficiency [8,25,28,34,70]. By this way, a segmented leg can operate with its highest efficiency in specific wide temperature range.

Under high temperatures (>750 K) in air, oxide TE materials could be one of strong candidate due to their chemical stability, low-cost and abundant source in comparing with intermetallic compounds [11,53,55]. Among *p*-type polycrystalline TE oxide materials, the doped layered-cobaltite $Ca_{2.8}Lu_{0.15}Ag_{0.05}Co_4O_{9+\delta}$ (CCO) material could attain a peak $zT = 0.61$ at 1100 K [44]. This material also shows a very good durability over many thermal cycles in air at high temperature [44]. However, like other TE oxide materials, CCO only shows good performance in the high temperature range. Although many modules have been fabricated and characterized using a different combination of *p* and *n*-type of TE oxide materials such as *p*-type $Ca_3Co_4O_9$ and *n*-type $CaMnO_3$ or ZnO [8–11], or *p*-type $NaCo_2O_4$ and *n*-type ZnO [15], the estimated conversion efficiencies are still lower than 3%.

It is seen from equation (6.1) that besides the zT, the conversion efficiency can also be significantly increased as the operating temperature increases. With the purpose of making a low-cost, high performance and high-temperature TE segmented leg, CCO is chosen as hot side material to combine with other materials. However, in order to achieve an improved efficiency segmented TE leg, the

materials to be segmented must have a difference in compatibility factors ($s = \frac{\sqrt{1+zT}-1}{\alpha T}$) within a factor of two according to the concept suggested in Refs. [25,26].
In this work, the segmentation of *p*-type the half-Heusler $Ti_{0.3}Zr_{0.35}Hf_{0.35}CoSb_{0.8}Sn_{0.2}$ (HH) and the $Ca_{2.8}Lu_{0.15}Ag_{0.05}Co_4O_{9+\delta}$ (CCO) is selected based on the calculation results of the compatibility factor and total conversion efficiency. The *p*-type segmented HH/CCO legs were then fabricated, and their thermoelectric properties, as well as electrical contact resistances between the two parts of the legs, were investigated as a function of temperature. The performances i.e. the output power and efficiency of the segmented legs, were measured at different temperature span with hot side temperature up to 1153 K. The influence of the contact resistance on the total conversion efficiency was evaluated, and correlated with the calculated results.

6.2 Modeling

6.2.1 Calculation model

With the purpose of evaluating the efficiency of non-segmented and segmented TE elements, a one-dimensional (1D) model of the thermoelectric legs is used [8,24]. This model takes into account all thermoelectric effects i.e. the Peltier, Seebeck and Thomson effects, as well as heat conduction, Joule heating and the temperature dependence of the resistivity, ρ(T), thermal conductivity κ(T) and Seebeck coefficient, α(T). In these calculations, the efficiency of segmented and non-segmented TE elements were calculated under the ideal conditions, i.e. neglecting all the heat losses, and thermal and electrical contact resistances. The calculations can, therefore, be considered as an upper limit for the actual obtainable efficiency in experiments. The 1D model solves for the reduced current density u (= $J/\kappa\nabla T$), which is defined as the ratio between the electrical current density (J) and the heat flux by conduction. The u values at any temperature can be determined by solving the following differential equation

$$\frac{du}{dT} = u^2 T \frac{d\alpha}{dT} + u^3 \rho\kappa, \tag{6.2}$$

with an approximate recursive solution [24]. The differential equation is valid for both non-segmented and segmented legs if – for the latter – the material properties are changed from one material to another at a particular known interface temperature (T_m) where the segments meet. The reduced current densities at the various temperatures can be calculated by numerical method using the following equation:

$$\frac{1}{u_n} = \frac{1}{u_{n-1}} \sqrt{1 - 2u_{n-1}^2 \overline{\rho\kappa} \Delta T} - \bar{T}\Delta\alpha, \tag{6.3}$$

here, $\Delta\alpha = \alpha(T_n) - \alpha(T_{n-1})$ and $\overline{\rho\kappa} = [\rho(T_n)\kappa(T_n) + \rho(T_{n-1})\kappa(T_{n-1})]/2$. From u values, the total (η_{leg}) efficiencies of a segmented or non-segmented leg can be calculated using the following expressions:

$$\eta_{leg} = 1 - \frac{\alpha_c T_c + \frac{1}{u_c}}{\alpha_h T_h + \frac{1}{u_h}} \tag{6.4}$$

As can be seen from equation (6.4) that the efficiency values of the leg are defined by u(T) which calculated in term of temperature dependent thermoelectric properties i.e. Seebeck coefficient, thermal conductivity and electrical conductivity.

For a situation where the dimensions of the legs are fixed, i.e. the length (l) and the cross-sectional area, the current density can be calculated in term of u and κ along the leg.

$$J = \frac{1}{l}\int_{T_c}^{T_h} u\kappa \mathrm{dT} \qquad (6.5)$$

The total electric power density then can be determined by using the following expression $P_d = JV$, where voltage can be expressed as [24,26]:

$$V = \frac{1}{u_h} + \alpha_h T_h - \frac{1}{u_c} - \alpha_c T_c \qquad (6.6)$$

6.2.2 Efficiency of single materials and segmented legs

According to Snyder [25], the compatibility factors of the prospective materials should be within "a factor of two" to obtain high efficiency of a segmented leg. Fig. 6.1a shows the figure-of-merit of some typical *p*-type TE materials in the temperature region from 300 to 1200 K. For temperatures above 750 K, SiGe [79] and $Yb_{14}MnSb_{11}$ [132] are the potential candidates which show high TE performance ($zT_{max} \approx 1$). However, TEGs based on these materials often require a complex processing in inert gas or vacuum, followed by encapsulation of the legs to protect them against oxidation at high temperature in air [83,84,128]. In contrast to conventional metallic alloys, the CCO oxide can be processed in air, and its high-temperature stability in air has been demonstrated [44]. In addition, the bulk material cost of CCO is only 1.2 \$/mol, which is much lower than that of e.g. 147 \$/mol for $Si_{80}Ge_{20}$ and 19000 \$/mol for $Yb_{14}MnSb_{11}$. Bulk material cost is the costs of all precursors and the manufacturing cost that require for producing 1 mol bulk material. The prices of precursors are taken from Alfa Aesar [89]), while the manufacturing costs are followed the data

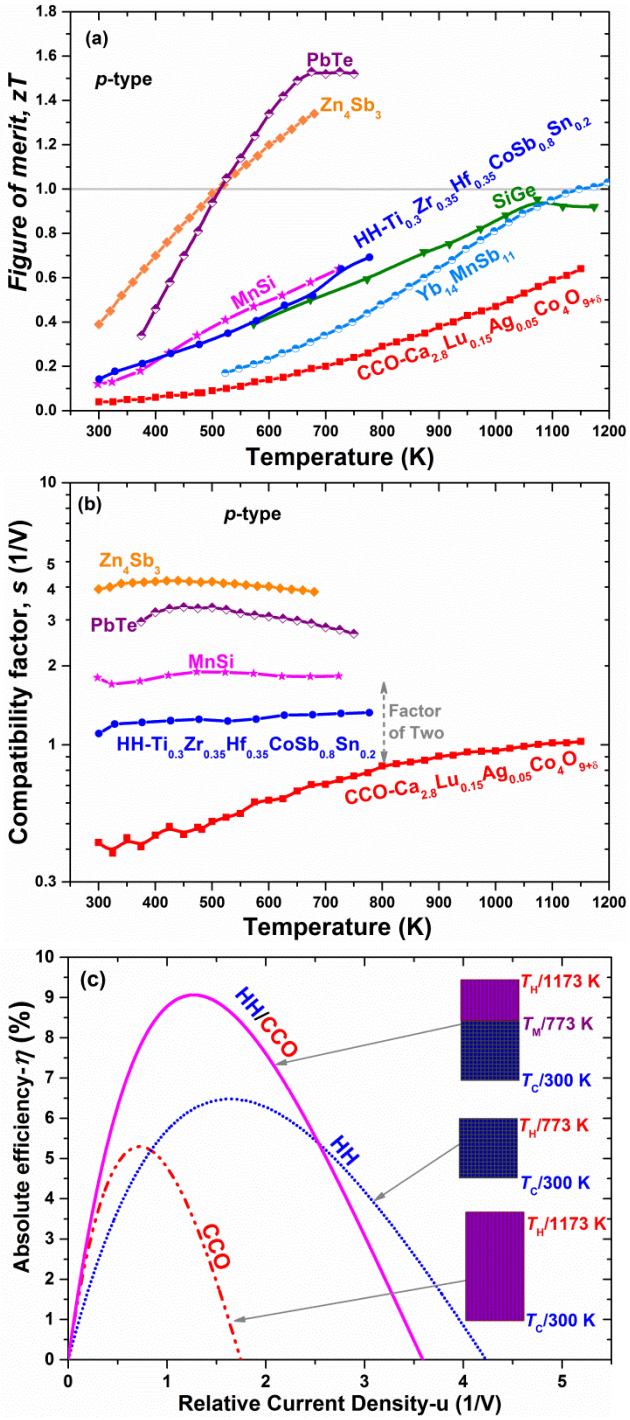

Figure 6.1 Selected dimensionless figure-of-merit zT of state of the art p-type TE materials, (b) temperature dependence of compatibility factors of MnSi, HH and CCO. (c) Calculated efficiency of single CCO, HH and segmented HH/CCO.

reported by LeBlanc et al. [90]. With above reasons, CCO has been chosen as key material for the high temperature (above 750 K) part of the segmentation. In order to achieve high performance over a large temperature range, ideally, CCO should combine with materials that have high performance in the low-mid temperature range. At a temperature below 750 K, the PbTe [131], Zn_4Sb_3 [74], HH [8] and MnSi [38] are the potential candidate materials showing high TE performance. However as can be seen from Fig. 6.1b, although the PbTe and the Zn_4Sb_3 have high peak *zT* values their compatibility factors are more than two times larger than that of CCO, pointing out that they are incompatible. The only compatible materials with the CCO are the HH and the MnSi, which lie within a factor of two. In this study, we have chosen the HH for the reason that its compatibility factors are more closer to the CCO (Fig. 6.1b) than those of MnSi. In addition, the average *zT* is higher for the HH (0.43) than for the MnSi (0.36) over the same temperature range. Fig. 6.1c shows the calculated efficiency for CCO, HH and segmented HH/CCO legs. The maximum efficiency of segmented HH/CCO leg attained a value of 9.1%, which is about 60% higher than the single material CCO (5.3%) under the temperature difference of 1173/300 K (Fig. 6.1c). Since the HH alloys can not be sustained at higher temperature due to sublimation and oxidation, its maximum efficiency could only reach a value of 6.4% at hot and cold side temperatures of 773/300 K. Therefore, the segmented HH/CCO legs are expected to have higher performance in comparison with the non-segmented legs as a result of increasing *zT* and larger temperature span.

6.3 Experimental procedures

6.3.1 Materials preparation and characterization

Polycrystalline samples of $Ca_{2.8}Lu_{1.5}Ag_{0.05}Co_4O_{9+\delta}$ (CCO) were synthesized by solid-state reaction. Commercial precursors of $CaCO_3$ (99.5%), Co_3O_4 (99.7%), $AgNO_3$ (99.9+ %) and Lu_2O_3 (99.9%) with appropriate ratio were thoroughly mixed by ball milling with ethanol for 36 h. The mixtures were dried and then calcined at 1203 K for 48 h in air with an intermediate grinding procedure. The calcined powder was densified using spark plasma sintering (SPS) system (SPS-515S Syntex Inc., Japan). The samples were heated to 1123 K, while a uniaxial pressure of 50 MPa was applied for 5 min. The details of this work could be seen elsewhere [44].

HH compound samples with the stoichiometric composition of $Ti_{0.3}Zr_{0.35}Hf_{0.35}CoSb_{0.8}Sn_{0.2}$ were synthesized by arc melting of the pure (99.999%) metals Ti, Zr, Hf, Co, Sb, and Sn under argon atmosphere. In the course of the arc melting, to ensure the homogeneity of the samples, samples were re-melted and turned over three times. The synthesized ingots were milled for 4 h at 700rpm in a high-energy ball milling station (PULVERISETTE 7 premium line, Fritsch, Germany) under a protective argon atmosphere. The powder was then filtered through a 60-mesh sieve and spark plasma sintered at 1373 K for 20 min (heating/cooling rates of 50 K/min) under mechanical pressure of 50 MPa.

Before and after sintering, the samples were examined by X-ray diffraction (XRD) on a Bruker D8 diffractometer (Bruker, Germany) using Cu-Kα radiation. The measurements of the electrical resistivity and the Seebeck coefficient were carried out on a ULVAC-RIKO ZEM-3 from room

temperature up to 1200 K under a low-pressure helium atmosphere. The thermal conductivity (κ) was determined from the thermal diffusivity (γ), the mass density (ρ) and the specific heat capacity (C_p) according to the equation $\kappa = \gamma\rho C_p$. The thermal diffusivity was obtained by the laser flash method (Netzsch LFA-457, Germany), the mass densities of the samples were measured by Archimedes' method using water with a surfactant, and the specific heat capacity was measured using a differential scanning calorimeter (Netzsch DSC 404C, Germany). Scanning electron microscope (SEM, Supra; Carl Zeiss, Inc., Germany) was used to observe the microstructures of the samples.

6.3.2 Segmented legs fabrication and characterization

For the fabrication of segmented legs, the obtained pellets of CCO and HH were cut, polished and then cleaned with acetone, isopropyl alcohol and deionized water and finally dried with nitrogen gas. As designed, the segmented HH/CCO leg can work at hot side temperature up to 1173 K with interface temperature T_m = 773 K and cold side temperature 300 K, the lengths of CCO and HH were calculated to be 2 and 4 mm, respectively. 150 µm thick Ag foil with a purity of 99.99% was used as the joining material between the HH and the CCO while 600 µm thick Ag foil was used to make electrodes. Brazing joining process was conducted in a vacuum using the SPS under 20 MPa at 973 K for 10 min to achieve a good contact between the two materials.

The electrical contact resistance is the interface resistance, which is multiplied by the cross-sectional area of the interface to give the area specific resistance of the interface (ASR). Fig. 6.2a demonstrates a method for measuring the contact resistance between the different TE materials in a segmented leg using the ZEM-03. The contact resistance can be determined by measuring the electrical resistivity of individual TE and v_3) materials (v_1 and the resistance across the interface of the segmented materials (v_2). By measuring the contact resistances of the sample with various cross-sectional areas (A_R), the ASR is then calculated from the slope of the fitted R^{-1}/A_R curve using the least-squares's method.

The power generation characteristics of the segmented legs were performed in air using an in-house Rig-test system. The *I-V* curves at different ΔT were automatically measured by sweeping the current from 0 to 15 A with a minimum step of 1 mA. The controlled software system is based on Apache web server software (Open Source Software, OSS) and allow flexibility with regard to the type gas control, cycling, long-term stability tests, etc. In order to define the accurate temperature difference

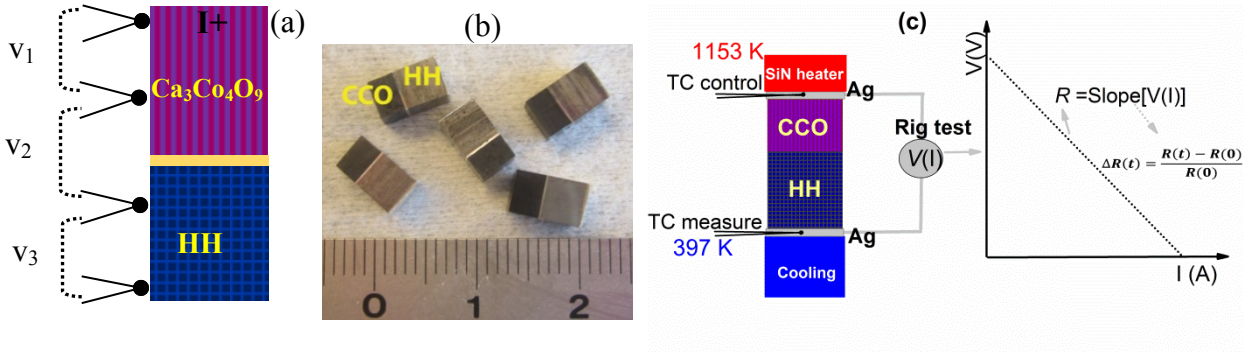

Figure 6.2 (a) Schematic configuration of the voltage probes along the segmented leg. (b) Images of the fabricated segmented HH/CCO legs. (c) Schematic of the long-term stability measurement configuration using test Rig system.

across the leg, 0.5 mm n-type thermocouple was directly inserted inside the Ag electrodes at the vicinity of the top part of the leg. The thermocouple at the hot side is also used for setting up the PID of the heater controller (Fig. 6.2b). To minimize the heat losses during the test, the heater was covered by a thick layer of silica felts.

6.4 Results and discussion

6.4.1 Electrical properties of single and segmented legs

In thermoelectric power generation devices, the magnitude of the measured electrical current is inversely proportional to the total electrical resistivity of the TE leg including their interfacial electrical contact resistance. For a segmented TE leg, the total contact resistance usually increases due to the increasing number of interfaces. Therefore, minimizing the electrical contact resistance between joined materials is of prime important in the module construction process.

Fig. 6.3a shows the temperature dependence of the electrical resistivity of CCO, HH, and segmented HH/CCO legs. As expected, the HH samples revealed a metallic conduction behavior while the CCO sample displayed a semiconductor-like electrical resistivity. As can be seen from this figure, the electrical resistivity of CCO is higher by a factor of eight compared with the HH in the low temperature range. Unsurprisingly, the electrical resistivity of segmented HH/CCO is between the electrical resistivity of CCO and HH. The experimental result exhibited the same tendency with the calculated one. The difference between these curves could be attributed to the interfacial electrical contact resistance at joint part of HH/Ag/CCO. Fig. 6.3b displays the contact resistance of the joint part as a function of temperature. Over measured temperature range, the contact resistance values are around 100 $\mu\Omega cm^2$, which is lower than the previously reported values of 800 $\mu\Omega cm^2$ for the electrical contacts of pure $Ca_3Co_4O_{9+\delta}$ with $Fe_{22}Cr$ electrode [125]. There is no crack or gap could be observed at the interfaces between HH and CCO with Ag (see Fig. 6.3b inset). In addition, EDX

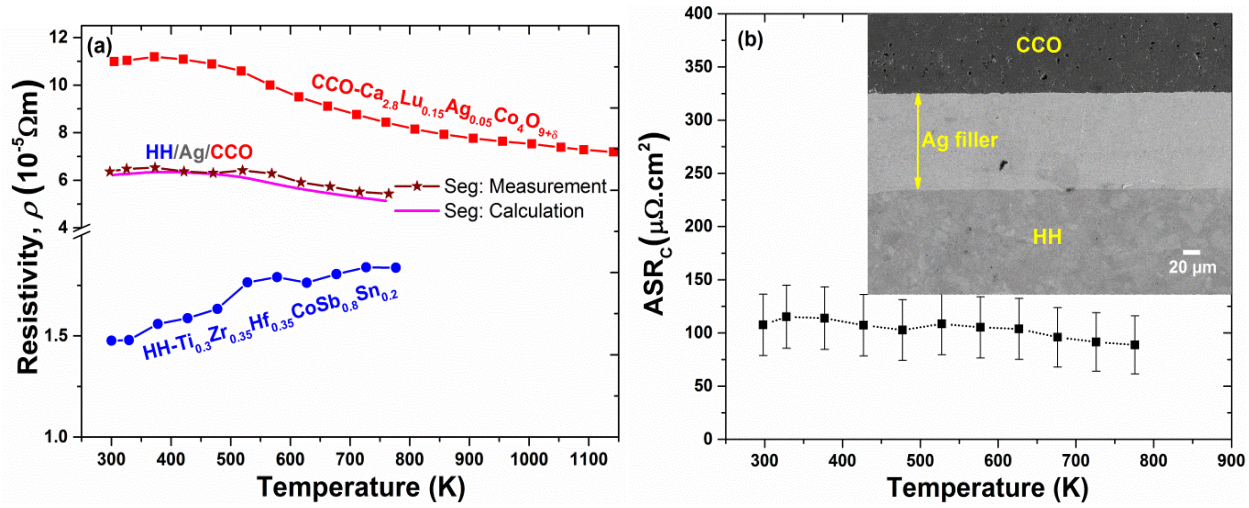

Figure 6.3 (a) Temperature dependence of the electrical resistivity of CCO, HH, and segmented HH/CCO. Star symbol curve denotes the calculated electrical resistivity. (b) The electrical contact resistance of joint interface HH/Ag/CCO as a function of temperature, inset SEM picture of HH/Ag/CCO.

analysis at the interfacial region (not shown here) revealed that there is no reaction or significant diffusion layer. These observation may explain for the lower measured interfacial contact resistance than that reported in [30] with $Fe_{22}Cr$ electrode. Measurement of the contact resistance of HH/Ag at room temperature revealed that the electrical contact resistance is in the order of 5 $\mu\Omega cm^2$, suggesting that the contact resistance at the cold side of HH/CCO segmented leg is small. The total electrical resistance of the TE leg is the sum of the resistances of the TE materials R_{legs} without silver electrodes and the total contact resistance R_C, which includes the contact resistances at the joining part, the hot and the cold side junctions. At hot and cold side temperatures of 1173/300 K, the ratio of R_C/R_{legs} is about 0.08. These results indicate that the Ag brazing is an effective way to achieve low electrical contact resistance.

6.4.2 Thermopower at small and large ΔT

For the thermoelectric modules construction, it is important that the TE properties of a single or segmented leg can be maintained after the joining process. Therefore in this work, the TE properties as a function of temperature of joined segmented legs of HH/CCO as well as single HH and CCO were carefully characterized. Fig. 6.4a shows the temperature dependence of the Seebeck coefficient (α) of the single CCO, HH and the segmented HH/CCO legs. For both the single and segmented samples, the Seebeck coefficient (α) increased with increasing temperature (Fig. 6.4a). The α values of CCO were measured to be about 150 μV/K and 235 μV/K at room temperature and 1140 K, respectively. As for the HH alloys, α increased from 160 to 230 μV/K as the temperature increased from room temperature to 700 K. In the segmented HH/CCO, the α values were in between the values of two single components. The intrinsic α value of segmented leg can be expressed via single components as [126]:

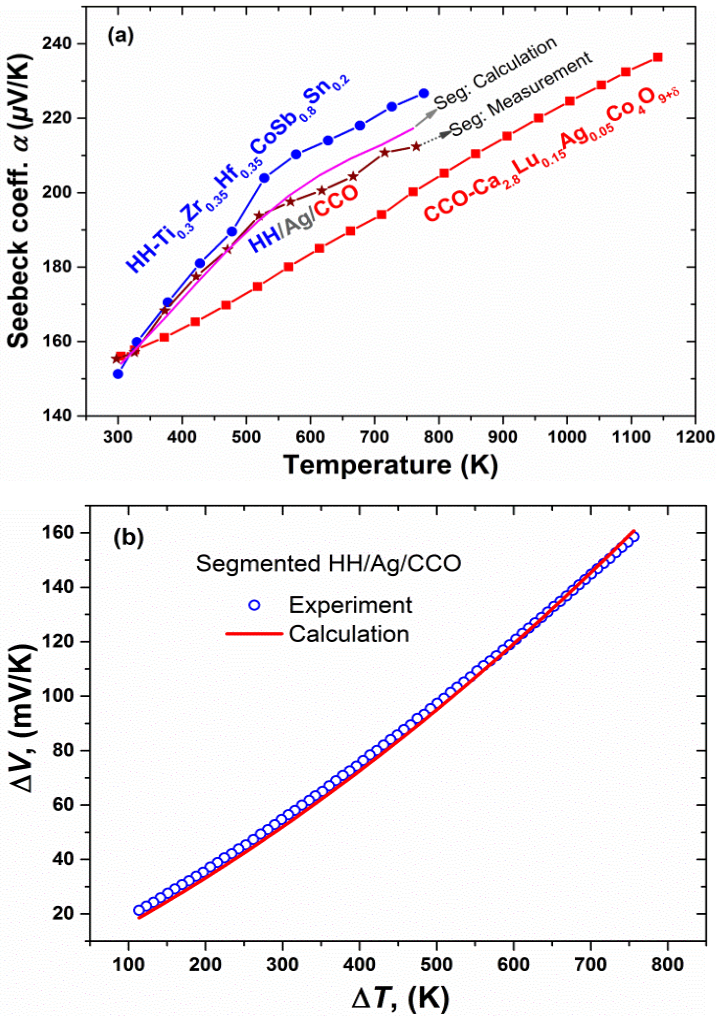

Figure 6.4 (a) Temperature dependence of Seebeck coefficient of CCO, HH, segmented HH/CCO legs at small temperature gradient. (b) The calculated and experimental total Seebeck coefficient of the segmented leg HH/CCO under large temperature gradient.

$$\alpha_{seg} = \frac{\Delta V}{\Delta T} = \frac{\kappa_{HH}\alpha_{HH} + \kappa_{\mathrm{CCO}}\alpha_{\mathrm{CCO}}}{\kappa_{HH} + \kappa_{\mathrm{CCO}}} \quad (6.7)$$

Where α_{seg} is the Seebeck coefficient of the segmented HH/CCO leg, κ_{HH}, α_{HH}, κ_{CCO}, α_{CCO} are thermal conductivity, Seebeck coefficient of HH alloys, thermal conductivity and Seebeck coefficient of CCO, respectively. In the calculation of α_{seg} using equation (6.7), the thermal contact of CCO and HH with silver filler was neglected. The measured α_{seg} is in good agreement with the calculation although there is a small fluctuation in the temperature range from 550 to 700 K (Fig. 6.4a). These results indicated that the silver brazing at the interface preserved the intrinsic thermopower of the segments at small temperature difference.

Fig. 6.4b shows the calculated and experimental open circuit voltage (ΔV_{oc}) of the segmented leg HH/CCO at various temperature differences (ΔT). It can be seen that the open circuit voltage increased rapidly with increasing ΔT. The experimental and calculated ΔV_{oc} curves are well fit, suggesting that thermal contact resistance at the interfaces as well as the heat loss through the segmented leg are very small. The relationship between the open-circuit voltage ΔV_{oc} and the α value of the single TE material can be then expressed as [7]:

$$\Delta V_{oc} = \int_{T_c}^{T_h} \alpha(T) dT \quad (6.8)$$

Where T_{h} and T_{c} are the hot and cold side temperatures, respectively. As for the segmented leg, equation (6.8) can be rewritten as:

$$\Delta V_{oc-seg} = \int_{\mathrm{T}_m}^{\mathrm{T}_h} \alpha_{\mathrm{CCO}}(T)\mathrm{dT} + \int_{\mathrm{T}_c}^{\mathrm{Tm}} \alpha_{HH}(T)\mathrm{dT} \quad (6.9)$$

where T_{m} is the temperature at the connection junction. In case of the open circuit voltage the T_{m} can be determined by the conservation of the heat transfer at the junction. The one-dimensional the heat flow equation, q, can be expressed as Fourier's law:

$$q = \kappa \frac{\Delta T}{l} A \quad (6.10)$$

Where A is the cross-sectional area and l is the length of the TE leg. T_{m} can then be obtained as:

$$T_m = \frac{\kappa_{CCO} T_h l_{HH} + \kappa_{HH} T_c l_{CCO}}{\kappa_{CCO} l_{HH} + \kappa_{HH} l_{CCO}} \quad (6.11)$$

T_{h}, T_{c}, l_{HH} and l_{CCO} are the hot side temperature, the cold side temperature, the length of HH and the length of CCO, respectively. Under the highest hot side temperature of 1153 K and cold side of 397 K, T_{m} is found to be 737 K, and the calculated $\Delta V_{oc\text{-seg}}$ of the segmented leg was 160 mV that is almost the same as the measured value of 158.6 mV. The measured data of $\Delta V_{oc\text{-seg}}$ (blue open circle) exhibits similar tendency with the calculated line (red solid line). This result again suggests that the silver brazing is a suitable material for joining between semi-metal (HH) and oxide materials (CCO).

6.4.3 Power generation characteristics

Fig. 6.5a exhibits the experimental results on the voltage V and output power density P_{d} depended on the current density J of the segmented HH/CCO leg at various applied temperature gradients. As can be seen, both V and P_{d} present the same tendency of increasing values as the temperature gradient increases. At the highest applied temperature difference ΔT = 756 K ($T_{\mathrm{h}}/T_{\mathrm{c}}$ = 1153 K/397

K), the measured open circuit voltage ($V_{oc} \equiv \Delta V_{oc\text{-seg}}$) of the segmented leg was found to be 158.6 mV, and the measured maximum output power density reached a value of 2.34 W/cm^2 at a current density of 30 A/cm^2 and a voltage of 81 mV (Fig. 6.5a). In practice of making TEG, the contact resistance is one of the main factors affecting the conversion efficiency [30,50]. In order to evaluate this effect, the measured power generation characteristics of the segmented legs were analyzed and compared with the theoretical results under both ideal (no contact resistance) and practical conditions (including contact resistance). The magnitude of the output current density, $J = I/A$, is proportional to the sum of the internal resistances of the TE leg, R_{int}, and the external resistive load, R_{Load}, and it is given by the following expression [7]:

$$J = \frac{I}{A} = \frac{V_{oc}}{A(R_{int}+R_{Load})} \tag{6.12}$$

where $R_{int} = R_{leg} + R_C$ is the sum of the resistances of the segmented legs without metal electrodes R_{leg} and the total contact resistance R_C.

The output power density of the leg as a function of V_{oc} and the resistance is given by

$$P_d = J^2 R_{Load} = \frac{V_{oc}^2}{A}\left[\frac{R_{Load}}{(R_{int}+R_{Load})^2}\right] \tag{6.13}$$

Equation (6.13) clearly shows that the power output of the leg depends on the Seebeck coefficient (via V_{oc}), the internal resistance and the external load resistance. The maximum output power density (P_{Max}) occurs when an external load resistance is equal to the internal resistance. To operate thermoelectric devices at a maximum output power, the load resistance needs to be continuously adjusted to match the internal resistance.

$$P_{Max} = \frac{V_{oc}^2}{4AR_{int}} \tag{6.14}$$

Disregarding the varying dimensions of the segmented legs due to thermal expansion, it is obvious that the smaller the internal resistance, the higher the maximum output power obtained. In our measurement, the influence of heat losses (radiation and convection) could be negligible since the segmented leg is small and well covered by a thick layer of the thermal insulator material (silica felts). To investigate the influence of the electrical contact resistance on the conversion efficiency of segmented leg, the model described in detail in Ref. [24] was used. Fig. 6.5b shows the experimental

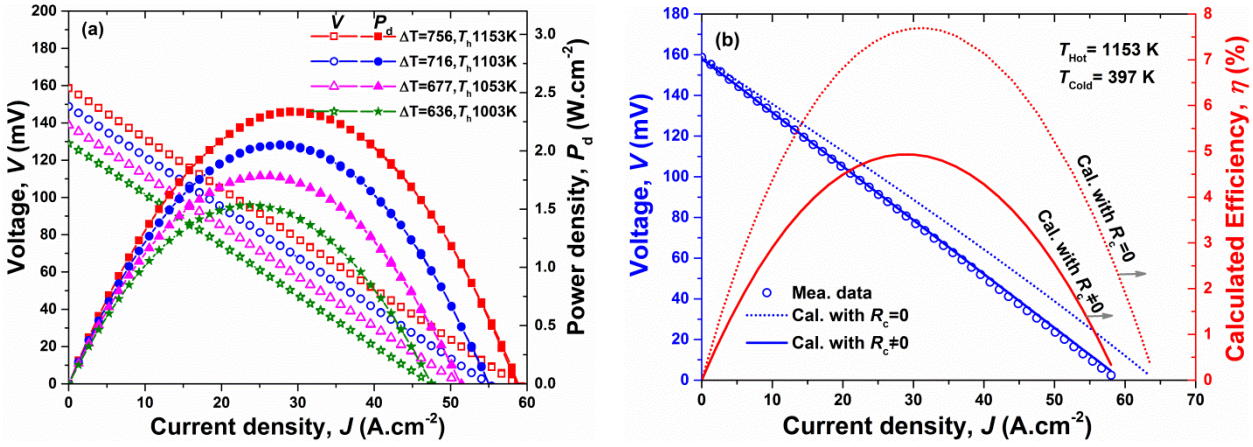

Figure 6.5 (a) Voltages and output power for the segmented HH/CCO legs as a function of current density under different temperature gradient. (b) The experiment and calculation of V(J) and the efficiency of the segmented legs with and without the electrical contact resistances at highest temperature difference.

and calculated *V-J* and *η-J* curves with and without the electrical contact resistances for the segmented leg at the highest temperature difference. As seen in Fig. 6.5b, the measured voltage, *V,* (blue open circle) fitted well with the calculated one (blue solid line) which included the contact resistance, R_C. From the slope of the *I-V* curves, the electrical resistance of the segmented leg was determined to be 164.2 mΩ and 179.6 mΩ for the conditions with and without interfacial contact resistances, respectively. These results indicate that the electrical contact resistance contributed about 8.6% to the total resistance of the leg, which is in good agreement with calculated 8% under ideal one-dimensional heat flow (hot and cold side temperatures of 1173/300 K). The efficiency as a function of current density has also been calculated for different cases, and the maximum values were found to be 7.6% and ~5% for the segmented HH/CCO leg without and with contact resistances, respectively. The efficiency of our segmented leg is comparable to the efficiency of commercial modules (e.g., module TG12-4-01Lby Marlow Industries, Inc.) constructed from state-of-the-art *p* and *n* TE materials but lower than the BiTe/PbTe segmented modules, which can reach 6.5% [28]. This is the first time an oxide-based segmented leg has been tested in an oxidative condition at high temperature. The results of the test clearly show that contact resistance strongly influenced on the total conversion efficiency, and, in this case, the suppression was about 35%. This investigation suggests that the efficiency of segmented leg can be significantly improved by reducing further the contact resistance. Forming a buffer layer of good conductive material of e.g. metal or alloy between oxide and electrode may be a good solution to minimize the contact resistance.

6.4.4 Long-term stability investigation

Besides improving the thermoelectric conversion efficiency of TEGs, the long-term stability is equally important for application of heat-electricity energy conversion. Oxide-based TEGs can be potentially used for waste heat recovery at high temperatures e.g., >750 K from metal refining furnaces, which is often switched off once/month. Therefore, in this study we have performed the long term stability test of the segmented leg at a constant high temperature. Fig. 6.6 displays the maximum power density and the changed total resistivity over a period of 336 h for the segmented HH/CCO leg. All the measurements were conducted in air by keeping the hot and the cold side temperatures at 1153/397 K. The *I-V* curves during these measurements were recorded every 30 min. The overall resistances of the legs including silver joint and electrodes were then calculated from the slope of

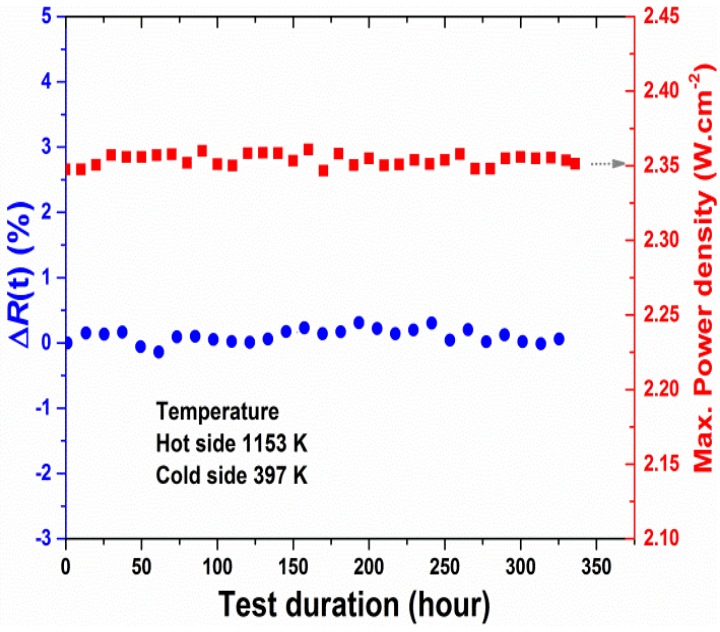

Figure 6.6 The long term stability test of the HH/Ag/CCO leg in air under hot and cold side temperatures of 1153/397 K.

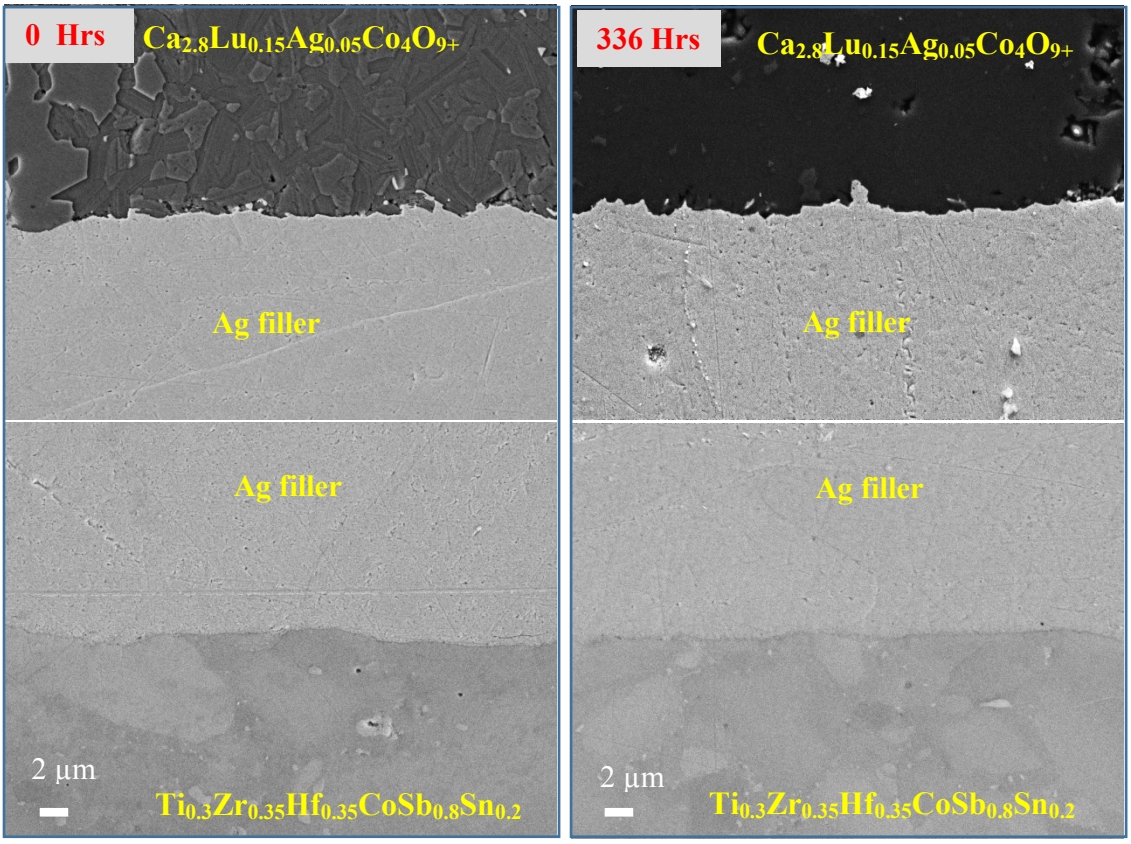

Figure 6.7 SEM joint interface of CCO/Ag and HH/Ag after joining 0 Hrs and after test 336 Hrs in air with hot and cold side temperatures of 1153/397 K.

the *I-V* curves. Interestingly, the total resistance and the maximum power density of the segmented HH/CCO leg remain almost constant up to 336 hours. In addition, the *I-V* curves (not shown here) were linear pointing out that the Ohmic contacts were maintained during the test at high temperature.

Fig. 6.7 shows SEM images of the HH and CCO with Ag joint cross-section at 0 h and 336 h operated at 1153 K. It can be seen from the micrographs that interfacial contacts remained the same good quality i.e. no evidence for cracks or elemental diffusions was observed at the interfaces. This observation is in good agreement with the almost unchanging total resistance of the HH/CCO segmented leg over a long period of holding time.

Fig. 6.7 shows SEM images of the HH and $Ca_3Co_4O_9$ with Ag joint cross-section before and after the long-term experiments. The micrographs confirm that contacts are stable, i.e. no evidence for cracks or elemental diffusions were observed at the interfaces. Noticeably, microstructure of $Ca_3Co_4O_9$ was even enhanced after a long time testing at high temperature.

6.5 Conclusions

In summary, for the first time the segmented *p*-type leg of the half-Heusler $Ti_{0.3}Zr_{0.35}Hf_{0.35}CoSb_{0.8}Sn_{0.2}$ and the doped misfit-layered cobaltite $Ca_{2.8}Lu_{0.15}Ag_{0.05}Co_4O_{9+\delta}$ (CCO) was successfully fabricated and characterized using the silver brazing joining technique. With this

technique, the total contact resistance was obtained to be about 8% of the total resistance of segmented leg. The calculation results pointed out that CCO and HH have their compatibility factors close to each other, and thus the efficiency of HH/CCO segmented leg could be improved to a value of 9.1% under conditions without parasitic losses. The output power generation characteristics of the segmented legs were measured in air with various temperature gradients, ΔT. At ΔT of about 756 K, the maximum generated power density attained 2.34 W/cm^2 corresponding to ~5% conversion efficiency, which is about 65% of the ideal condition. Long term stability investigation for over two weeks in air suggests that this oxide-based segmented leg is very promising for generating electricity from high temperature waste heat. According to our recent report [134], n-type segmented leg of doped ZnO and half-Heusler could be a promising partner to build up low-cost high performance oxide-based TEG.

.

Chapter 7 Summaries and outlooks

Summary of some selected main results obtained in this thesis are given below:

- Theoretical description of segmented thermoelectric generators have been formulated and numerically solved. A rule of thumb when selecting a segmented material is that the difference in compatibility factors of two different thermoelectric materials should be within a factor of two. This has been proven theoretically by obtaining the conversion efficiency of *n*-type segmented ZnO with HH and CoSb. The one-dimensional numerical modelling has been developed and used to evaluate the efficiency of single and segmented oxide based materials. A new concept was used to select segmented materials and it is based on their figure-of-merit, the "efficiency ratio" and their compatibility factors. In comparison with other metallic alloys, it was found that oxides materials are good candidates for hot-side materials for building up low-cost, high performance segmented legs/unicouples. A maximum efficiency of more than 10% was calculated for the unicouples made of segmented legs of *p*-$Ca_3Co_4O_9$ and *n*-ZnO with intermetallic compounds such as HH and BiTe. The results of the modeling indicate that building TEG-based segmented legs include a trade-off between the increment in conversion efficiencies and the module processing and fabrication costs, effects that should be taken into consideration when building a module. The obtained results suggest a useful tool to construct low-cost and high-efficiency thermoelectric modules based on oxide materials for a high-temperature power generation.
- *n*-type oxide $CaMnO_3$ compound includes environmentally friendly materials and offers a stable thermoelectric properties in oxidative condition at high temperature and used in commercial oxide modules. The effect of Fe substitution on the structure and the high-temperature thermoelectric properties of $Ca_{0.9}Y_{0.1}Mn_{1-x}Fe_xO_3$ (x = 0, 0.05, 0.1, 0.15, 0.2, 0.25) was investigated in details. Structural analysis shows that lattice parameters slightly increase with increasing amount of Fe substituent, which originates from the difference in the ionic radii between Fe and Mn ions. The thermoelectric properties were found to be improved for the Fe-doped samples with $x < 0.1$, particularly for the SPS samples with further annealing mainly due to the increase in the Seebeck coefficient that could overcome the simultaneous decrease of the electrical conductivity. The thermal conductivity was suppressed by the substitution of Fe for Mn. The maximum zT attained was 0.11 at 1150 K for the sample x = 0.05, which is about 20% higher than the x = 0 sample. Further study should be performed with finer Fe substituent tuning with $x < 0.1$ in order to optimize thermoelectric as well as mechanical properties of these compounds.
- For the first time, a high-temperature segmented thermoelectric based-oxide module comprising of *p*-legs segmentation of $Ti_{0.3}Zr_{0.35}Hf_{0.35}CoSb_{0.8}Sn_{0.2}$, and the misfit-layered cobaltite $Ca_3Co_4O_{9+\delta}$, and *n*-legs 2% Al-doped ZnO has been successfully fabricated and tested. Numerical modeling was used to optimize and design the TEG. The input for the model was the experimental data on the TE properties of the legs, as well as on electrical contact resistance. The enhancement of output power generation of the segmented TEG originated from the properties of the HH alloy in the low-to-mid temperature range, compared with those of the oxides. The high-performance of the segmented TEG also benefited from the reduction in the total internal resistance of the module due to

the low contact resistance between the HH alloy and the Ag electrodes. At a hot side temperature of 1173 K corresponding to a temperature gradient of about 700 K, the maximum power density of the module reached 0.65 W/cm^2, a value which is among the highest reported so far for oxide-based modules. Using 3D numerical modeling in combination with the experimental data, we found that the efficiency of the segmented TEG (1.16%) was significantly improved compared with the non-segmented TEG (0.37%). Initial long-term testing showed that a segmented oxide module is stable and exhibits a promising power generation e.g. from waste heat at high temperatures.

- High-temperature segmented *p*-type leg of the half-Heusler $Ti_{0.3}Zr_{0.35}Hf_{0.35}CoSb_{0.8}Sn_{0.2}$ (HH) and the doped misfit-layered cobaltite $Ca_{2.8}Lu_{0.15}Ag_{0.05}Co_4O_{9+\delta}$ was successfully fabricated. The resultant microstructure and the electrical contact resistance at the junction suggest that silver brazing is a suitable material for joining semi-metal and oxide material. The thermoelectric properties of single components and the segmented HH/$Ca_{2.8}Lu_{0.15}Ag_{0.05}Co_4O_{9+\delta}$ legs were characterized as a function of temperature. The results also indicated that the silver brazing at the interface preserved the intrinsic thermopower of the segments at small temperature difference. The output power generation characteristics of the segmented legs were measured in air under various temperature gradients. At ΔT of about 756 K, the maximum generated power density was attained with a value of 2.34 W/cm^2 corresponding to ~5% conversion efficiency, which is of date the highest value reported on oxide-based thermoelectrics. Long-term stability investigation in air suggests that this oxide-based segmented leg is very promising for generation of electricity from high-temperature waste heat.

Outlook of the future prospects

- Three-segment *p*-type BiTe/HH/$Ca_3Co_4O_9$ would be a good solution to improve the total conversion efficiency further.
- While the thermoelectric performance of *n*-type oxide materials is still much lower than the *p*-type counterparts, a uni-leg TEG which uses single segmented *p*-legs and metal connection may be considered a good solution.
- Doped $CaMnO_3$ oxide is a promising material, i.e. stable in air, and may be a good candidate for hot side material for a high-temperature segmentation if ZnO:Al will be replaced.

References

[1] Pollock DD. General Principles and Theoretical Considerations Phenomena 1995.

[2] Seebeck, T.J., Magnetische polarisation der metalle und erze durck temperatur- differenz, Abh. K. Akad. Wiss., 265 (1823). n.d.

[3] Snyder GJ, Toberer ES. Complex thermoelectric materials. Nat Mater 2008;7:105–14. doi:10.1038/nmat2090.

[4] Biswas K, He J, Blum ID, Wu C-I, Hogan TP, Seidman DN, et al. High-performance bulk thermoelectrics with all-scale hierarchical architectures. Nature 2012;489:414–8. doi:10.1038/nature11439.

[5] Zhao L-D, Lo S-H, Zhang Y, Sun H, Tan G, Uher C, et al. Ultralow thermal conductivity and high thermoelectric figure of merit in SnSe crystals. Nature 2014;508:373–7. doi:10.1038/nature13184.

[6] Heikes RR, Ure RW. Thermoelectricity: science and engineering. Interscience Publishers; 1961.

[7] M.H. Cobble. Calculation of generator performance. In D.M. Rowe, editor, CRC Handbook of Thermoelectrics, Chapter 39, pp. 489-501. CRC Press, Boca Raton, FL, 1995 n.d.

[8] Le Thanh Hung, Ngo Van Nong, Gerald Jeffrey Snyder, Benjamin Balke, Li Han, Rasmus Bjørk, Pham Hoang Ngan, Tim C. Holgate, Søren Linderoth and NP. Segmented thermoelectric oxide-based module. Energy 2014.

[9] Mele P, Kamei H, Yasumune H, Matsumoto K, Miyazaki K. Development of thermoelectric module based on dense Ca3Co4O9 and Zn0.98Al0.02O legs. Met Mater Int 2014;20:389–97. doi:10.1007/s12540-014-2024-7.

[10] Lim C-H, Choi S-M, Seo W-S, Park H-H. A Power-Generation Test for Oxide-Based Thermoelectric Modules Using p-Type Ca3Co4O9 and n-Type Ca0.9Nd0.1MnO3 Legs. J Electron Mater 2011;41:1247–55. doi:10.1007/s11664-011-1868-6.

[11] Fergus JW. Oxide materials for high temperature thermoelectric energy conversion. J Eur Ceram Soc 2012;32:525–40. doi:10.1016/j.jeurceramsoc.2011.10.007.

[12] Souma M. ; Shigeno, M. ; Ohba, Y. ; Nakamura, N. ; Shimozaki, T. T. O. Power generation characteristics of oxide thermoelectric modules incorporating nanostructured ZnO sintered materials. 2007 26th Int. Conf. Thermoelectr., IEEE; 2007, p. 38–41. doi:10.1109/ICT.2007.4569418.

[13] Matsubara I, Funahashi R, Takeuchi T, Sodeoka S, Shimizu T, Ueno K. Fabrication of an all-oxide thermoelectric power generator. Appl Phys Lett 2001;78:3627. doi:10.1063/1.1376155.

[14] Funahashi R, Mikami M, Mihara T, Urata S, Ando N. A portable thermoelectric-power-generating module composed of oxide devices. J Appl Phys 2006;99:66117. doi:10.1063/1.2180449.

[15] Souma T, Ohtaki M. ; Ohba, Y. ; Nakamura, N. ; Shimozaki, T. M; S. Fabrication and power generation characteristics of p-NaCo2O4 n-ZnO oxide thermoelectric modules 2006. doi:10.1109/ICT.2006.331386.

[16] Urata S, Funahashi R, Mihara T. Power generation of p-type Ca3Co4O9/n-type CaMnO3 module. 2006 25th Int. Conf. Thermoelectr., IEEE; 2006, p. 501–4. doi:10.1109/ICT.2006.331343.

[17] Funahashi R, Urata S. Fabrication and Application of an Oxide Thermoelectric System. Int J Appl Ceram Technol 2007;4:297–307. doi:DOI: 10.1111/j.1744-7402.2007.02144.x.

[18] Choi S-M, Lee K-H, Lim C-H, Seo W-S. Oxide-based thermoelectric power generation module using p-type Ca3Co4O9 and n-type (ZnO)7In2O3 legs. Energy Convers Manag 2011;52:335–9. doi:10.1016/j.enconman.2010.07.005.

[19] Ure RW, Heikes RR. Materials requirements for segmented thermoelectric materials. Adv Energy Convers 1962;2:177–81. doi:10.1016/0365-1789(62)90022-X.

[20] Vikhor LN, Anatychuk LI. Generator modules of segmented thermoelements. Energy Convers Manag 2009;50:2366–72. doi:10.1016/j.enconman.2009.05.020.

[21] Swanson BW, Somers E V., Heikes RR. Optimization of a Sandwiched Thermoelectric Device. J Heat Transfer 1961;83:77. doi:10.1115/1.3680473.

[22] Cohen RW, Abeles B. Efficiency Calculations of Thermoelectric Generators with Temperature Varying Parameters. J Appl Phys 1963;34:1687. doi:10.1063/1.1702659.

[23] Sherman B, Heikes RR, Ure RW. Calculation of Efficiency of Thermoelectric Devices. J Appl Phys 1960;31:1. doi:10.1063/1.1735380.

[24] G. J. Snyder, Thermoelectric Power Generation: Efficiency and Compatibility (CRC Press, Taylor & Francis Group, Boca Raton, FL, USA, 2006), Chap. 9, n.d.

[25] Snyder GJ. Application of the compatibility factor to the design of segmented and cascaded thermoelectric generators. Appl Phys Lett 2004;84:2436. doi:10.1063/1.1689396.

[26] Snyder G, Ursell T. Thermoelectric Efficiency and Compatibility. Phys Rev Lett 2003;91. doi:10.1103/PhysRevLett.91.148301.

[27] Fleurial J-P, Bux S, Caillat T. Engineering of Novel Thermoelectric Materials and Devices for Next Generation, Long Life, 20% Efficient Space Power Systems. 11th Int. Energy Convers. Eng. Conf., Reston, Virginia: American Institute of Aeronautics and Astronautics; 2013. doi:10.2514/6.2013-3927.

[28] D'Angelo J, Case ED, Matchanov N, Wu C-I, Hogan TP, Barnard J, et al. Electrical, Thermal, and Mechanical Characterization of Novel Segmented-Leg Thermoelectric Modules. J Electron Mater 2011;40:2051–62. doi:10.1007/s11664-011-1717-7.

[29] Crane DT, Kossakovski D, Bell LE. Modeling the Building Blocks of a 10% Efficient Segmented Thermoelectric Power Generator. J Electron Mater 2009;38:1382–6. doi:10.1007/s11664-009-0673-y.

[30] El-Genk MS, Saber HH. High efficiency segmented thermoelectric unicouple for operation between 973 and 300 K. Energy Convers Manag 2003;44:1069–88. doi:10.1016/S0196-8904(02)00109-7.

[31] Wojciechowski KT, Zybala R, Leszczynski J, Nieroda P, Schmidt M, Gajerski R, et al. Performance characterization of high-efficiency segmented Bi2Te3/CoSb3 unicouples for thermoelectric generators 2012:467–70. doi:10.1063/1.4731597.

[32] Anatychuk LI, Vikhor LN, Strutynska LT, Termena IS. Segmented Generator Modules Using Bi2Te3-Based Materials. J Electron Mater 2011;40:957–61. doi:10.1007/s11664-010-1468-x.

[33] El-Genk MS, Saber HH, Caillat T, Sakamoto J. Tests results and performance comparisons of coated and un-coated skutterudite based segmented unicouples. Energy Convers Manag 2006;47:174–200. doi:10.1016/j.enconman.2005.03.023.

[34] El-Genk MS, Saber HH. High efficiency segmented thermoelectric unicouple for operation between 973 and 300 K. Energy Convers Manag 2003;44:1069–88. doi:10.1016/S0196-8904(02)00109-7.

[35] Caillat T, Fleurial J-P, Snyder GJ, Borshchevsky A. Development of high efficiency segmented thermoelectric unicouples. Proc. ICT2001. 20 Int. Conf. Thermoelectr. (Cat. No.01TH8589), IEEE; n.d., p. 282–5. doi:10.1109/ICT.2001.979888.

[36] Yatir Sadia, Ohad Ben-Yehuda YG. Highly Efficient Segmented p-type Thermoelectric Leg. Dordrecht: Springer Netherlands; 2013. doi:10.1007/978-94-007-4984-9_5.

[37] El-Genk MS, Saber HH, Caillat T. Efficient segmented thermoelectric unicouples for space power applications. Energy Convers Manag 2003;44:1755–72. doi:10.1016/S0196-8904(02)00217-0.

[38] Sadia Y, Gelbstein Y. Silicon-Rich Higher Manganese Silicides for Thermoelectric Applications. J Electron Mater 2012;41:1504–8. doi:10.1007/s11664-012-1936-6.

[39] El-Genk MS. Performance Tests of Skutterudites and Segmented Thermoelectric Converters. AIP Conf. Proc., vol. 699, AIP; 2004, p. 541–52. doi:10.1063/1.1649615.

[40] Ben-Yehuda O, Gelbstein Y, Dashevsky Z, George Y, Dariel MP. Functionally Graded Bi_2Te_3 based material for above ambient temperature application. 2007 26th Int. Conf. Thermoelectr., IEEE; 2007, p. 82–5. doi:10.1109/ICT.2007.4569429.

[41] Orrù R, Licheri R, Locci AM, Cincotti A, Cao G. Consolidation/synthesis of materials by electric current activated/assisted sintering. Mater Sci Eng R Reports 2009;63:127–287. doi:10.1016/j.mser.2008.09.003.

[42] Matsugi K, Wang Y, Hatayama T, Yanagisawa O, Syakagohri K. Application of electric discharge process in joining aluminum and stainless steel sheets. J Mater Process Technol 2003;135:75–82. doi:10.1016/S0924-0136(02)01040-3.

[43] Matsugi K, Konishi M, Yanagisawa O, Komatsu M. Design and manufacture of an impact–electric current discharge joining machine. Mater Sci Eng A 2003;350:195–201. doi:10.1016/S0921-5093(02)00727-X.

[44] Van Nong N, Pryds N, Linderoth S, Ohtaki M. Enhancement of the thermoelectric performance of p-type layered oxide $Ca_3Co_4O(_9+\delta)$ through heavy doping and metallic nanoinclusions. Adv Mater 2011;23:2484–90. doi:10.1002/adma.201004782.

[45] Hung LT, Nong N Van, Han L, Minh D Le, Borup KA, Iversen BB, et al. High-temperature thermoelectric properties of Ca0.9Y0.1Mn1−x Fe x O3 ($0 \leq x \leq 0.25$). J Mater Sci 2012;48:2817–22. doi:10.1007/s10853-012-6834-z.

[46] Han L, Hung LT, Nong N, Pryds N, Linderoth S. The Influence of Spark Plasma Sintering Temperature on the Microstructure and Thermoelectric Properties of Al,Ga Dual-Doped ZnO. J Electron Mater 2012;42:1573–81. doi:10.1007/s11664-012-2325-x.

[47] Grange P, Delmon B, editors. Interfaces in New Materials. Dordrecht: Springer Netherlands; 1991. doi:10.1007/978-94-011-3680-8.

[48] Singh M, Ohji T, Asthana R, Mathur S, editors. Ceramic Integration and Joining Technologies. Hoboken, NJ, USA: John Wiley & Sons, Inc.; 2011. doi:10.1002/9781118056776.

[49] http://tellurex.com/shop-products/#TPG n.d.

[50] Rowe DM. CRC Handbook of Thermoelectrics. Boca Raton, FL: CRC Press; 1995.

[51] Vining CB. An inconvenient truth about thermoelectrics. Nat Mater 2009;8:83–5. doi:10.1038/nmat2361.

[52] Kristiansen NR, Snyder GJ, Nielsen HK, Rosendahl L. Waste Heat Recovery from a Marine Waste Incinerator Using a Thermoelectric Generator. J Electron Mater 2012;41:1024–9. doi:10.1007/s11664-012-2009-6.

[53] Koumoto K, Wang Y, Zhang R, Kosuga A, Funahashi R. Oxide Thermoelectric Materials: A Nanostructuring Approach. Annu Rev Mater Res 2010;40:363–94. doi:10.1146/annurev-matsci-070909-104521.

[54] Walia S, Balendhran S, Nili H, Zhuiykov S, Rosengarten G, Wang QH, et al. Transition metal oxides – Thermoelectric properties. Prog Mater Sci 2013;58:1443–89. doi:10.1016/j.pmatsci.2013.06.003.

[55] He J, Liu Y, Funahashi R. Oxide thermoelectrics: The challenges, progress, and outlook. J Mater Res 2011;26:1762–72. doi:10.1557/jmr.2011.108.

[56] Yadav GG, Susoreny J a, Zhang G, Yang H, Wu Y. Nanostructure-based thermoelectric conversion: an insight into the feasibility and sustainability for large-scale deployment. Nanoscale 2011;3:3555–62. doi:10.1039/c1nr10555h.

[57] Koumoto K, Funahashi R, Guilmeau E, Miyazaki Y, Weidenkaff A, Wang Y, et al. Thermoelectric Ceramics for Energy Harvesting. J Am Ceram Soc 2013;96:1–23. doi:10.1111/jace.12076.

[58] Jood P, Mehta RJ, Zhang Y, Borca-Tasciuc T, Dou SX, Singh DJ, et al. Heavy element doping for enhancing thermoelectric properties of nanostructured zinc oxide. RSC Adv 2014;4:6363. doi:10.1039/c3ra46813e.

[59] Guilmeau E, Maignan A, Martin C. Thermoelectric Oxides: Effect of Doping in Delafossites and Zinc Oxide. J Electron Mater 2009;38:1104–8. doi:10.1007/s11664-009-0815-2.

[60] Van NN, Pryds N. Nanostructured oxide materials and modules for high-temperature power generation from waste heat. Adv Nat Sci Nanosci Nanotechnol 2013;4:023002. doi:10.1088/2043-6262/4/2/023002.

[61] Han L, Van Nong N, Zhang W, Hung LT, Holgate T, Tashiro K, et al. Effects of morphology on the thermoelectric properties of Al-doped ZnO. RSC Adv 2014;4:12353. doi:10.1039/c3ra47617k.

[62] Brockway L, Vasiraju VRK, Sunkara MK, Vaddiraju S. Engineering Efficient Thermoelectrics from Large-scale Assemblies of doped ZnO Nanowires: Nanoscale Effects and Resonant-Level Scattering. ACS Appl Mater Interfaces 2014:140811154730003. doi:10.1021/am5023489.

[63] Mikami M, Guilmeau E, Funahashi R. Enhancement of electrical properties of the thermoelectric compound Ca 3 Co 4 O 9 through use of large-grained powder 2005:2491–7.

[64] Pichanusakorn P, Bandaru P. Nanostructured thermoelectrics. Mater Sci Eng R Reports 2010;67:19–63. doi:10.1016/j.mser.2009.10.001.

[65] Ohtaki M, Araki K, Yamamoto K. High Thermoelectric Performance of Dually Doped ZnO Ceramics. J Electron Mater 2009;38:1234–8. doi:10.1007/s11664-009-0816-1.

[66] Bérardan D, Byl C, Dragoe N. Influence of the Preparation Conditions on the Thermoelectric Properties of Al-Doped ZnO. J Am Ceram Soc 2010;93:2352–8. doi:10.1111/j.1551-2916.2010.03751.x.

[67] Nong NV, Liu C-J, Ohtaki M. Improvement on the high temperature thermoelectric performance of Ga-doped misfit-layered Ca3Co4−xGaxO9+δ (x=0, 0.05, 0.1, and 0.2). J Alloys Compd 2010;491:53–6. doi:10.1016/j.jallcom.2009.11.009.

[68] Xia C, Sugiyama J, Itahara H, Tani T. Platelet crystals of thermoelectric layered cobaltites; pure and Sr-doped. J Cryst Growth 2005;276:519–24. doi:10.1016/j.jcrysgro.2004.11.415.

[69] Funahashi R. Waste Heat Recovery Using Thermoelectric Oxide Materials. Sci Adv Mater 2011;3:682–6. doi:10.1166/sam.2011.1200.

[70] Ngan PH, Christensen DV, Snyder GJ, Hung LT, Linderoth S, Nong N Van, et al. Towards high efficiency segmented thermoelectric unicouples. Phys Status Solidi 2014;211:9–17. doi:10.1002/pssa.201330155.

[71] Ma Y, Hao Q, Poudel B, Lan Y, Yu B, Wang D, et al. Enhanced thermoelectric figure-of-merit in p-type nanostructured bismuth antimony tellurium alloys made from elemental chunks. Nano Lett 2008;8:2580–4. doi:10.1021/nl8009928.

[72] Chan TE, Venkatasubramanian R, LeBeau JM, Thomas P, Stuart J, Koch CC. Enhanced Thermoelectric Figure-of-merit at Room Temperature in Bulk Bi(Sb)Te(Se) With Grain Size of ∼100nm. MRS Proc 2013;1543:93–8. doi:10.1557/opl.2013.948.

[73] Li D, Li R, Qin X-Y, Song C-J, Xin H-X, Wang L, et al. Co-precipitation synthesis of nanostructured Cu3SbSe4 and its Sn-doped sample with high thermoelectric performance. Dalton Trans 2014;43:1888–96. doi:10.1039/c3dt52447g.

[74] Wang S, Tan X, Tan G, She X, Liu W, Li H, et al. The realization of a high thermoelectric figure of merit in Ge-substituted β-Zn4Sb3 through band structure modification. J Mater Chem 2012;22:13977. doi:10.1039/c2jm30906h.

[75] Yan X, Liu W, Wang H, Chen S, Shiomi J, Esfarjani K, et al. Stronger phonon scattering by larger differences in atomic mass and size in p-type half-Heuslers Hf1−xTixCoSb0.8Sn0.2. Energy Environ Sci 2012;5:7543. doi:10.1039/c2ee21554c.

[76] Sui J, Li J, He J, Pei Y-L, Berardan D, Wu H, et al. Texturation boosts the thermoelectric performance of BiCuSeO oxyselenides. Energy Environ Sci 2013;6:2916. doi:10.1039/c3ee41859f.

[77] Shi X, Yang J, Salvador JR, Chi M, Cho JY, Wang H, et al. Multiple-filled skutterudites: high thermoelectric figure of merit through separately optimizing electrical and thermal transports. J Am Chem Soc 2011;133:7837–46. doi:10.1021/ja111199y.

[78] Liu W, Tang X, Sharp J. Low-temperature solid state reaction synthesis and thermoelectric properties of high-performance and low-cost Sb-doped Mg 2 Si 0.6 Sn 0.4. J Phys D Appl Phys 2010;43:085406. doi:10.1088/0022-3727/43/8/085406.

[79] Joshi G, Lee H, Lan Y, Wang X, Zhu G, Wang D, et al. Enhanced thermoelectric figure-of-merit in nanostructured p-type silicon germanium bulk alloys. Nano Lett 2008;8:4670–4. doi:10.1021/nl8026795.

[80] Wang XW, Lee H, Lan YC, Zhu GH, Joshi G, Wang DZ, et al. Enhanced thermoelectric figure of merit in nanostructured n-type silicon germanium bulk alloy. Appl Phys Lett 2008;93:193121. doi:10.1063/1.3027060.

[81] Brown SR, Kauzlarich SM, Gascoin F, Snyder GJ. Yb 14 MnSb 11 : New High Efficiency Thermoelectric Material for Power Generation. Chem Mater 2006;18:1873–7. doi:10.1021/cm060261t.

[82] May AF, Flage-Larsen E, Snyder GJ. Electron and phonon scattering in the high-temperature thermoelectric La_{3}Te_{4−z}M_{z} (M=Sb,Bi). Phys Rev B 2010;81:125205. doi:10.1103/PhysRevB.81.125205.

[83] J. Yang, T. Caillat, MRS Bull. 2006, 31 224–229. Thermoelectric Materials for Space and Automotive Power Generation n.d.

[84] Kambe M, Jinushi T, Ishijima Z. Encapsulated Thermoelectric Modules and Compliant Pads for Advanced Thermoelectric Systems. J Electron Mater 2010;39:1418–21. doi:10.1007/s11664-010-1315-0.

[85] Nong N V., Ohtaki M. Thermoelectric properties and local electronic structure of rare earth-doped Ca3Co2O6. 2006 25th Int. Conf. Thermoelectr., IEEE; 2006, p. 62–5. doi:10.1109/ICT.2006.331270.

[86] Ito M, Furumoto D. Microstructure and thermoelectric properties of NaxCo2O4/Ag composite synthesized by the polymerized complex method. J Alloys Compd 2008;450:517–20. doi:10.1016/j.jallcom.2006.12.081.

[87] Kikuchi a., Okinaka N, Akiyama T. A large thermoelectric figure of merit of La-doped SrTiO3 prepared by combustion synthesis with post-spark plasma sintering. Scr Mater 2010;63:407–10. doi:10.1016/j.scriptamat.2010.04.041.

[88] Bocher L, Aguirre MH, Logvinovich D, Shkabko A, Robert R, Trottmann M, et al. CaMn(1-x)Nb(x)O3 (x < or = 0.08) perovskite-type phases as promising new high-temperature n-type thermoelectric materials. Inorg Chem 2008;47:8077–85. doi:10.1021/ic800463s.

[89] http://www.alfa.com. Accessed 24 Novemb 2014 n.d.

[90] LeBlanc S, Yee SK, Scullin ML, Dames C, Goodson KE. Material and manufacturing cost considerations for thermoelectrics. Renew Sustain Energy Rev 2014;32:313–27. doi:10.1016/j.rser.2013.12.030.

[91] Snyder GJ. Thermoelectrics And Its Energy Harvesting: Materials, Preparation, And Characterization In Thermoelectrics 2012.

[92] Seifert W, Pluschke V, Goupil C, Zabrocki K, Müller E, Snyder GJ. Maximum performance in self-compatible thermoelectric elements. J Mater Res 2011;26:1933–9. doi:10.1557/jmr.2011.139.

[93] Muto A, Yang J, Poudel B, Ren Z, Chen G. Skutterudite Unicouple Characterization for Energy Harvesting Applications. Adv Energy Mater 2013;3:245–51. doi:10.1002/aenm.201200503.

[94] García-Cañadas J, Min G. Preparation and characterisation of contacts for high temperature thermoelectric modules 2012:454–7. doi:10.1063/1.4731594.

[95] Wojciechowski KT, Zybala R, Mania R. High temperature CoSb3–Cu junctions. Microelectron Reliab 2011;51:1198–202. doi:10.1016/j.microrel.2011.03.033.

[96] Le Thanh Hung, Ngo Van Nong, G. Jeffrey Snyder, Li Han, Eugen Stamate, Man Hoang Viet, Benjamin Balke, Søren Linderoth and NP. High Performance p-type Segmentation of Oxide and Half-Heusler Alloy. Energy Convers Manag n.d.

[97] Yee SK, LeBlanc S, Goodson KE, Dames C. $ per W metrics for thermoelectric power generation: beyond ZT. Energy Environ Sci 2013;6:2561. doi:10.1039/c3ee41504j.

[98] Han L, Nong N Van, Hung LT, Holgate T, Pryds N, Ohtaki M, et al. The influence of α- and γ-Al2O3 phases on the thermoelectric properties of Al-doped ZnO. J Alloys Compd 2013;555:291–6. doi:10.1016/j.jallcom.2012.12.091.

[99] Rowe DM. Thermoelectrics Handbook: Macro to Nano. CRC Press, 6000 Broken Sound Parkway NW, Suite 300, Boca Raton, FL, 33487, 912 pages, Taylor and Francis Group.; 2006.

[100] Kosuga A, Urata S, Kurosaki K, Yamanaka S, Funahashi R. Mechanical Properties of Ca 0.9 Yb 0.1 MnO 3 /Ag Composites for n-Type Legs of Thermoelectric Oxide Devices. Jpn J Appl Phys 2008;47:6399–403. doi:10.1143/JJAP.47.6399.

[101] Wang Y, Sui Y, Fan H, Wang X, Su Y, Su W, et al. High Temperature Thermoelectric Response of Electron-Doped CaMnO 3. Chem Mater 2009;21:4653–60. doi:10.1021/cm901766y.

[102] Flahaut D, Mihara T, Funahashi R, Nabeshima N, Lee K, Ohta H, et al. Thermoelectrical properties of A-site substituted Ca[sub 1−x]Re[sub x]MnO[sub 3] system. J Appl Phys 2006;100:084911. doi:10.1063/1.2362922.

[103] Wang Y, Sui Y, Su W. High temperature thermoelectric characteristics of Ca[sub 0.9]R[sub 0.1]MnO[sub 3] (R=La,Pr,[ellipsis (horizontal)],Yb). J Appl Phys 2008;104:093703. doi:10.1063/1.3003065.

[104] Bocher L, Aguirre MH, Robert R, Logvinovich D, Bakardjieva S, Hejtmanek J, et al. High-temperature stability, structure and thermoelectric properties of CaMn1-xNbxO3CaMn1-xNbxO3 phases. Acta Mater 2009;57:5667–80. doi:10.1016/j.actamat.2009.07.062.

[105] Kosuga A, Isse Y, Wang Y, Koumoto K, Funahashi R. High-temperature thermoelectric properties of Ca[sub 0.9−x]Sr[sub x]Yb[sub 0.1]MnO[sub 3−δ] (0≤x≤0.2). J Appl Phys 2009;105:093717. doi:10.1063/1.3125450.

[106] Thuy NT, Minh DL, Nong NV, Bahl CRH and Pryds N 7-9, November, Ho Chi Minh city, Vietnam (2011). No Title. Proc Press Solid State Phys Mater Sci Symp (in Press n.d.

[107] Wang HC, Wang CL, Su W Bin, Liu J, Sun Y, Peng H, et al. Doping Effect of La and Dy on the Thermoelectric Properties of SrTiO3. J Am Ceram Soc 2011;94:838–42. doi:10.1111/j.1551-2916.2010.04185.x.

[108] Poeppelmeier KR, Leonowicz ME, Scanlon JC, Longo JM, Yelon WB. Structure determination of CaMnO3 and CaMnO2.5 by X-ray and neutron methods. J Solid State Chem 1982;45:71–9. doi:10.1016/0022-4596(82)90292-4.

[109] Kostogloudis G. Electronic conductivity in the Pr1âˆ’xSrxCo1âˆ’yMnyO3âˆ’Î´ system. Solid State Ionics 1999;118:241–9. doi:10.1016/S0167-2738(98)00193-3.

[110] Shannon RD. Revised effective ionic radii and systematic studies of interatomic distances in halides and chalcogenides. Acta Crystallogr Sect A 1976;32:751–67. doi:10.1107/S0567739476001551.

[111] Karim D, Aldred A. Localized level hopping transport in La(Sr)CrO_{3}. Phys Rev B 1979;20:2255–63. doi:10.1103/PhysRevB.20.2255.

[112] Vecherskii SI, Konopel MA, Esina NO, Batalov NN. (0 < x ≤ 0 . 15) Mixtures 2002;38:1270–6.

[113] G. H. Jonker, Philips Res. Rep., 1968, 23 131–138. No Title n.d.

[114] Ohtaki M, Tsubota T, Eguchi K, Arai H. High-temperature thermoelectric properties of (Zn1−xAlx)O. J Appl Phys 1996;79:1816. doi:10.1063/1.360976.

[115] Wu N, Holgate TC, Nong N, Pryds N, Linderoth S. Effects of Synthesis and Spark Plasma Sintering Conditions on the Thermoelectric Properties of Ca3Co4O9+δ. J Electron Mater 2013;42:2134–42. doi:10.1007/s11664-013-2546-7.

[116] Poon SJ, Wu D, Zhu S, Xie W, Tritt TM, Thomas P, et al. Half-Heusler phases and nanocomposites as emerging high-ZT thermoelectric materials. J Mater Res 2011;26:2795–802. doi:10.1557/jmr.2011.329.

[117] Snyder, G. J. “Thermoelectric Power Generation: Efficiency and Compatibility” Chapter 9, in Thermoelectrics Handbook: Macro to Nano edited by D. M. Rowe, CRC Press (2006) n.d.

[118] Bjørk R, Christensen DV, Eriksen D, Pryds N. Analysis of the internal heat losses in a thermoelectric generator. Int J Therm Sci 2014;85:12–20. doi:10.1016/j.ijthermalsci.2014.06.003.

[119] Jeffrey Snyder G, Caillat T. Using the Compatibility Factor to Design High Efficiency Segmented Thermoelectric Generators. MRS Proc 2003;793:S2.1. doi:10.1557/PROC-793-S2.1.

[120] Baranowski LL, Jeffrey Snyder G, Toberer ES. Effective thermal conductivity in thermoelectric materials. J Appl Phys 2013;113:204904. doi:10.1063/1.4807314.

[121] Chen W-H, Liao C-Y, Hung C-I, Huang W-L. Experimental study on thermoelectric modules for power generation at various operating conditions. Energy 2012;45:874–81. doi:10.1016/j.energy.2012.06.076.

[122] Casper F, Graf T, Chadov S, Balke B, Felser C. Half-Heusler compounds: novel materials for energy and spintronic applications. Semicond Sci Technol 2012;27:63001. doi:10.1088/0268-1242/27/6/063001.

[123] Liang G, Zhou J, Huang X. Analytical model of parallel thermoelectric generator. Appl Energy 2011;88:5193–9. doi:10.1016/j.apenergy.2011.07.041.

[124] Goldsmid HJ. Introduction to Thermoelectricity. vol. 121. Berlin, Heidelberg: Springer Berlin Heidelberg; 2010. doi:10.1007/978-3-642-00716-3.

[125] Holgate TC, Han L, Wu N, Bøjesen ED, Christensen M, Iversen BB, et al. Characterization of the interface between an Fe–Cr alloy and the p-type thermoelectric oxide Ca3Co4O9. J Alloys Compd 2014;582:827–33. doi:10.1016/j.jallcom.2013.08.096.

[126] Apertet Y, Ouerdane H, Goupil C, Lecoeur P. Series thermoelectrics. Eprint arXiv:12065649 2012:7.

[127] Park K, Lee GW. Fabrication and thermoelectric power of π-shaped Ca3Co4O9/CaMnO3 modules for renewable energy conversion. Energy 2013;60:87–93. doi:10.1016/j.energy.2013.07.025.

[128] Salvador JR, Cho JY, Ye Z, Moczygemba JE, Thompson AJ, Sharp JW, et al. Thermal to Electrical Energy Conversion of Skutterudite-Based Thermoelectric Modules. J Electron Mater 2012;42:1389–99. doi:10.1007/s11664-012-2261-9.

[129] Muto A, Kraemer D, Hao Q, Ren ZF, Chen G. Thermoelectric properties and efficiency measurements under large temperature differences. Rev Sci Instrum 2009;80:93901. doi:10.1063/1.3212668.

[130] Kim S. Analysis and modeling of effective temperature differences and electrical parameters of thermoelectric generators. Appl Energy 2013;102:1458–63. doi:10.1016/j.apenergy.2012.09.006.

[131] Ohta M, Biswas K, Lo S-H, He J, Chung DY, Dravid VP, et al. Enhancement of Thermoelectric Figure of Merit by the Insertion of MgTe Nanostructures in p-type PbTe Doped with Na2Te. Adv Energy Mater 2012;2:1117–23. doi:10.1002/aenm.201100756.

[132] Brown SR, Kauzlarich SM, Gascoin F, Snyder GJ. Yb14MnSb11: New High Efficiency Thermoelectric Material for Power Generation. ChemInform 2006;37. doi:10.1002/chin.200625011.

[133] Date A, Date A, Dixon C, Akbarzadeh A. Progress of thermoelectric power generation systems: Prospect for small to medium scale power generation. Renew Sustain Energy Rev 2014;33:371–81. doi:10.1016/j.rser.2014.01.081.

[134] Le TH, Ngo VN, Pryds N. Physica Status Solidi A : Applications and Materials Science Segmentation of low-cost , high efficiency oxide-based thermoelectric materials n.d. doi:10.1002/pssa.201431626.

[135] http://sps.fdc.co.jp/whats/whats4.html n.d.